THE RESISTIVE ALFVEN SPECTRUM OF TOKAMAK-LIKE CONFIGURATIONS

W. KERNER, K. LERBINGER, K. RIEDEL*

IPP 6/250 August 1985

MAX-PLANCK-INSTITUT FÜR PLASMAPHYSIK

8046 GARCHING BEI MÜNCHEN

MAX-PLANCK-INSTITUT FÜR PLASMAPHYSIK

GARCHING BEI MÜNCHEN

THE RESISTIVE ALFVEN SPECTRUM OF TOKAMAK-LIKE CONFIGURATIONS

W. KERNER, K. LERBINGER, K. RIEDEL*

IPP 6/250 August 1985

*Courant Institute of Mathematical Sciences

New York University

New York, N.Y. 10012

Die nachstehende Arbeit wurde im Rahmen des Vertrages zwischen dem Max-Planck-Institut für Plasmaphysik und der Europäischen Atomgemeinschaft über die Zusammenarbeit auf dem Gebiete der Plasmaphysik durchgeführt.

Abstract

The resistive Alfven spectrum for tokamak-like configurations with one or two singular surfaces is analyzed by combined WKBJ treatment and numerical solution using a spectral code. It is found that the ideal continua disappear; these are approximated only at the end points, at the singular surfaces and at selected interior points (given by extrema of $\omega_A(r) = |\vec{k} \cdot \vec{B}_0|/\sqrt{\rho_0}$). The normal modes are damped and the eigenvalues lie on specific curves which become independent of resistivity for small η .

1. Introduction

The study of linearized motion has significantly contributed to the understanding of ideal and resistive MHD plasma phenomena such as stability, wave propagation and heating. The most complete picture is obtained by means of a normal-mode analysis. Since this analysis is quite difficult both analytically and numerically, simpler methods have been developed. The classical boundary layer approach /1/, i.e. the Δ' concept, is suitable for treating current and pressure-driven instabilites but is not applicable for wave propagation. An energy principle in the fashion of the ideal MHD δW formalism has been derived to analyze the stability with respect to resistive perturbations /2-6/. Since the resistive time scale is of the order of milliseconds and hence significantly larger than the ideal time scale, detailed knowledge about the perturbations is as important as the determintion of stability in discussing their influence on the long-time plasma evolution.

The numerical solution for the full spectrum of eigenfrequencies and the corresponding normal modes is a complicated task, even in ideal MHD. With dissipation, complex frequencies evolve which are expressed by complex eigenvalues. The successful discretization of the ideal MHD operator by means of a Hermitian eigenvalue problem and its numerous interesting results suggest that dissipative MHD be tackled in the same fashion. Knowledge of the ideal problem was used to develop a spectral code of solving for the entire spectrum of compressible, resistive MHD /7/. Combining the Galerkin method with a finite-element discretization yields the general complex eigenvalue problem $\mathcal{A}\mathbf{x} = \lambda\mathcal{B}\mathbf{x}$. Inverse vector iteration, which preserves the band structure of the matrices, finds selected eigenvalues and allows entire parts of the complex spectrum to be successively mapped out even in cases of large matrix dimension /8/. This scheme is therefore suited to analyzing the complexe resistive spectrum with great accuracy.

The influence of resistivity on the spectrum is twofold. Point eigenvalues of the

ideal system are distorted linearly with η, e.g. the fast magnetoacoustic waves experience a small damping superimposed on a large oscillation frequency. The larger this frequency is, i.e. the more radial nodes there are, the larger is the damping. Consequently, these eigenvalues lie on rays only a small angle off the imaginary axis. Both the shear-Alfven and sound modes, on the other hand, show completely different behaviour. If resistivity is added, the logarithmic singularity in the eigenfunctions is no longer present and, hence, the ideal continua disappear. The influence of resistivity on these branches is therefore drastic as shown by Boris /9/ and recently rediscussed by several authors /10-15/. Stimulated by the pioneering numerical analysis of Ryu and Grimm /10/, we investigate the resistive Alfven modes in detail for experimentally relevant configurations. Our numerical scheme affords an accuracy resulting in much finer details of the spectrum. Complete results can thus be given. It is found that the ideal continua disappear and are approximated only at the end points and at a few selected interior points. These interior points are given in terms of the ideal Alfven dispersion relation $\omega_A = |\vec{k} \cdot \vec{B}_0|/\sqrt{\rho_0}$, where $\vec{k}$ is the wave vector of the perturbation and $\vec{B}_0$ the equilibrium magnetic field; ρ_0 is the density. Configurations with magnetic shear and with one or two resonant surfaces in the plasma are treated. The eigenvalues lie on well-defined curves in the complex plane which become independent of η in the limit $\eta \to 0$. The scaling of the damping with η is displayed for different profiles. The logarithmic singularity in the radial velocity component is altered into an oscillatory behaviour. Eikonal functions form the solutions of the resistive system.

The behaviour of the resistive Alfven modes for vanishing η can be analyzed analytically by phase-integral or WKBJ methods. So far only simple configurations without magnetic shear in slab geometry /11,12/ and cylindrical geometry /13/ have been solved completely. The most complete WKBJ treatment which takes the ideal solutions into account has been given by Pao and Kerner /14/; the spectrum is shown to be determined by the geometry of the anti-Stokes lines. A brief discussion for the case where $\vec{k} \cdot \vec{B}_0$

vanishes is also given there. A generalization to cases with singular surfaces together with the discussion of two turning points was given by K. Riedel /15/; in this paper viscosity is included. Such an analytical approach suited to the asymptotic limit of vanishing resistivity complements the numerical method valid for large, medium and small resistivity, but not for asymptotically small η. The numerical approach in particular allows examination of complicated realistic equilibria which are too complex for complete mathematical treatment. This calls for numerical solution which is rather involved /16/. By combining the accurate normal-mode code with the sophisticated phase-integral method we are able to discuss a tokamak-like equilibrium thoroughly. In this configuration a large longitudinal current is present which leads to finite magnetic shear, and one, or two resonant surfaces lie in the plasma. It is emphasized that the numerical scheme in conjunction with careful convergence studies using an increasingly finer mesh affords accurate results for sufficiently small η. The asymptotic behaviour is therefore mapped out numerically. Then the eikonal ansatz is introduced and the formal asymptotic solutions are constructed. In the limit of small β the slow-wave solutions do not couple to the Alfven wave solutions. The geometry of the anti-Stokes lines involving one and two turning points then determines the resistive Alfven spectrum, which lies on specific, quite complicated curves in the complex eigenvalue plane. Furthermore, these curves are asymptotically independent of η. The structure of the eigenfunctions is derived from this phase-integral analysis. In this fashion the spectrum is mapped out thoroughly for configurations where three or four branch points are involved in the eigenvalue curves. Details of the solutions for the eigenvalues as well as for the eigenfunctions are displayed.

The paper is organized as follows: The physical model which is the common compressible resistive MHD model is presented in Sec. 2. We also discuss the numerical scheme and show how it reduces the computation to a complex eigenvalue problem. Results for the resistive Alfven branch for tokamak-like equilibria with singular surface $\vec{k}\cdot\vec{B}_0 = 0$ are

presented in Sec. 3. These configurations have longitudinal current and finite magnetic shear and represent a tokamak with large aspect ratio in cylindrical geometry. Then the case with two resonant surfaces in the plasma is discussed. Since the Alfven branch considered here is characterized by incompressibility like the tearing mode, a short side step is taken to discuss with a force-free equilibrium the transition of this unstable mode into the stable domain. The connection between this stable tearing mode and the Alfven modes is discussed. Section 4 presents the phase-integral method and the corresponding results, including the discussion of the anti-Stokes line pattern. Finally, Section 5 contains the discussion and the conclusions.

2. Model

2.1 Physical model

The plasma is described in terms of single-fluid theory. The resistive MHD equations read in normalized, dimensionless form

equation of motion

$$\rho(\frac{\partial \vec{v}}{\partial t} + \vec{v} \cdot \nabla \vec{v}) = -\nabla P + (\nabla \times \vec{B}) \times \vec{B}, \tag{1}$$

Maxwell - Ohm

$$\frac{\partial \vec{B}}{\partial t} = \nabla \times (\vec{v} \times \vec{B}) - \nabla \times (\eta \nabla \times \vec{B}), \tag{2}$$

adiabatic law

$$\frac{\partial P}{\partial t} = -\gamma P \nabla \cdot \vec{v} - \vec{v} \cdot \nabla P, \tag{3}$$

Maxwell

$$\nabla \cdot \vec{B} = 0. \tag{4}$$

Here ρ denotes the density, $\vec{v}$ the velocity, $\vec{B}$ the magnetic field, P the pressure and η

the resistivity; γ is the ratio of the specific heats. Note that the assumption of incompressibility, $\nabla \cdot \vec{v} = 0$, is not made. The adiabatic law is adopted for the equation of state since the dissipation proportional to η is considered to be small. The incompressible equations of motion accurately describes the plasma behaviour if the pressure variations are small compared with the mean thermodynamic pressure. Since the resistive modes rapidly oscillate, the compressible set of equations is appropriate. Then the fast and slow magnetoacoustic waves are retained. These equations are now linearized around a static equilibrium characterized by $\frac{\partial}{\partial t} = 0$ and $\vec{v}_0 = 0$. The equilibrium is then determined by the equation

$$\nabla P_0 = (\nabla \times \vec{B}_0) \times \vec{B}_0. \tag{5}$$

In straight geometry static, ideal equilibria can be interpreted as resistive equilibria if $\nabla \times \eta(\nabla \times \vec{B}_0) = 0$, with the consequence that $\eta_0 j_0 = E_z = const.$ In toroidal geometry a resistive equilibrium is only possible with flow, i.e. $\vec{v}_0 \neq 0$. This flow, however, is proportional to η and hence very small. Here we take the simplest approach of a constant resistivity η_0 instead of a constant E_z; this still gives the basic features of resistive modes, since we are interested in phenomena which scale as $\eta^{\frac{1}{2}}$ or $\eta^{\frac{1}{3}}$. For a circular cylinder the equilibrium quantities only have an r-dependence. With the usual cylindrical coordinates r, θ, z the equilibrium is determined by the equation

$$\frac{\partial P_0}{\partial r} = -\frac{1}{r} B_\theta \frac{\partial}{\partial r}(r B_\theta) - B_z \frac{\partial}{\partial r} B_z. \tag{6}$$

With two profiles given, eq. (6) can be solved to give the remaining one.

The following separation ansatz is suitable for the perturbed quantities :

$$f(r, \theta, z; t) = f(r)\ exp(im\theta + inkz + \lambda t), \tag{7}$$

where λ is the eigenvalue. The growth rate λ_R is then defined as the real part of λ, i.e. $\lambda_R = Re(\lambda)$. With $k = \frac{2\pi}{L}$ defining a periodicity length, a tokamak with large aspect

ratio is simulated, n corresponding to the toroidal mode number; m is the poloidal mode number. In ideal MHD λ is either real or purely imaginary, which leads to unstable or purely oscillating waves. With resistivity included, the frequency can become complex. The equations for the perturbed quantities $\vec{v}, p$ and $\vec{b}$ read

$$\lambda \rho_0 \vec{v} = -\nabla p + (\nabla \times \vec{B}_0) \times \vec{b} + (\nabla \times \vec{b}) \times \vec{B}_0, \tag{8}$$

$$\lambda p = -\gamma P_0 \nabla \cdot \vec{v} - \vec{v} \cdot \nabla P_0, \tag{9}$$

$$\lambda \vec{b} = \nabla \times (\vec{v} \times \vec{B}_0) - \nabla \times (\eta \nabla \times \vec{b}). \tag{10}$$

The divergence condition, eq.(4), for the perturbed field, $\nabla \cdot \vec{b} = 0$, is used to eliminate b_θ provided m $\neq 0$. The perturbed resistivity is set to zero, thus eliminating the rippling mode.

Finally, we discuss the boundary conditions. It is assumed that the plasma is surrounded by a perfectly conducting wall, which implies the following conditions at the wall :

$$v_r(a) = 0, \tag{11a}$$

$$b_r(a) = 0. \tag{11b}$$

For finite resistivity in the plasma the Maxwell equations require that the tangential component of the electric field vanish at the wall. This implies

$$(b_z)'_{r=a} = 0. \tag{11c}$$

On the axis $r = 0$ all the quantities are regular.

2.2 Numerical method

The set of resistive MHD equations is solved in its weak form. By introducing a state vector $\vec{u}$ which contains the perturbed velocity, pressure and magnetic field,

$$\vec{u}^T = (v_r, v_\theta, v_z, p, b_r, b_z), \tag{12}$$

the differential equations (8 - 10) can be written in the form $\mathcal{L}\vec{u} = 0$, where $\mathcal{L}$ denotes the linear matrix operator. The components of $\vec{u}(r)$ are approximated by a finite linear combination of local expansion functions, namely cubic Hermite elements for v_r and b_r and quadratic ones for v_θ, v_z, p, and b_z :

$$u^k(r) \approx \tilde{u}^k(r) = \sum_{j=1}^{2N} a_j^k h_j^k(r), \qquad k = 1, ..., 6 \tag{13}$$

where the a_j^k are coefficients to be determined and the $h_j^k(r)$ are the chosen expansion functions. This discretization yields a 'pollution-free' approximation to the entire spectrum. The Galerkin method applied here yields

$$< L_{kl}\tilde{u}^l(r), h_j^k(r) > = 0 \qquad j = 1, ..., 2N. \tag{14}$$

The error $E_j(r)$ introduced in the differential equations through the approximation $\tilde{u}^k(r)$ for $u^k(r)$, is orthogonal to every expansion function. The Galerkin method eventually leads to the general eigenvalue problem

$$\mathcal{A}\mathbf{x} = \lambda\mathcal{B}\mathbf{x}, \tag{15}$$

where the eigenvalue λ and the eigenvector of the expansion coefficients are, in general, complex. $\mathcal{A}$ is a general, non-Hermitian matrix and $\mathcal{B}$ is symmmetric and positive definite. Since $\mathcal{A}$ and $\mathcal{B}$ are real matrices, the eigenvalues occur in complex conjugate pairs. $\mathcal{A}$ and $\mathcal{B}$ have block-tridiagonal structure with a bandwidth b = 48. The dimension of the matrices is given by d = 12N - 2, where N is the number of radial intervals and is usually quite large. For details about the numerical method we refer to Ref. /7/. Since the QR algorithm

produces full matrices it can only be applied up to relatively small matrix dimensions. Inverse vector iteration preserves the band structure and thus allows treatment of very large matrices. Combining inverse vector iteration with a continuation procedure provides a very efficient method of extracting successively complete parts of the spectrum. It is emphazised that all results presented are converged; they do not change any further with mesh refinement. Typical convergence properties for the tearing mode have been presented in Ref. /7/ and for resistive Alfven modes near the complex branching point in Ref. /8/.

3. Results

3.1 Configurations with one singular surface

The discussion of the resistive Alfven spectrum after the Boris study in 1968 /9/ was only recently revived by Ryu and Grimm /10/. Their results clearly indicate the disappearence of the ideal continua in resistive MHD, but leave details unclear. Prompted by their findings, several authors have rigorously treated a simple case by WKBJ methods, namely the case of monotonic profile without current and, hence, without magnetic shear in slab geometry /11,12,14/ or in cylindrical geometry for a pressureless plasma /13/. This analytic approach has revealed that the resistive Alfven modes form a point spectrum lying on a locus which is independent of resistivity in the limit $\eta \rightarrow 0$ and which intersects the ideal continuum only at its end points. Such a simple configuration has been taken as a test case for discussing inverse vector iteration in Ref. /8/. It is, however, desirable to analyze more realistic equilibria, especially configurations with magnetic shear. A tokamak-like configuration carries a longitudinal current which contributes to the equilibrium as well as to ohmic heating. It has to satisfy the equilibrium equation, eq. 6, and contains finite pressure. For a homogeneous plasma without current and with constant toroidal magnetic field the dispersion relation for the Alfven modes, $\lambda = .5\ \left(\eta(n^2k^2 + j_{m,\nu}^2) \pm \right.$

$\sqrt{(\eta^2(n^2k^2 - j_{m,\nu}^2)^2 - \frac{4n^2k^2B_z^2}{\rho_0^2})}$, where n and m denote the toroidal and poloidal wave number and $j_{m,\nu}$ the ν^{th} zero of the Bessel function of order m, can easily be derived. For large resistivity all the modes are purely damped with negative infinity and zero as accumulation points. For the modes with few radial oscillations complex eigenvalues occur with both the oscillatory and damping parts approximating the ideal frequency for $\eta \to 0$. For an inhomogeneous configuration the ideal continuum is not degenerate, but fills a finite frequency range. Then the spectrum of the damped modes no longer forms a simple curve, but splits to form a triangle with the end points of the continuum. Purely damped modes still persist. The most rigorous treatments using the phase-integral method have been given by Refs. /14,15/. This mathematical solution is used later on to complement the numerical results and to complete the interpretation. Now the resistive Alfven spectrum is studied for a realistic equilibrium with peaked current density and constant toroidal field :

$$j_z(r) = j_0(1 - ((r/a)^2)^2, \tag{16a}$$

$$P_0(r) = \frac{j_0^2}{6}(\frac{1}{10}(1-(r/a)^{10}) - \frac{5}{8}(1-(r/a)^8) + \frac{5}{3}(1-(r/a)^6) - \frac{9}{4}(1-(r/a)^4) + \frac{3}{2}(1-(r/a)^2), \tag{16b}$$

$$B_z(r) = 1, \tag{16c}$$

$$\rho_0(r) = 1. \tag{16d}$$

For these profiles the safety factor, which is defined as usual as

$$q(r) = \frac{rkB_z(r)}{B_\theta(r)}, \tag{17}$$

assumes the form

$$q(r) = \frac{6k}{j_0((r/a)^4 - 3(r/a)^2 + 3)}. \tag{18}$$

The ratio of $q(r)$ on surface and on axis is $q(a)/q(0) = 3$. The perturbations have the wave numbers $n = 1, k = 0.2$ and $m = -2$. The constant j_0 in eq. (16) is used to vary $q(0)$ and is chosen such that the resonant surface is in the middle of the plasma; i.e. $\vec{k} \cdot \vec{B}_0(r_s) = 0$,

with $q(r_s) = 2$ and $r_s = 0.5a$. The current density and safety factor profiles are displayed in Fig. 1. For this equilibrium the ideal Alfven frequency ω_A

$$\omega_A(r) = |H(r)| = |\frac{m}{r}B_\theta + nkB_z|/\sqrt{\rho_0}, \tag{19}$$

which is plotted in Fig. 2, is not a monotonic function of r. It decreases with increasing r to zero at $r = r_s$ and then increases for $r \geq r_s$. The entire Alfven spectrum for $\eta = 10^{-5}$ and $\eta = 5 \times 10^{-6}$ is displayed in Fig. 3. The sound mode spectrum has an even more complicated structure and is concentrated close to the origin. The sound modes are not well resolved on this scale and therefore are omitted from this and the following graphs. The purely damped modes on the negative real axis with accumulation points at $\lambda_R = 0$ and $\lambda_R = -\infty$, are omitted as well. The Alfven modes have the property of incompressibility, i.e. $\nabla \cdot \vec{v} \approx 0$, and are thus easily distinguished from the sound modes. Clearly, the Alfven spectrum exhibits a more complicated structure than the very simple cases treated so far. The ideal continuum is approximated at all points where $\omega_A(r)$ has a local extremum. The uppermost branch of Fig. 3 is due to modes with eigenfunctions localized near r = a in the limit $\eta \to 0$. The second branch is formed by the corresponding modes localized near r = 0. The lowest branch reaching the origin is due to modes localized at the resonant surface. The eigenfunctions for the modes corresponding to all of these branches have different numbers of radial oscillations. For a given branch, the number of oscillations increases from the endpoints lying on the imaginary axis until the number becomes infinite at the accumulation points which correspond to $\lambda_R = 0$ and $-\infty$ on the real axis. The modes with one and two oscillations localized at r = a are examined for varying η. The dependence of the eigenvalue on η with η ranging between 10^{-2} and 10^{-5} is shown in Fig. 4. It is evident that for large η the eigenvalues for different modes lie on different curves in the complex plane which coincide only at the end points. Note that for η-values larger than 10^{-2} the modes are purely damped and no complex eigenvalue occurs. For small η-values, $\eta \leq 10^{-5}$, the eigenvalues lie on identical curves, which is evident from Fig. 3. Next we

examine the angle at which the different branches emerge from the imaginary axis. This angle is defined by the equilibrium and is not always $\alpha = 30^0$ or 45^0, as found previously /9,10,11,12,13,14/. The damping, which is defined by $\delta = -Re(\lambda)$, is considered for the different parts of the spectrum. Figure 5 shows the dependence of the first two modes of the uppermost branch, i.e. with radial node number $\nu = 1$ and 2 and localization near $r = a$. The damping δ is proportional to $\eta^{1/3}$ and the logarithmic correction discussed in Ref. /12/ is reproduced. From the eigenfunctions it is evident that the resisitivity is important only in a layer around $r = a$ with width $w \alpha \eta^{1/3}$. Figure 6a for the first mode with $\nu = 1$ shows that the part outside this layer is the ideal solution since $b_1 = rb_r$ vanishes at $r = r_s$. With increasing radial nodes, $\nu \geq 1$, the centre of the eigenfunctions gets away from $r = a$, the layer becomes wider and the ideal contribution to the eigenfunction becomes smaller, as seen for $\nu = 4$ in Fig. 6b. For highly oscillatory modes the eigenfunction is disconnected from the end point and the ideal contribution is exponentially small, as shown for $\nu = 8$ in Fig. 6c.

On the second branch with localization at the origin the damping is proportional to $\eta^{\frac{1}{2}}$ as is evident from Fig. 7 and the logarithmic correction is no longer significant. This line forms an angle of $\alpha = 45^0$ with the imaginary axis. The part of the spectrum due to modes localized at the resonant surface is actually formed by two lines, as is seen from Fig. 6. Only in the limit of very small η, say $\eta \leq 10^{-8}$, are these lines degenerated with an angle of again 30^0.

It is now time to summarize the results obtained as regards the approximation of the ideal continua. The following proposition is obvious : The ideal continua are approximated at the end points, at singular points and at local extrema of $\omega_A(r)$. The eigenvalue curves approach these points as $\delta \alpha \eta^{l/(l+2)}$, where l denotes the polynominal power of ω_A at $r = r_e$ given by $\omega_A(r) = c \cdot r_e^l + \ldots$. The uppermost branch has a linear dependence on

r and hence a damping $\delta \alpha \eta^{\frac{1}{3}}$, the second branch has a quadratic dependence due to the regularity at the origin, and hence $\delta \alpha \eta^{\frac{1}{2}}$ and the third branch again show a linear dependence as seen from Fig. 8. Configurations with $B_z(r) = B_0 r^3$ and $B_0 r^4$ while $B_\theta = 0$ give cubic and quartic dependence of ω_A on r at points $r = 0$ and yield damping proportional to $\delta = \eta^{\frac{3}{5}}$ and $\delta = \eta^{\frac{4}{5}}$, as shown in Fig. 9, in agreement with our claim. Furthermore, the equilibrium with two resonant surfaces yields evidence to support our proposition. Let us return to the discussion of the modes connected with the resonant surface. The degenerate asymptotic scaling is achieved only for very small η, $\eta \leq 10^{-8}$, and the resistive solution varies over a relatively wide radial range. This is indeed confirmed by Figs. 10 and 11, where the eigenfunctions of the first and third modes closest to the origin are displayed. Figure 11 cuts out the layer region. There are no modes with only one radial oscillation as before. It is striking that the eigenfunctions are mades up of two parts, the first part due to a solution $r < r_s$ with a wall at $r = r_s$ and the second due to the corresponding exterior solution with a wall also at $r = r_s$. The modes on the third branch (the upper one of this double line) have a radial magnetic perturbation $b_1 = rb_r$ which is even with respect to the point $r = r_s$, whereas the corresponding eigenfunctions on the fourth branch are odd. These even and odd solutions for the resistive layer are already known from the Δ' concept; see for example, /17/. The radial velocity component has just the opposite parity to b_1, as is seen in Fig. 12. With increasing damping starting from the ideal continua, the number of radial nodes in the eigenfunctions increases and the corresponding modes oscillate over an increasingly broader radial region. Near branching points the modes have a complicated structure with a specific amplitude modulation superimposed on these radial oscillations. Figure 13a and 13b display the eigenfunction near the branch point $\lambda = \lambda_*$, Fig. 13d near the other branch point $\lambda = \lambda_0$ and Fig. 13c in between. Beyond the left branch point $\lambda = \lambda_0$ the eigenfunctions oscillate over the entire radius, still having a slight amplitude oscillation. The purely damped oscillations emerging from the third branching $\lambda = \lambda_d$ towards $\lambda = 0$ and $\lambda = -\infty$ have a Bessel function type form with nearly constant

amplitude. These modes are numerically easy to compute even if the eigenvalues lie close together.

3.2 Configurations with two singular surfaces

We now discuss configurations with two singular surfaces, such as occur in the current build-up phase of tokamaks and in 'hollow' temperature and current profiles frequently observed in, for example, PLT /20/. The tearing mode stability of such configurations has been discussed in Ref. /3/. Here the resistive Alfven spectrum is analyzed. A relevant equilibrium used in Ref. /3/ is taken . It is defined by:

$$j(r) = j_0(1 + 10(r/a)^2)(1 - (r/a)^2)^3, \tag{20a}$$

$$B_z = 1, \tag{20b}$$

$$\rho_0 = 1. \tag{20c}$$

A pronounced dip occurs at the centre. These profiles are shown in Fig. 14. For $q(0) = 2.5$ the singular surfaces are located at $r/a = s_1 = 0.30$ and $r/a = s_2 = 0.73$. The ideal Alfven frequency $\omega_A(r)$ has now two zero transitions with a maximum in between at $r/a = r_e = 0.52$, as shown in Fig. 15. The resistive Alfven spectrum for this equilibrium is displayed in Fig. 16. Building up on the results discussed previously, we can easily interpret this picture. Two different values for the resistivity are used, namely $\eta = 10^{-5}$ and $\eta = 5 \times 10^{-6}$. The fact that eigenvalue curves coincide reveals that the asymptotic η limit has been reached numerically. The uppermost branch emerging from $\lambda = \omega_A(a)$ is formed by normal modes with radial localization in the eigenfunction near $r = a$ and extends to the branch point $\lambda = \lambda_0$; the second curve emerging from $\lambda = \omega_A(0)$ corresponds to modes localized near $r = 0$ and reaches the second branch point $\lambda = \lambda_{**}$. New in comparison with the previous results given in Fig. 3 is the third branch emerging from $\lambda = \omega_A(r_e)$. This

branch is due to the extremum of $\omega_A(r)$ at $r = r_e$, namely a maximum; the corresponding eigenfunctions have localized oscillations around $r/a = r_e \approx 0.50$. This branch extends up to $\lambda = \lambda_*$. This curve is actually formed by two lines which are degenerate for small η and have an angle of 45^0 with the imaginary axis. These results confirm the propostion made in the previous section. The curves emerging from $\lambda = \lambda_*$ and reaching the origin $\lambda = 0$ are due to the two singular surfaces at s_1 and s_2 and fill two double lines. It is easy to trace these lines close to the origin for small η values up to 10^{-8}, as discussed in the former case. Beyond λ_0 towards the fourth branch point $\lambda = \lambda_d$ and on the negative real axis the results are basically the same as for the case with one singular surface. Since the WKBJ analysis covers this equilibrium, too, the interpretation of the results is indeed complete.

3.3 Tearing mode

In this section, we examine the relation between tearing modes and the discrete Alven spectrum. We consider the eigenfunctions for the branch of the discrete spectrum which emerges from $\lambda = 0$. Numerically, we find that there is an eigenfunction with four oscillations and an eigenfunction with five oscillations, etc. The eigenfunctions which are even lie on one curve and those solutions with the opposite odd parity lie on a slightly displaced curve. The striking result is that there are no eigenfunctions with one, two or three oscillations. Since the tearing modes and discrete Alfven modes are both approximately incompressible, one may conjecture that the missing Alfven modes are really tearing modes. This branch of the discrete Alfven spectra occurs when two turning points are connected by an anti-Stokes line, as discussed in Section 4. The eigenfunctions are oscillatory in the middle sectors of the anti-Stokes line diagram. As $|\lambda|$ tends to zero, the region in which the eigenfunctions oscillate becomes small. If $|\lambda| \leq \eta^{\frac{1}{3}}$, the two turning points are so close that it is impossible to find valid asymptotic expansions in the domain between the two

turning points. We note that both the tearing modes and this branch of the discrete Alven spectra have a similar structure. In both types of modes, the region of nonideal MHD behaviour is used to connect two ideal MHD solutions. Thus we may apply the classical boundary layer analysis around the resonance surface. We restrict our consideration to a pressureless plasma so that we may concentrate on tearing modes and Alfven modes. In a pressureless plasma, there are no slow interchange modes. The formulas in Coppi, Greene and Johnson /18/ may be applied except on the negative real λ axis. The stable tearing mode, namely the one with odd perturbed field b_1, only exists for a marginally stable configuration. This agrees with the fact that we cannot find this mode numerically on the negative real axis among the purely damped Alfven modes. For tearing modes in a pressureless plasma, the dispersion relation simplifies to

$$\lambda = c\eta^{\frac{3}{5}}\Delta'^{\frac{4}{5}}, \tag{21}$$

where c is known constant. Thus when Δ' is positive the unstable tearing mode lies on the positive real λ axis. When Δ' is negative, the mode lies on a ray in the λ plane, which forms an angle $\pm\frac{4}{5}\pi$ with the real axis. Numerically, we confirm this behaviour by varying $j'(r = r_s)$ and thereby varying Δ' for a pressureless equilibrium defined in Ref. /19/ :

$$B_z(r) = \sqrt{B_0^2 - 1 + \frac{1}{(1+r^2)^2}}, \tag{22a}$$

$$B_\theta(r) = \frac{r}{1+r^2}, \tag{22b}$$

$$P_0(r) = 0, \tag{22c}$$

$$\rho_0(r) = 1. \tag{22d}$$

We find that the tearing mode remains on the $\pm\frac{4}{5}\pi$ rays and that the tearing mode never joins the discrete Alfven spectrum. The transition of the unstable tearing into the stable domain is shown in Fig. 17. Here q_0 is varied and the plasma extends from $r = 0$ to $r = a = 2.0$. The small deviation from the predicted curve near $\lambda = 0$ is due to insufficient

numerical resolution; the corresponding points are therefore indicated by circles. However, the mode for $q_0 = 0.70$ scales exactly to the origin as shown in Fig. 18. The eigenfunctions for an unstable and a stable mode are shown in Fig. 19. It is evident that v_r picks up one oscillation while b_r retains its shape.

4. WKBJ Analysis

The ideal Alfven and sound modes branches are described by a second-order equation, namely the Hain- Lüst equations. Resistivity raises the order of the equations to sixth order and thus leads to a singular perturbation problem. The numerical results show that the new solutions vary rapidly in the radial variable r with increasing number of radial oscillations as the resistivity decreases. The WKBJ expansion can therefore be applied to calculate the four additional formal solutions. In this section, a hard-core plasma in cylindrical geometry with conducting walls at $r = r_i$ and $r = a$ is considered. Thus the curvature terms in the MHD equations are retained but the origin, $r = 0$, is excluded. The equations are examined for a fixed λ at Alfven frequencies, as η tends to zero. Now the formal WKBJ solutions are calculated to leading order. The rapid radial oscillation behaviour of the solutions suggests the introduction of an eikonal phase factor $\exp\big((\Phi(r,\lambda)/\eta^{1/2}\big)$. Then the radial components of the velocity and of the perturbed magnetic field, v_r and b_r, have to be small, i.e. $O(\eta^{1/2})$. This scaling is chosen so that the divergence of $\vec{v}$ and $\vec{b}$ remains finite, and is confirmed further on by consistency; i.e. the fact that we can find four solutions with this property shows that the assumption is justified. Thus each of the formal WKBJ solutions has the form

$$(\vec{v}^T, p, \vec{b}^T) = (\eta^{1/2} v_r, v_\theta, v_z, p, \eta^{1/2} b_r, b_\theta, b_z) e^{\Phi(r,\lambda)/\eta^{1/2}} \tag{23}$$

The actual solutions of the differential equations may couple the formal solutions on the real interval (r_i, a). In order to obtain valid asymptotic expansions and thereby

increase the applicability of the phase-integral method, we follow the standard practice of treating the differential equations in the complex r-plane.

The resistive MHD equations, eqs. 8-10, are now written as

$$\lambda\rho_0\vec{v} = -\nabla(p + \vec{B}_0 \cdot \vec{b}) + (\vec{B}_0 \cdot \nabla)\vec{b} + (\vec{b} \cdot \nabla)\vec{B}_0, \tag{24}$$

which suggests that we introduce the total perturbed pressure.

$$p_* = p + \vec{B}_0 \cdot \vec{b} \tag{25}$$

as a variable:

$$\lambda p_* - \lambda\vec{B}_0 \cdot \vec{b} = -\gamma P_0 \nabla \cdot \vec{v} - v_r \partial_r P_0 \tag{26}$$

and

$$\lambda\vec{b} = (\vec{B}_0 \cdot \nabla)\vec{v} - (\vec{v} \cdot \nabla)\vec{B}_0 - \vec{B}_0(\nabla \cdot \vec{v}) + \eta\Delta\vec{b}. \tag{27}$$

If the vector $\vec{k} = (0, \frac{m}{r}, nk)$ is introduced, the r-component of the momentum balance yields

$$\lambda\rho_0 v_r = -\frac{\partial p_*}{\partial r} + i\vec{k} \cdot \vec{B}_0 \; b_r - \frac{2}{r} B_\theta b_\theta.$$

This equation forces p_* to be small, i.e. $p_* = O(\eta^{1/2})$, for each of the WKBJ solutions. Then the θ and z components give

$$\lambda\rho_0 v_\theta = i\vec{k} \cdot \vec{B}_0 b_\theta \tag{28}$$

and

$$\lambda\rho_0 v_z = i\vec{k} \cdot \vec{B}_0 \; b_z. \tag{29}$$

The pressure equation simplifies to

$$\lambda\vec{B}_0 \cdot \vec{b} = \gamma P_0 \; \nabla \cdot \vec{v}. \tag{30}$$

Thus, with $\vec{b}_* = (0, b_\theta, b_z)$, the magnetic field equation becomes

$$\lambda^2 \vec{b}_* = -H^2(r)\vec{b}_* - \lambda^2 \frac{\vec{B}_0 \cdot \vec{b}}{\gamma P_0} \vec{B}_0 + \lambda \Phi'^2 b_* \tag{31}$$

for $P_0(r) \neq 0$, where

$$H(r) = \frac{\vec{k} \cdot \vec{B}_0}{\sqrt{\rho_0}} \tag{32}$$

is the equilibrium quantity related to the ideal Alfven frequency, introduced in eq. 19.

This equation has two types of solution. The Alfven formal solutions satisfy

$$\vec{B}_0 \cdot \vec{b} = O(\eta^{1/2}), \tag{33a}$$

$$\Phi_A'^2 = \frac{\lambda^2 + H^2(r)}{\lambda}. \tag{33b}$$

The slow-wave solutions satisfy

$$\vec{B}_0 || \vec{b}, \tag{34a}$$

$$\Phi_S'^2 = \frac{1}{\lambda}(\lambda^2(1 + \frac{B^2}{\gamma P_0}) + H^2(r)). \tag{34b}$$

To leading order, the Alfven solutions are incompressible and the perturbed pressure is small. In addition to these four formal WKBJ solutions, there are two formal solutions which satisfy $\Phi'(r, \lambda) = 0$. These two formal solutions approach solutions of the ideal MHD equations as $\eta^{1/2}$ tends to zero.

We wish to calculate the normal modes using these asymptotic expansions. However, these formal solutions may not be valid. The actual solutions may couple the formal solutions. The reason for this is that $\Phi(r, \lambda)$ is complex and thus there are exponentially growing solutions. We restrict our consideration to sufficiently small β equilibria and λ at Alfven frequencies. In this case the slow-wave solutions vary more rapidly in space than do the other solutions. The general theory of valid WKBJ expansions shows that the slow wave solutions do not couple to the other solutions /15/. For unstable λ, all the expansions are valid and no new unstable modes occur.

For stable λ, we must analytically continue the equations and the expansions into the complex plane in order to obtain valid asymptotics. As in the theory of WKBJ expansions for second-order equations, the asymptotic expansions have resonant denominators at the turning points where $\Phi'(r,\lambda) = 0$. The region around the turning point is divided into three sectors by anti-Stokes lines, curves on which $Re\Phi$ is constant. The ideal MHD solutions are valid in any proper subsector (excluding a small region with width $\eta^{1/2}$ around the anti-Stokes lines) of two sectors, the WKBJ solutions are valid in all three sectors, except near the turning point and near one anti-Stokes line, provided $\exp(\Phi/\eta^{1/2})$ is exponentially small in the sector opposite to the anti-Stokes line. If the domain of interest contains all three sectors, the ideal MHD solutions couple to the WKBJ solutions. We calculate the normal modes directly, using the valid asymptotic expansion, and find that normal modes occur when one of the following criteria is satisfied: (1) $Re\Phi(r_i,\lambda) = Re\Phi(a,\lambda)$; (2) an anti-Stokes line intersects r_i or a and a second anti-Stokes line from the same transition point crosses (r_i, d); (3) two transition points are connected by an anti- Stokes line. These three criteria specify curves in the λ-plane where point eigenvalues accumulate with a density of $\eta^{1/2}$ and these curves are independent of η. Normal modes also occur when $|\lambda| \leq \eta^{1/3}$ (slow interchange and tearing modes) and on the stable imaginary axis. Direct calculation, using the valid asymptotic expansions, shows that the only other normal modes on an Alfven time scale are the point eigenvalues of ideal MHD. We note that the curves on which the discrete Alfven spectra lie are determined only to within $\eta^{1/2}$ by the first two criteria and within $\eta^{1/3}$ by the third. It is necessary to carry the calculation to a higher order if one wishes to determine the fine structure, such as the splitting of a curve into several different curves separated by $\eta^{1/2}$.

The eigenfunctions for those modes which satisfy the first criterion are highly oscillatory in the entire domain (r_i, a) and therefore damp rapidly in time. The eigenfunctions for those modes which satisfy the second criterion are highly oscillatory near one endpoint

and behave as ideal MHD-solutions near the other endpoint. Since the second criterion is satisfied when a turning point lies on an endpoint, the normal modes which satisfy criterion two lie on curves in the λ-plane which emerge from the endpoints of the ideal continua. The eigenfunctions for those modes which satisfy the third criterion behave as ideal MHD solution near both endpoints and are oscillatory in the middle of (r_i, a). Since the third criterion is satisfied when two turning points merge, the curves of normal modes which satisfy the third criterion emerge from 'double turning point' points. These 'double turning point' points occur at a resonant surface; $\omega_A = H(r_s) = 0$ and at a relative maximum of $\omega_A(r)$. The eigenfunctions which oscillate rapidly in a large region of (r_i, a) damp faster than those solutions which oscillate only in a small region. Since the WKBJ solutions grow exponentially as a function of radius, the amplitude of the WKBJ oscillations will be much larger than the amplitude of the nonoscillatory part of the eigenfunction when λ_R is large. Each eigenfunction of the discrete Alfven spectrum has its spatial maximum when $\mathrm{Re}\Phi\prime(r, \lambda) = 0$. This expression simplifies to $|\lambda|^2 = H^2(r)$, but λ is complex for these modes. It is possible to compute the exact location of these discrete Alfven spectra by numerically evaluating each criterion which we have given. However, this requires in general the use of sophisticated interactive programs in which the user must repeatedly guess values of λ as input; see, for example, /16/. Since we have already computed these curves numerically, we only need to complement these data by determining the qualitative shape of the curves containing the spectra. This is done by examining the geometry of the anti-Stokes lines. We follow the geometry of the anti-Stikes lines along these curves of spectra to determine how the curves begin, intersect and terminate as well as to determine the general shape of the curves.

If $\vec{k} \cdot \vec{B}_0(r) \neq 0$ and $H(r)$ is monotonic, there is only one transition point. For $\lambda = \omega_A(a)$ the transition point is located at the end point. There is a curve in the λ-plane (namely the uppermost branch in Fig. 3) on which one of the anti-Stokes lines of the

transition point passes through the end point a in the complex r-plane. By constantly decreasing λ_I and increasing $|\lambda|_R$ the second anti-Stokes line moves to the right and eventually hits end point r_i at $\lambda = \lambda_0$ (Fig. 20a). Once the second anti-Stokes line passes r_i, all asymptotic expansions are valid and normal modes cease to exist on this curve in the λ-plane. By decreasing λ_R and continuing to increase λ_I a second curve containing spectra is generated. This curve then consists of those λ which have one anti-Stokes line hitting the end point r_i and one anti-Stokes line crossing (r_i, a). The boundaries of this curve are $\lambda = \lambda_0$ and $\lambda = \omega_A(r_i)$. A third curve of spectral points emerge from λ_0 and extends to the negative real axis. This third curve consists of points with $\mathrm{Re}\Phi(r_i, \lambda) - \mathrm{Re}\Phi(a, \lambda) = 0$ and on this curve $|\lambda_R|$ increases so that the transition point moves further away from the real axis. Furthermore normal modes occur on the negative real axis with density $\eta^{-1/2}$ and with accumulation points $\lambda = 0$ and $\lambda = -\infty$. Note that for finite viscosity the accumulation point is moved away from the origin to $\min_{r\in(r_i,a)} \left(\frac{2\sqrt{\rho_0(r)\eta\mu}H(r)}{|\mu-\eta\rho_0(r)}\right)$, where μ is the viscosity. For a monotonic $H(r)$ profile with no singular surface we thus obtain the typical Λ shape for the eigenvalues curve as discussed in Refs. /10,11,12,13,14,15/.

If $\vec{k} \cdot \vec{B}_0(r_s) = 0$ and $H(r)$ is monotonic, then two relevant turning points exist. These transition points cross (r_i, a) only for imaginary λ. For small stable λ the two transition points labelled T_1 and T_2 are on opposite sides of (r_i, a). A spectral curve, defined by the connection of the two transition points by an anti-Stokes line, emerges from $\lambda = 0$ (Fig. 21a). At $\lambda = \lambda_*$ one of the two anti-Stokes lines hits the other end point r_i (Fig. 21b); then only one transition point enters the problem, and normal modes will no longer occur on this spectral curve. There are two different ways to disconnect the anti-Stokes line from the transition points: 1) By increasing λ_I and decreasing $|\lambda_R|$ the transition point closer to r_i can be connected to r_i by an anti-Stokes line (Fig. 21c), and this generates a curve of spectrum which ends at $\lambda = \omega_A(r_i)$. 2) By increasing λ_I and $|\lambda_R|$ we can generate a second curve of spectrum; this curve consists of those λ which

have an anti-Stokes line connecting the second transition point T_2 with r_i (Fig. 21d). At $\lambda = \lambda_0$, when the second anti-Stokes line of the second transition point T_2 hits the other end point a, the normal modes cease to occur on this curve. Fig. 22 resembles Fig. 20 in the case where $\vec{k} \cdot \vec{B}(r) \neq 0$. There are two more curves of spectrum; the first is generated by the anti-Stokes line of the second transition point T_2, crossing the second end point. The second curve is defined by $Re\Phi(a, \lambda) - Re\Phi(r_i, \lambda) = 0$. The second curve hits the imaginary axis and spectra exist on the stable real axis as well. These curves of spectrum match the numerical results in Fig. 3.

5. Discussion

The study of the linearized motion around an equilibium state reveals the properties of ideal and resistive MHD. Naturally, analytic survey is applied first, yielding both basic concepts as well as complete results for sufficiently simple configurations. The resistive stability in terms of boundary layer analysis is such a sophisticated concept; the stability criteria have brought progress, too. However, these concepts do not solve the problem of wave propagation in resistive MHD.

The normal mode analysis yields the most complete insight into the plasma behaviour. The development of the ideal spectral codes in 1D and 2D, such as PEST and ERATO, has proved that a good enough discretization can be achieved to discuss analytical results in detail, to extend those and to stimulate new areas. The study and interpretation of the ideal continua, the Alfven and slow-mode continua, serves as an example of fruitful combination of analytical and numerical work. The understanding of the ideal Alfven continuum is important, because it plays a crucial role in Alfven wave heating interpreted as a phase-mixing phenomenon. In contrast to the detailed analysis of the ideal MHD continua, the investigation of the resistive Alfven spectra is still in its preliminary phase. One rea-

son is obviously the degree of complexity. The set of resistive equations form a sixth-order system which is too complicated for complete analytical solution. The initial-value codes usually used for numerical solution do not give the stable part of the spectrum. Only recently the resistive MHD spectrum has been solved numerically. The basic result has been that the ideal continuua disappear for finite resistivity and are approximated only at the end points and that the eigenvalues lie on specific curves. These findings have provided the stimulus to address the problem analytically in terms of WKBJ theory; a complete solution confirming the previous numerical results has been constructed for the simple case of of a monotonic $B_z(r)$ profile yielding a monotonic $\omega_A(r) = |\vec{k} \cdot \vec{B}/\sqrt{\rho_0}|$. More relevant and, hence, more complicated equilibrium profiles need to be analyzed thoroughly in order to complete the picture with respect to the resistive spectrum. This is the objective of the present work in which tokamak-like configurations in cylindrical symmetry with one and two singular surfaces are examined. Complete results are given by a combined effort involving numerical and mathematical treatment.

The spectrum of resistive MHD is evaluated numerically by a nonvariational approach by applying the Galerkin procedure in conjunction with finite elements. This approach culminates in the complexe eigenvalue problem $\mathcal{A}\mathbf{x} = \lambda\mathcal{B}\mathbf{x}$. Careful comparison with the discretized ideal spectrum as well as with exact resistive solutions have confirmed that a good discretization has been established. In conjunction with convergence studies using increasingly finer mesh size, this numerical scheme guarantees high accuracy. All details presented consist of converged results. It is evident that the value of the resistivity is small enough for discussing the asymptotic behaviour. Further decreasing the value of η which would require more spatial resolution yields only a higher point density on the eigenvalue curves, but does not give qualitativly new results. In that sense, the numerical answer is complete. Instead of arguing about the proper numerical value for η a complementary approach is included.

The oscillatory behaviour of the resistive normal modes suggests the introduction of an eikonal factor $\exp(\Phi(r,\lambda)/\eta^{1/2})$ and, hence, the phase-integral method. The turning points and the anti- Stokes lines pattern yield the spectrum by means a quantization condition such as $\int_{z_1}^{z_2} \Phi^{1/2}\, dz = in\pi$. However, only for very simple profiles this quadrature is trivial. For general configurations, the anti-Stokes lines have to be found numerically. The evaluation of the spectrum is therefore quite involved. However, for the cases under consideration the eigenvalue curves have already been found numerically. Consequently, this part is considered an unnecessary complication for the WKBJ solution. The analytical treatment is rigorous and the discussion of the anti-Stokes line pattern complete. The end points of the resistive Alfven curves and the characteristics of the curves including their branching points are derived accurately, the actual values being filled in numerically. For the different branches of the resistive Alfven modes the behaviour of the eigenfunctions is extracted and displayed in terms of computed solutions.

Our results can be summarized as follows: The resistive Alfven modes form a point spectrum; the modes experience finite damping. The eigenvalues lie on specific curves in the complex plane with a width proportional to $\eta^{1/2}$, hence, in the limit of asymtotically small resistivity these curves practically coincide and become independent of η. The point density on these curves is proportional to $\eta^{-1/2}$. The ideal continua are approximated only at their endpoints and specific interior points, namely at singular surfaces and at extrema of $\omega_A(r)$. The eigenfunctions consist of resistive and ideal parts with localization around the points where the ideal continuum is approximated.With increasing damping, i.e. further away from the continuum, the number of radial oscillations occur over a wider radial interval. For the same amount of damping, the number of oscillations increases in the resistive part of the solutions for decreasing η. The oscillatory part has a maximum at specific radial points. The ideal solution soon becomes exponentially small. Eventually, the eigenfunctions oscillate over the entire radius. For eigenvalues between branching

points, the eigenfunctions show complicated radial dependence owing to the influence from different sides. The modes which form the branches emerging from the origin owing to the singular surfaces miss the fundamental radial nodes $\nu = 1,2$ and 3. Starting with four radial oscillations, these modes comprise two components, each with a wall at $r = r_s$. Finally, purely damped modes evolve with accumulation points at $\lambda = 0$ and $-\infty$. The radial oscillations now have constant amplitude.

Since the discrete Alfven modes and the tearing modes are both approximately incompressible, the transition of a tearing mode in the stable region is examined for a pressureless plasma. It is found that the stable tearing modes stay on the rays predicted by boundary layer theory and never join the Alfven spectrum. So far, no unstable oscillatory modes have been found for the incompressible branch. But we cannot prove this in general. We believe that the question whether there can be two unstable tearing modes should be addressed first. If so, it should be possible to drive these modes overstable. Such overstable modes should then be subject to oscillatory behaviour.

For small pressure in the equilibrium, the perturbed pressure is small and the Alfven and slow-mode branches decouple. This is evident from Fig. 3, where the location of the resistive sound modes is indicated. As the set of the compressible equations is more complicated, the complete analytical treatment is far more difficult. It may be conjectured that the basic behaviour is similar to the discrete Alfven spectrum. This has indeed been confirmed by numerical calculations so far. But the singular surfaces and the boundary where the pressure vanishes introduce new complications. Although less important owing to their small frequency, the sound modes should be treated rigourosly, too, in order to complete the understanding of resistive MHD. The compressible modes are important for the question of stability, especially at the β-limits.

To summarize, it can be stated that there are no continuum modes in resistive

MHD. The logarithmic singularities in the ideal eigenfunctions are changed drastically towards oscillatory solutions, not just locally, as one might have expected. In order to estimate the effect on the Alfven wave heating scheme by the continuous spectrum, it has to be kept in mind that the heating problem is not an eigenvalue problem, but an inhomogenous boundary value problem with a given frequency. A thorough discussion of the heating problem treated in the context of resistive MHD requires treatment of the initial value problem and presents a new issue.

References

/1 / H.P. Furth, J. Killen, M.N. Rosenbluth, Phys. of Fluids 6, 459 (1963)

/2/ H. Tasso, J.T. Virtamo, Plasma Physics 22, 1009 (1980)

/3/ W. Kerner, H. Tasso, Plasma Physics 24, 97 (1982)

/4/ W. Kerner, H. Tasso, Comp. Phys. Com. 24, 407 (1981)

/5/ W. Kerner, H. Tasso, Phys. Rev. Lett. 49, 654 (1982)

/6/ W. Kerner, H. Tasso, 9^{th} International Conference on Plasma Physics and Controlled Nuclear Fusion Research, Baltimore, USA, September 1-8, 1982, paper P 2-2

/7/ W. Kerner, K. Lerbinger, R. Gruber and T. Tsunematsu, Comp. Phys. Com. 36, 225 (1985)

/8/ W. Kerner, K. Lerbinger, J. Steuerwald, to appear in Comp. Phys. Com., IPP 6/236 (1984)

/9/ J.P. Boris, Ph.D. Dissertation, Princeton University, 1968

/10/ C.M. Ryu, R.C. Grimm, J. of Plasma Physics 32, 207 (1984)

/11/ D. Lortz, G. Spies, Phys. Lett. A 101, 335 (1984)

/12/ D. Lortz, G. Spies, 10^{th} International Conference on Plasma Physics and Controlled Nuclear Fusion Research, London, UK, September 12-19, 1984, paper E III-11

/13/ R. Dewar, B. Davis, J. of Plasma Physics 32, 443 (1984)

/14/ Y.P. Pao, W. Kerner, Phys. of Fluids 28, 287 (1985)

/15/ K. Riedel, Ph.D. Dissertation, Courant Institute, 1985

/16/ R.B. White, J. of Comp. Phys. 31, 409 (1979)

/17/ J.M. Greene, Report LRP 114/76 Ecole Polytechnique Federale de Lausanne, Centre de Recherches en Physique des Plasmas

/18/ B. Coppi, J.M. Greene, J.L. Johnson, Nucl. Fusion 6, 101 (1966)

/19/ H.P. Furth, P.H. Rutherford, H. Selberg, Phys. of Fluids 16, 1054 (1973)

/20/ N.R. Sauthoff, S. von Goeler, W. Stodiek, PPPL-1379 (1977), Princeton, N.J.

Figure Captions

Figure 1 :

Safety Factor q and current density J profile for a tokamak-like equilibium with one singular surface $q = 2$ at $r_s = 0.5a$.

Figure 2 :

Ideal Alfven frequency $\omega_A(r) = |\frac{m}{r}B_\theta + nkB_z| \; / \; \sqrt{\rho_0}$ for wave numbers $m = -2, n = 1$ and $k = 0.2$.

Figure 3 :

Resistive Alfven mode spectrum for the tokamak-like equilibrium with one singular surface for values of the resistivity $\eta = 10^{-5}$ ($\cdot$) and $\eta = 5 \cdot 10^{-6}$ (x). The sound modes have much smaller eigenfrequencies as is indicated by the box close to the origin. The purely damped modes on the negative real axis have been omitted.

Figure 4 :

Frequency of the first two modes from the uppermost branch in Fig. 3 for different η ranging from $\eta = 10^{-5}$ to $\eta = 10^{-2}$.

Figure 5 :

Scaling of the damping $\delta = -Re(\lambda)$ with respect to η for the first two modes from the uppermost branch in Fig. 3; ν labels the number of radial nodes.

Figure 6 :

Eigenfunctions of the first mode of the uppermost branch in Fig. 3 for $\eta = 5 \cdot 10^{-6}$; $v_1 = rv_r$ and $b_1 = irb_r$ denote the radial components of velocity and perturbed magnetic field; ν labels the number of radial nodes.

a) $\nu = 1$

b) $\nu = 4$

c) $\nu = 8$

Figure 7 :

Scaling of the damping $\delta = -Re(\lambda)$ with respect to η for the first two modes from the second branch in Fig. 3; ν labels the number of radial nodes.

Figure 8 :

Scaling of the damping $\delta = -Re(\lambda)$ with respect to η for the first two modes from the third and forth branch in Fig. 3 emerging from the origin; ν labels the number of radial nodes.

Figure 9 :

Scaling of the damping $\delta = -Re(\lambda)$ with respect to η for equilibria with $B_z(r) = B_0 \cdot r^3$ and $B_z(r) = B_0 \cdot r^4$ with $\delta \; \alpha \; \eta^{3/5}$ and $\eta^{4/6}$.

Figure 10 :

Eigenfunctions of modes on the double line emerging from the origin in Fig. 3 for $\eta = 10^{-8}; v_1 = rv_r$ and $b_1 = irb_r$ denote the radial components of velocity and perturbed magnetic field

a) third branch and first mode, $\nu = 4$

b) third branch and third mode, $\nu = 6$

Figure 11 :

Eigenfunctions of modes on the double line emerging from the origin in Fig. 3 for $\eta = 10^{-8}$ in an enlarged scale ; $b_1 = irb_r$ denotes the radial component of the perturbed magnetic field

a) third branch and first mode, $\nu = 4$

b) fourth branch and first mode, $\nu = 4$

c) third branch and second mode, $\nu = 5$

d) fourth branch and second mode, $\nu = 5$

Figure 12 :

Eigenfunctions of the second mode of the fourth branch for $\eta = 10^{-8}$; $v_1 = irv_r$ denotes the radial component of the velocity.

Figure 13 :

Eigenfunctions of modes of Fig. 3; $v_1 = rv_r$

a) right to the branch point λ_*

b) left to the branch point λ_*

c) between the branch points λ_* and λ_0.

d) left to the branch point λ_0

Figure 14 :

Safety Factor q and current density J profile for a tokamak-like equilibium with two singular surfaces $q = 2$ at $s_1 = 0.30a$ and $s_2 = 0.73a$.

Figure 15 :

Ideal Alfven frequency $\omega_A(r) = |\frac{m}{r}B_\theta + nkB_z| \; / \; \sqrt{\rho_0}$ for the equilibrium of Fig. 14 for wave numbers $m = -2, n = 1$ and $k = 0.2$.

Figure 16 :

Resistive Alfven mode spectrum for the tokamak-like equilibrium with two singular surface for values of the resistivity $\eta = 10^{-5}$ ($\cdot$) and $\eta = 5 \cdot 10^{-6}$ (x). The sound modes being close to the origin and the purely damped modes on the negative real axis have been omitted.

Figure 17 :

Eigenvalues of the tearing mode for the pressureless equilibrium defined in eq.(22a-22d) with $\eta = 10^{-6}$ for different values of q_0 which implies different values for Δ'. The stable modes lie on a ray emerging from the origin under an angle of $\frac{4}{5}\pi$ with the positive real axis.

Figure 18 :

Scaling of the complex eigenvalue of the stable tearing mode with $q_0 = 0.70$ in the pressureless equilibrium defined in eq.(22a-22d)

a) the eigenvalues are lying on a ray which forms an angle of $\frac{4}{5}\pi$ with the imaginary axis.

b) the real part of λ scales like $Re(\lambda)\ \alpha\ \eta^{\frac{3}{5}}$

Figure 19 :

Eigenfunctions of the tearing mode for the pressureless equilibrium defined in eq.(22a-22d) with $\eta = 10^{-6}$; $v_1 = rv_r$ and $b_1 = irb_r$ denote the radial component of the velocity and the perturbed magnetic field

a) unstable tearing mode for $q_0 = 0.90$

b) stable tearing mode for $q_0 = 0.70$

Figure 20 :

One anti-Stokes line crosses the endpoint $r = a$ and the other crosses at an interior point $r \in (r_i, a)$ (dotted line). If the second anti-Stokes line crosses at the other end point $r = r_i$ (solid line) the limiting spectral point λ_0 is reached. This anti-Stokes diagramm describes the spectral curve emerging from $\lambda = \omega_a(a)$ to $\lambda = \lambda_0$ in Fig. 3.

Figure 21a :

Two turning points, T_1 and T_2, connected by an anti-Stokes line. This anti-Stokes diagramm describes the spectral curve emerging from $\lambda = 0$ in Fig. 3.

Figure 21b :

Anti-Stokes diagramm at $\lambda = \lambda_*$.

Figure 21c :

Anti-Stokes diagramm for the spectral line from $\lambda = \lambda_*$ to $\lambda = H(r_i)$.

Figure 21d :

Anti-Stokes diagramm for the spectral line from $\lambda = \lambda_*$ to $\lambda = \lambda_0$.

Figure 22 :

Anti-Stokes diagramm at $\lambda = \lambda_0$.

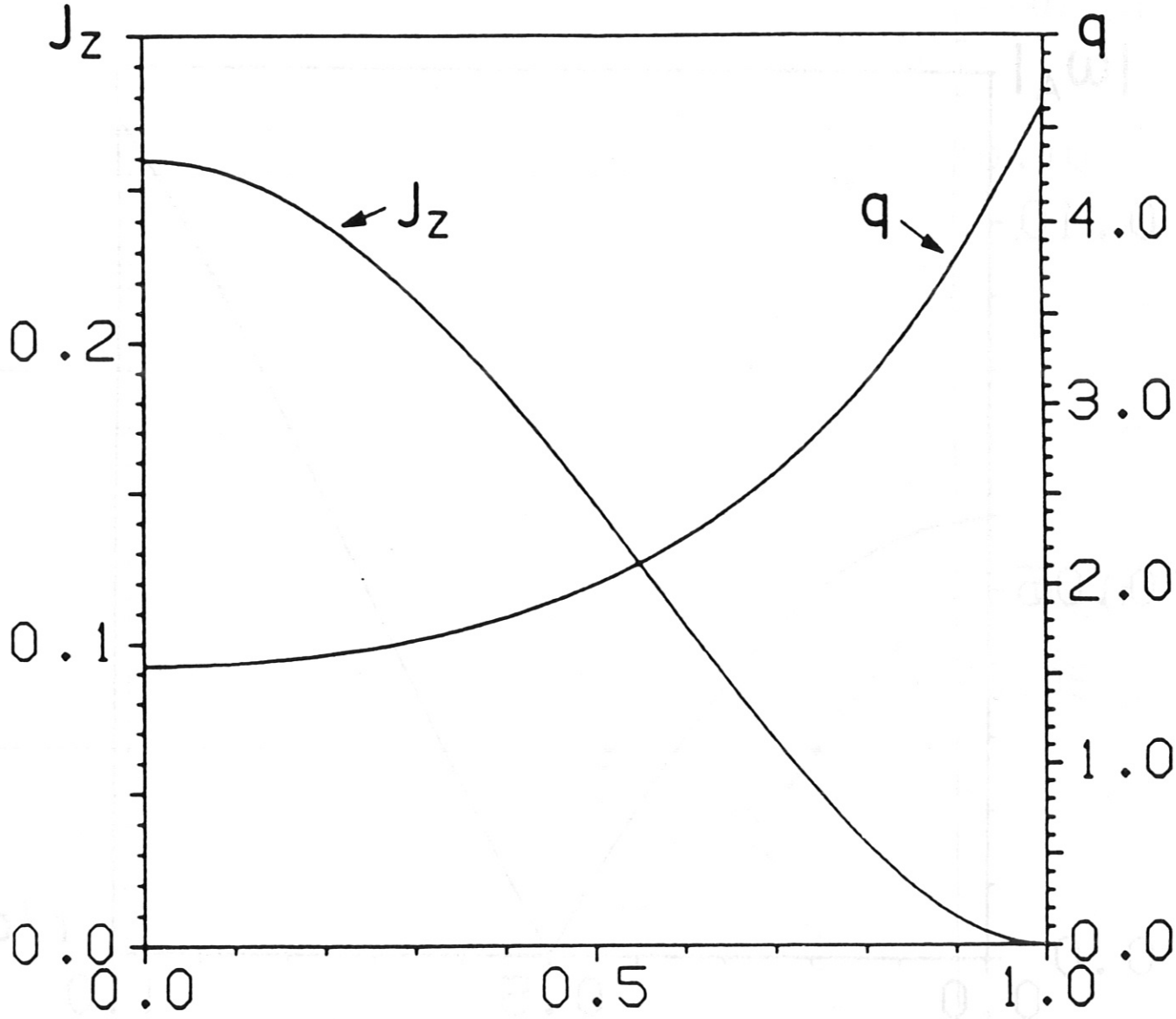

Fig 1

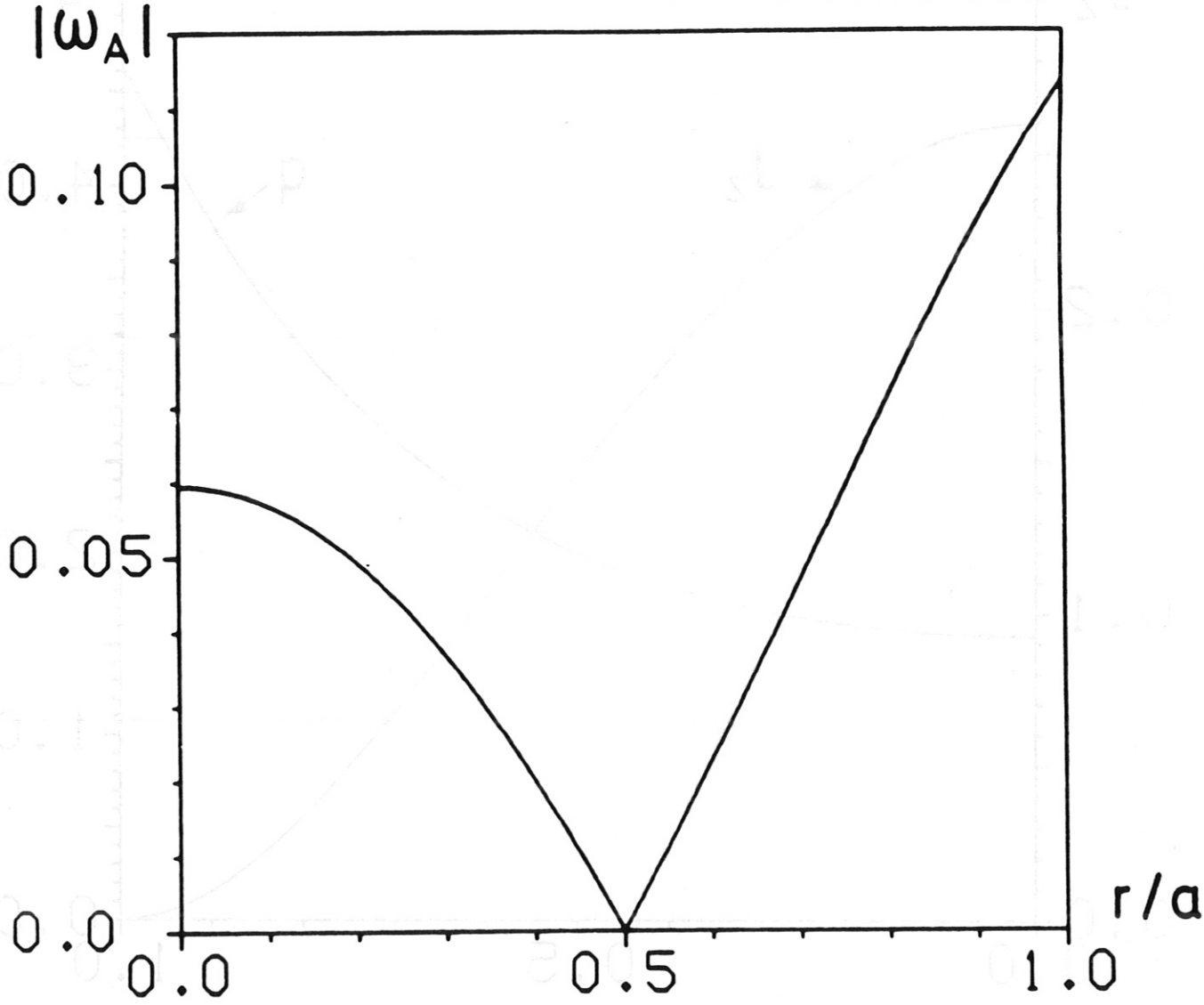

Fig 2

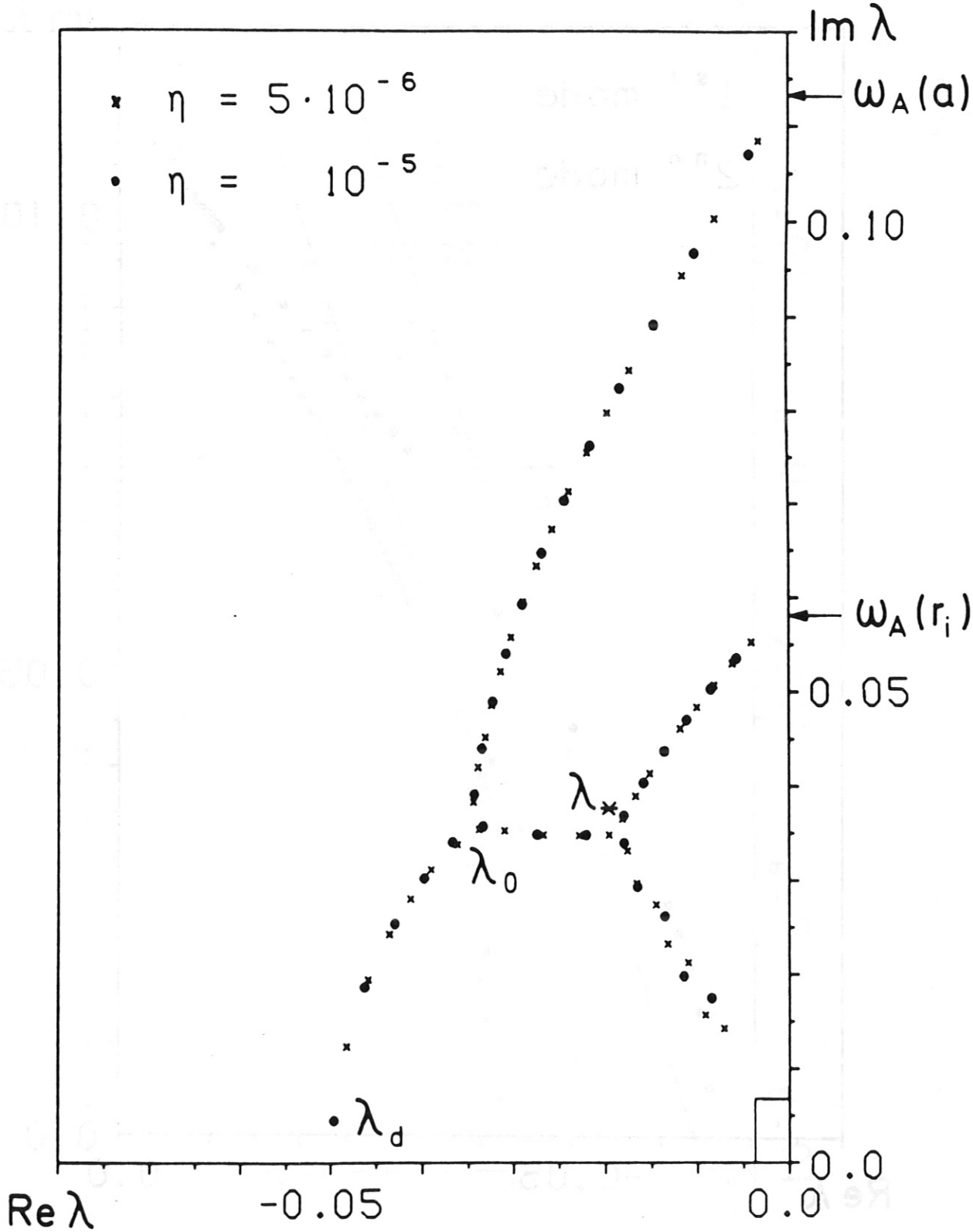

Fig 3

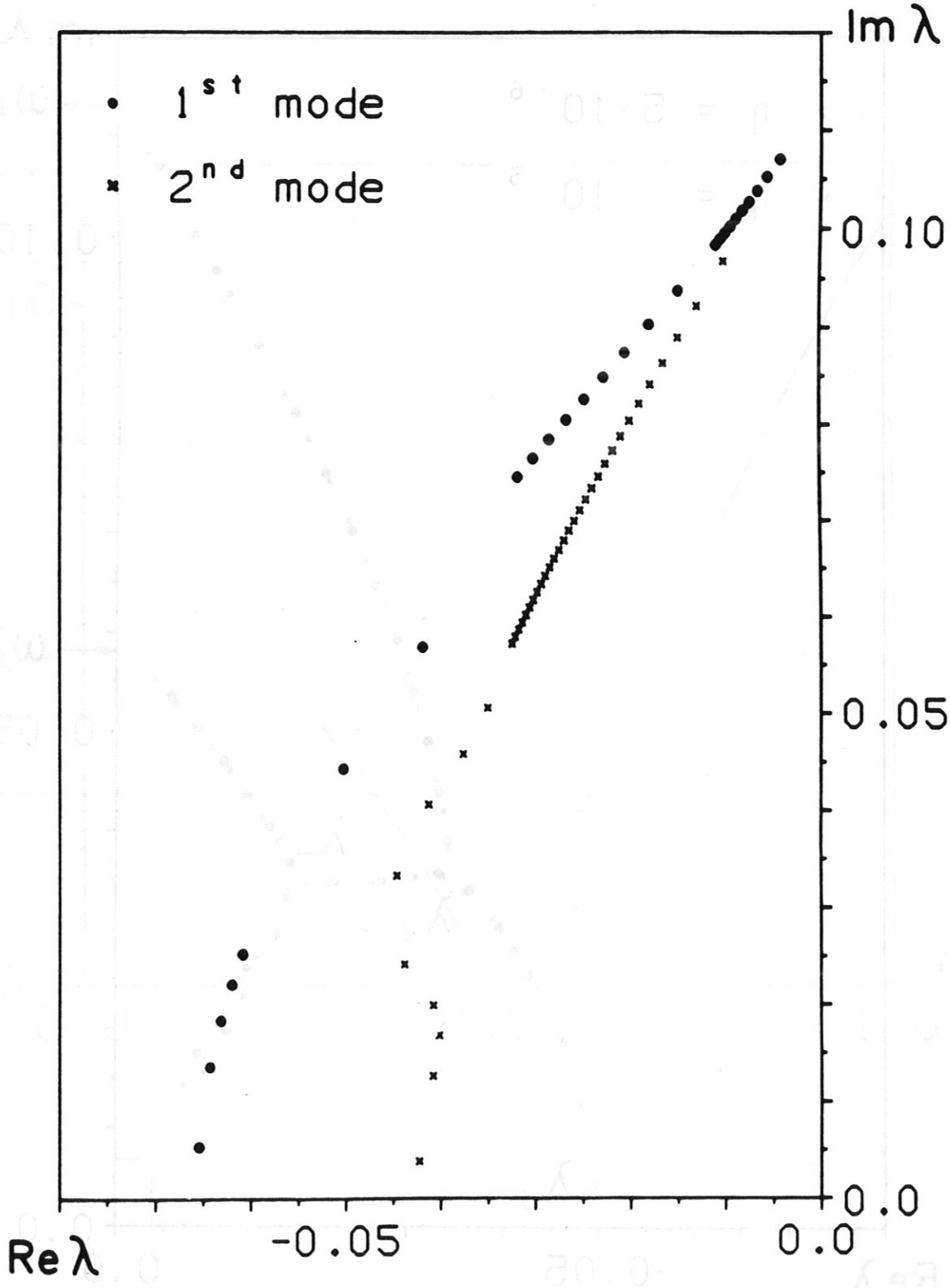

Fig 4

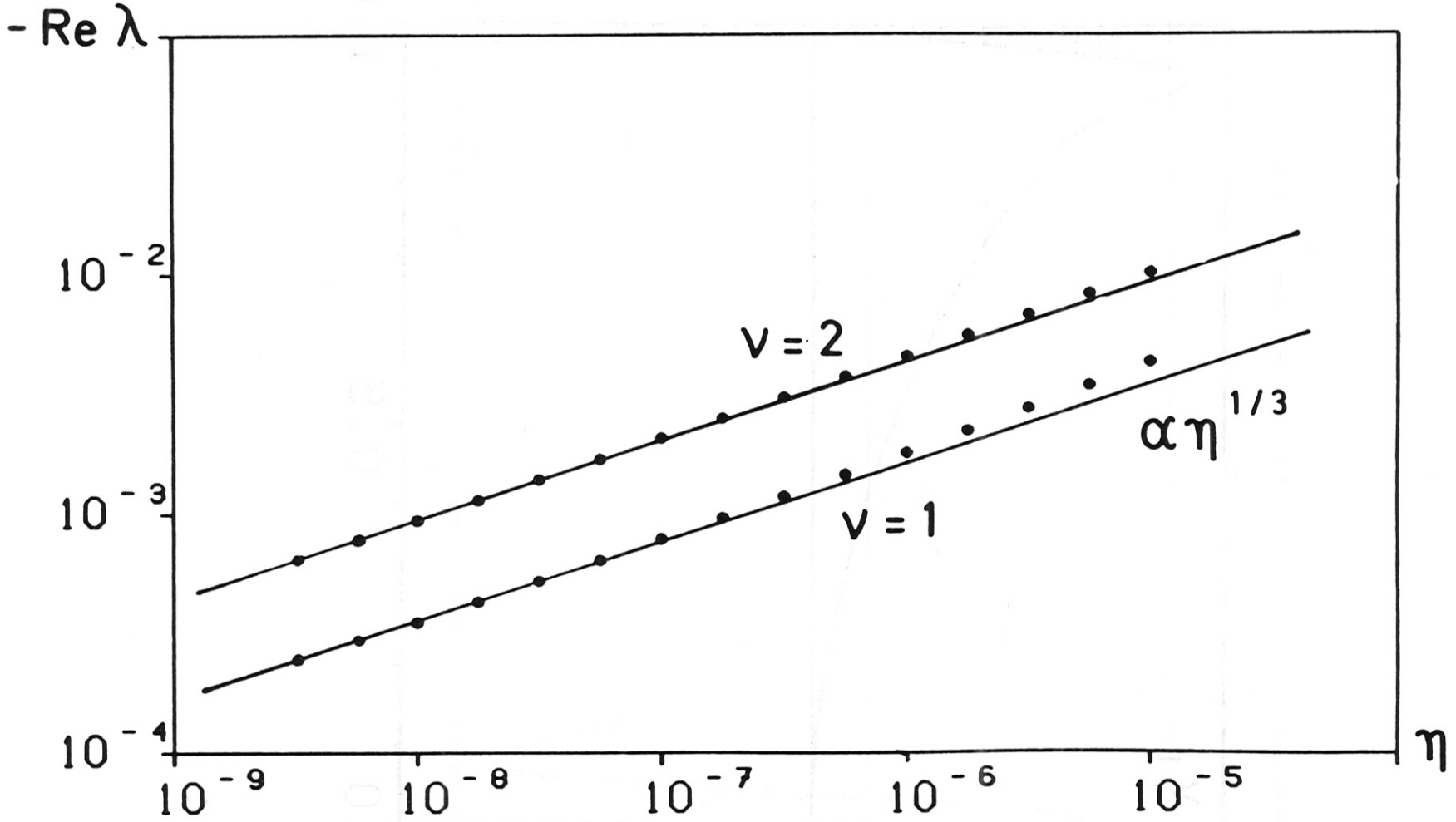

Fig 5

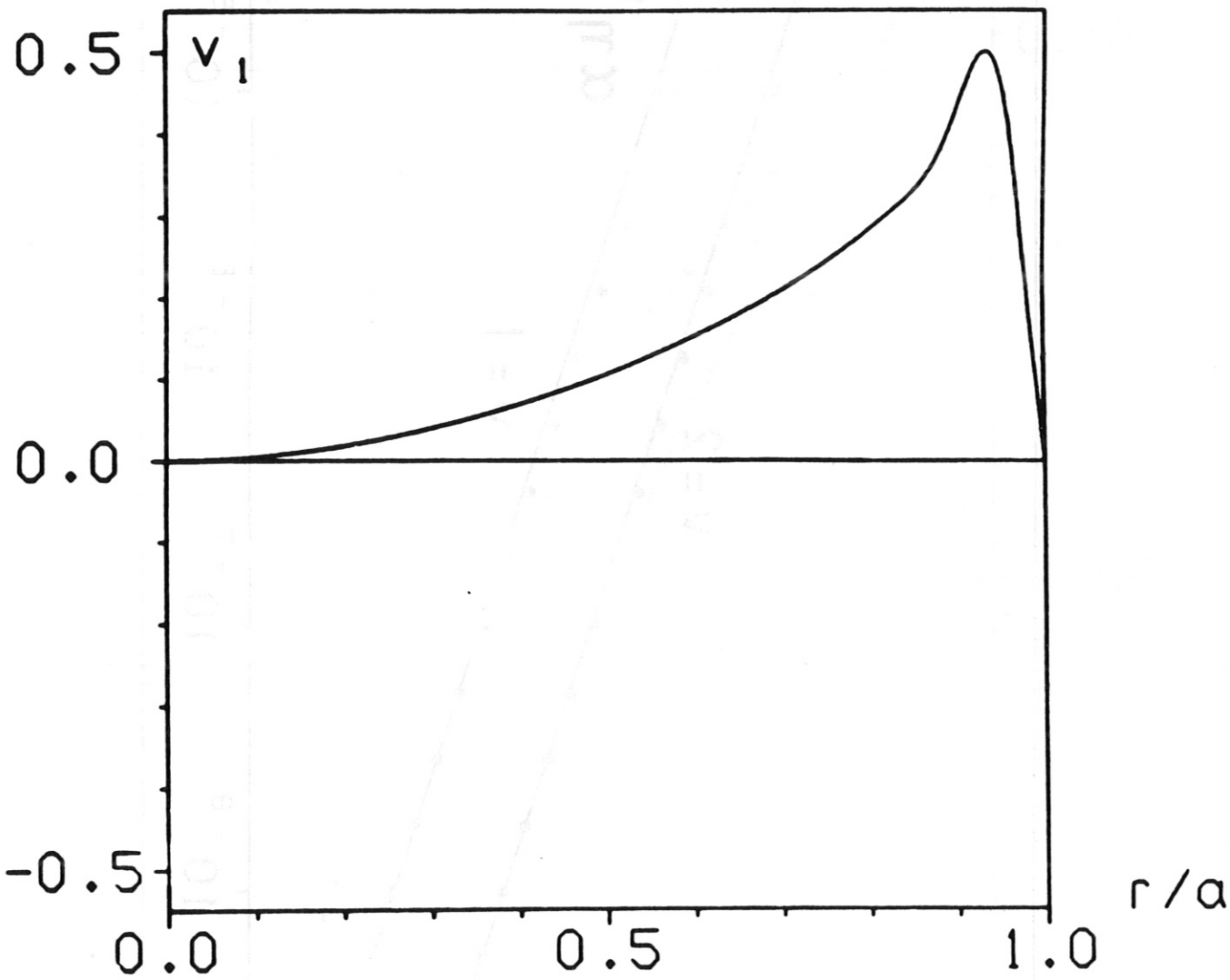

Fig 6a

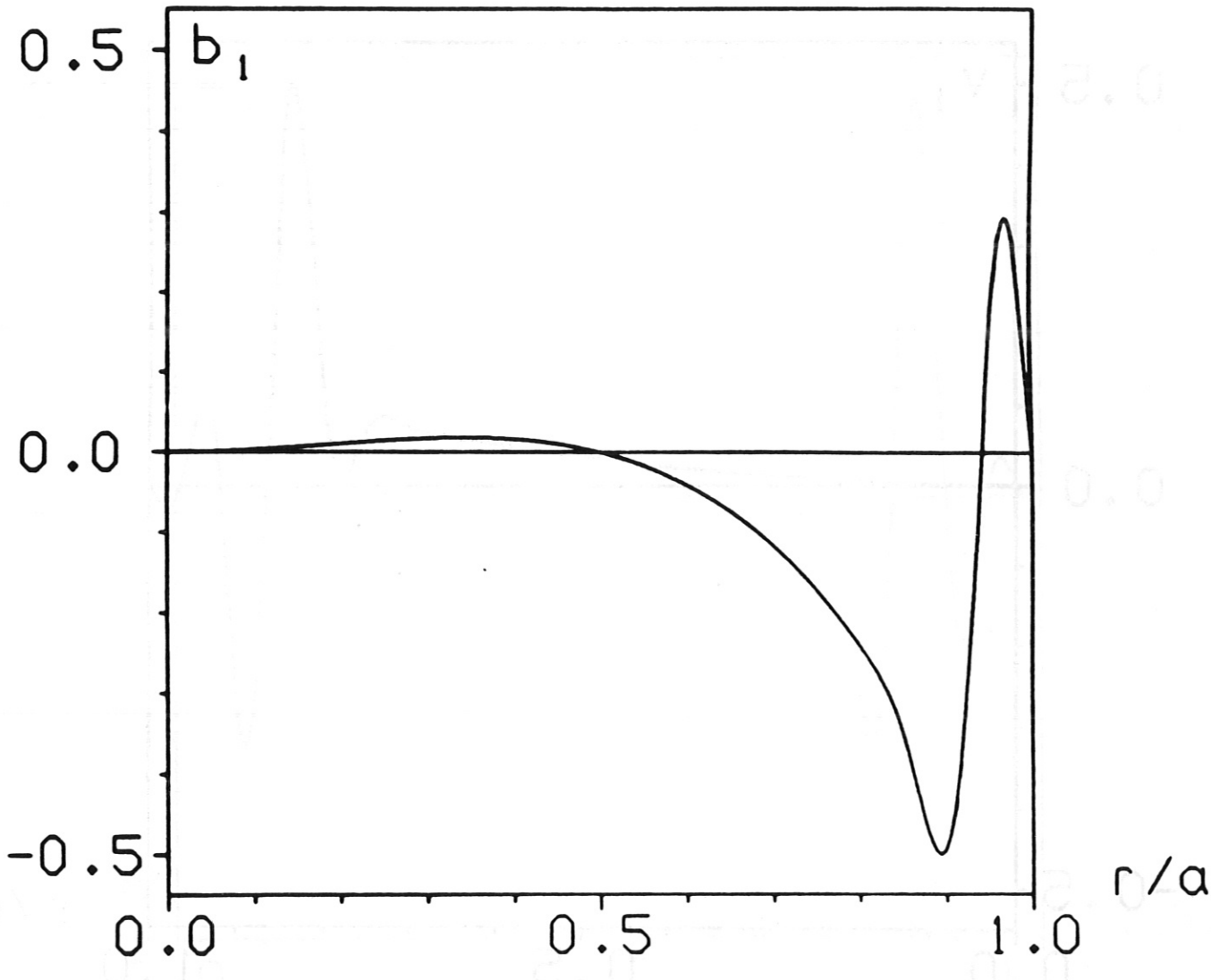

Fig 6a

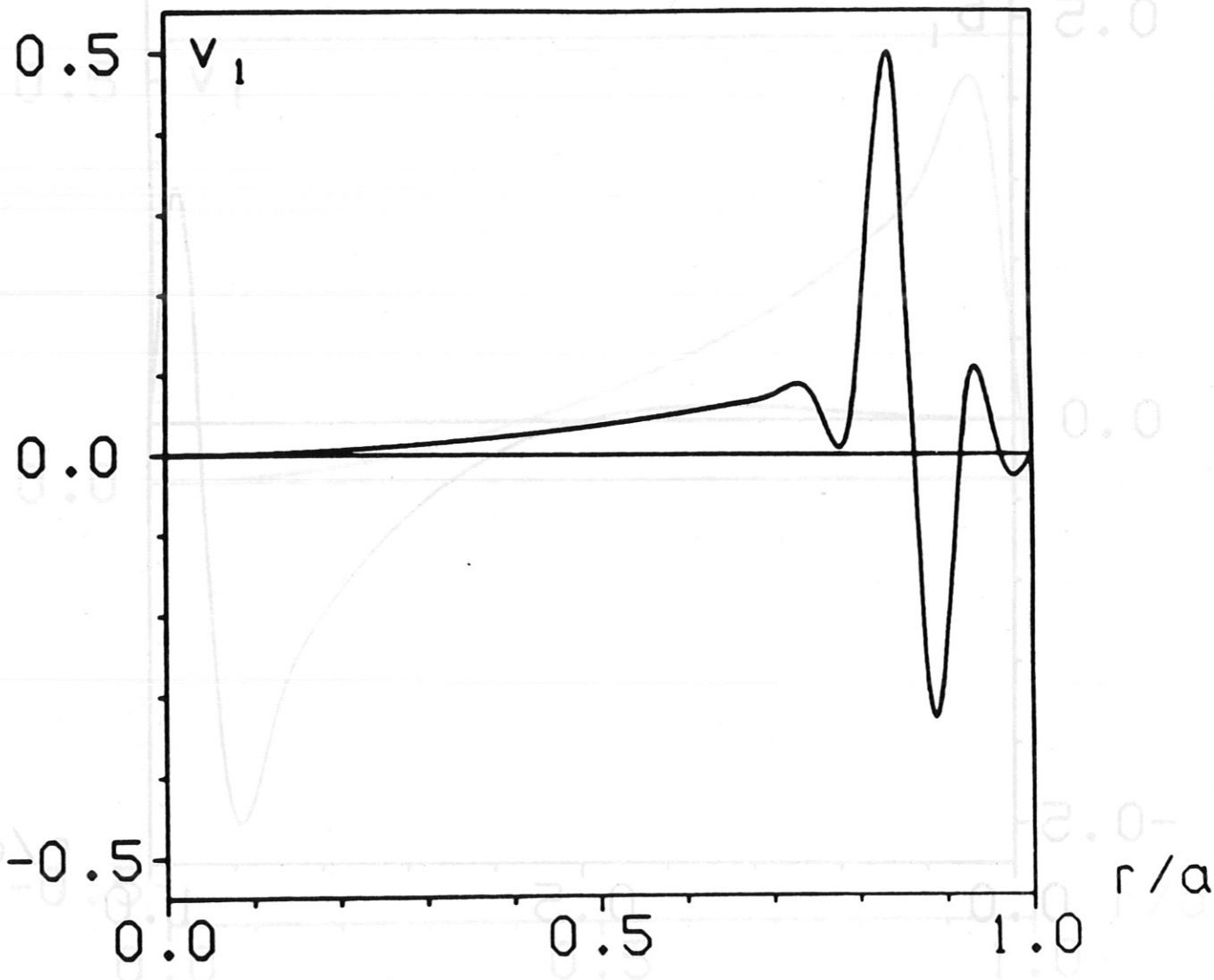

Fig 6b

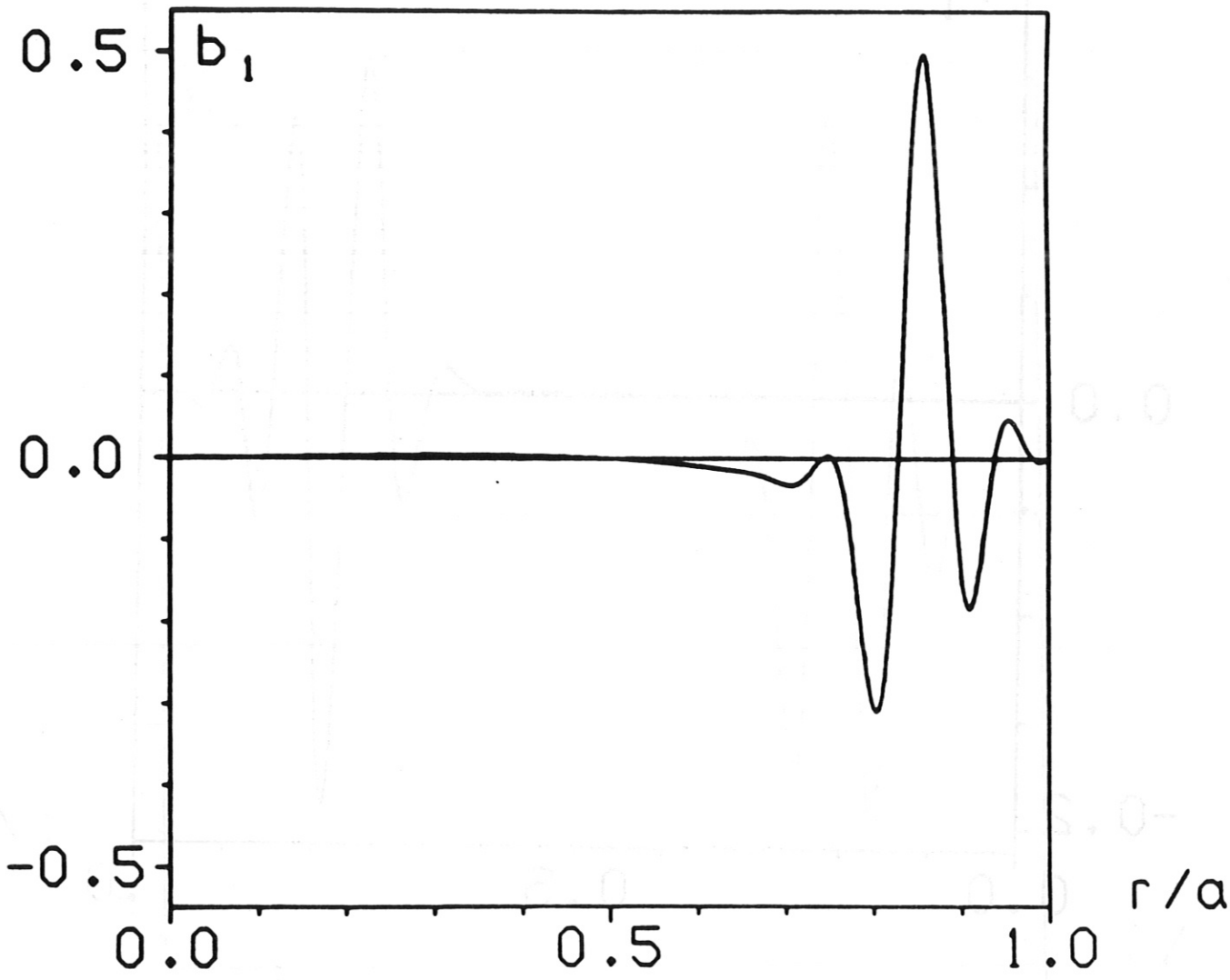

Fig 6b

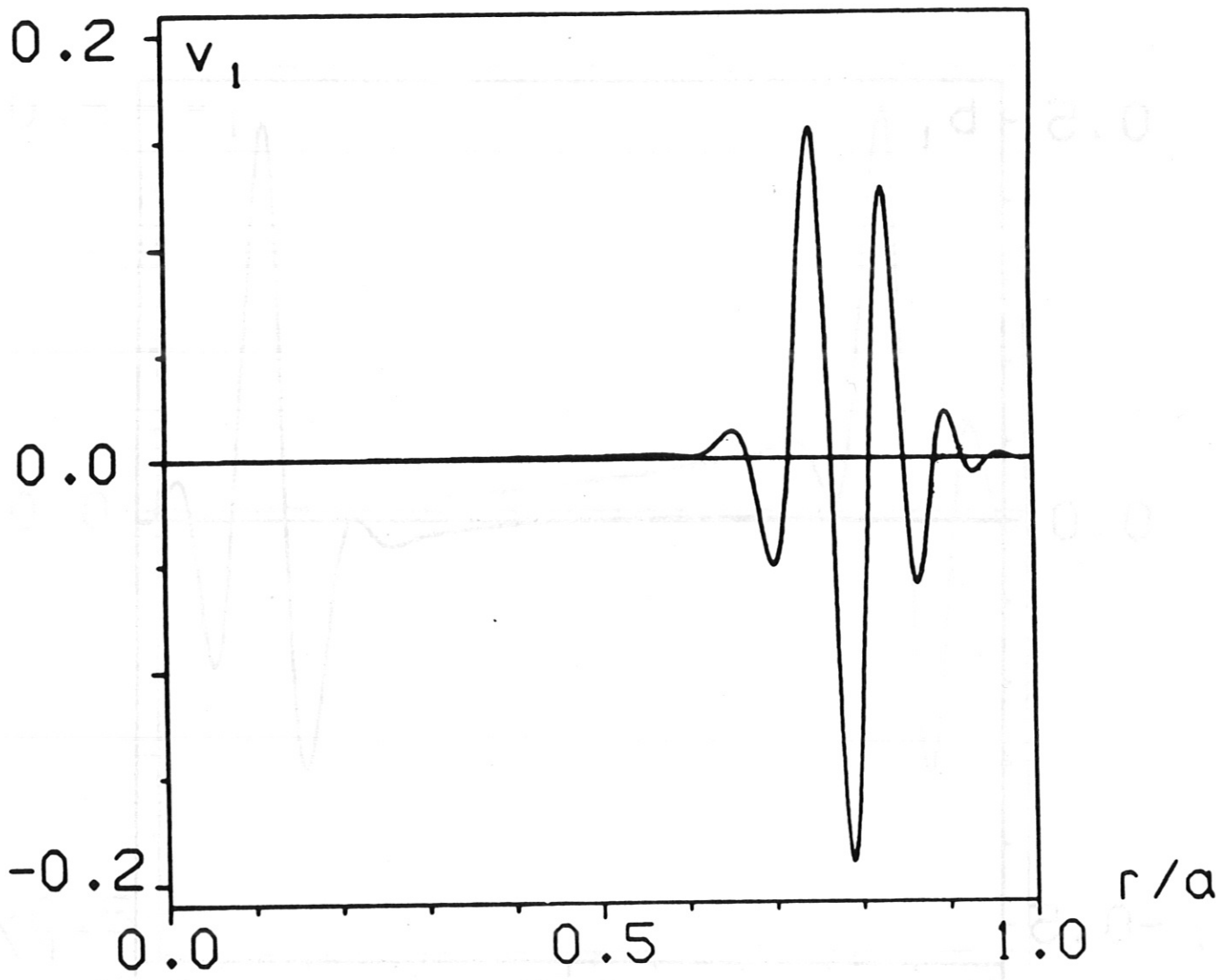

Fig 6c

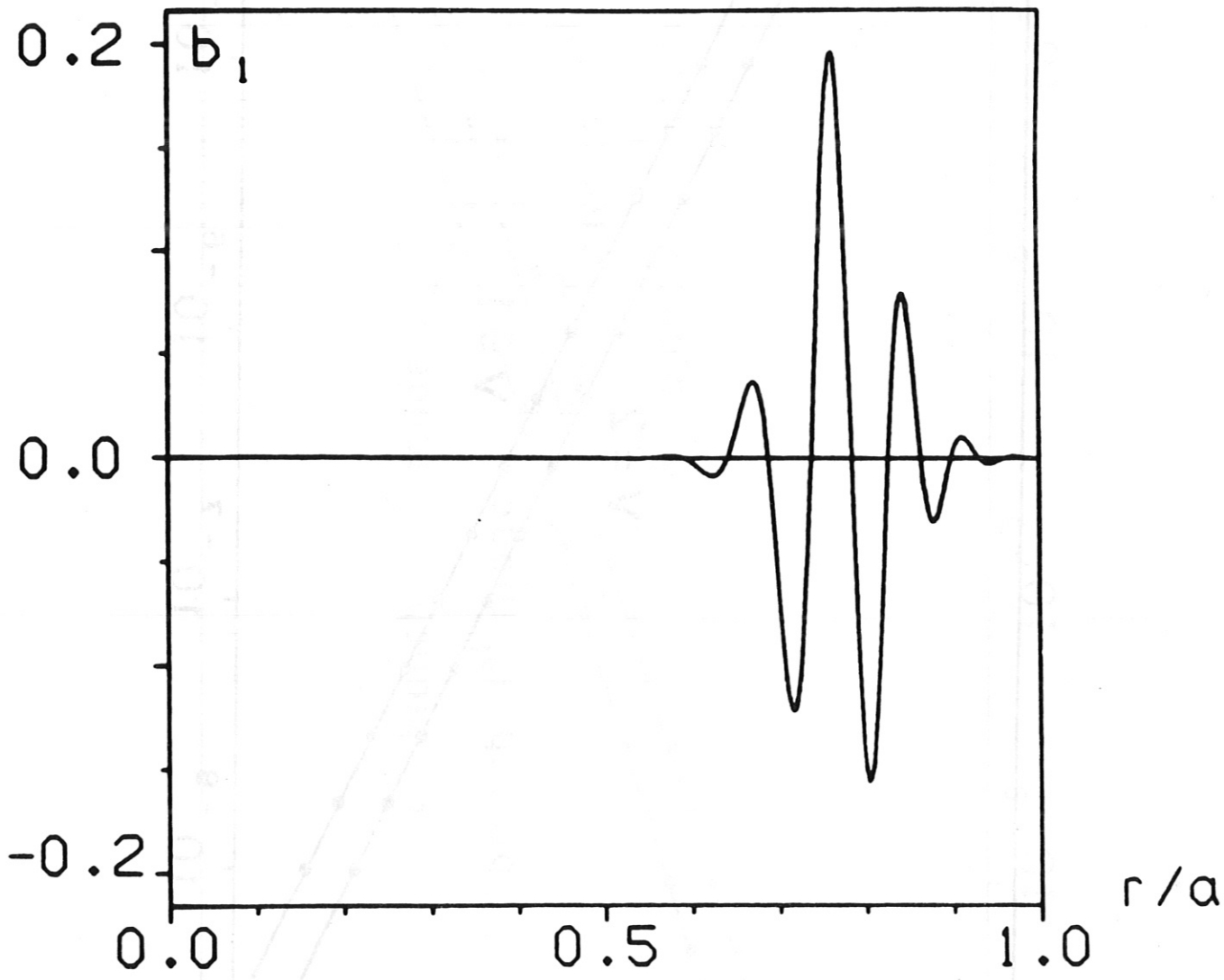

Fig 6c

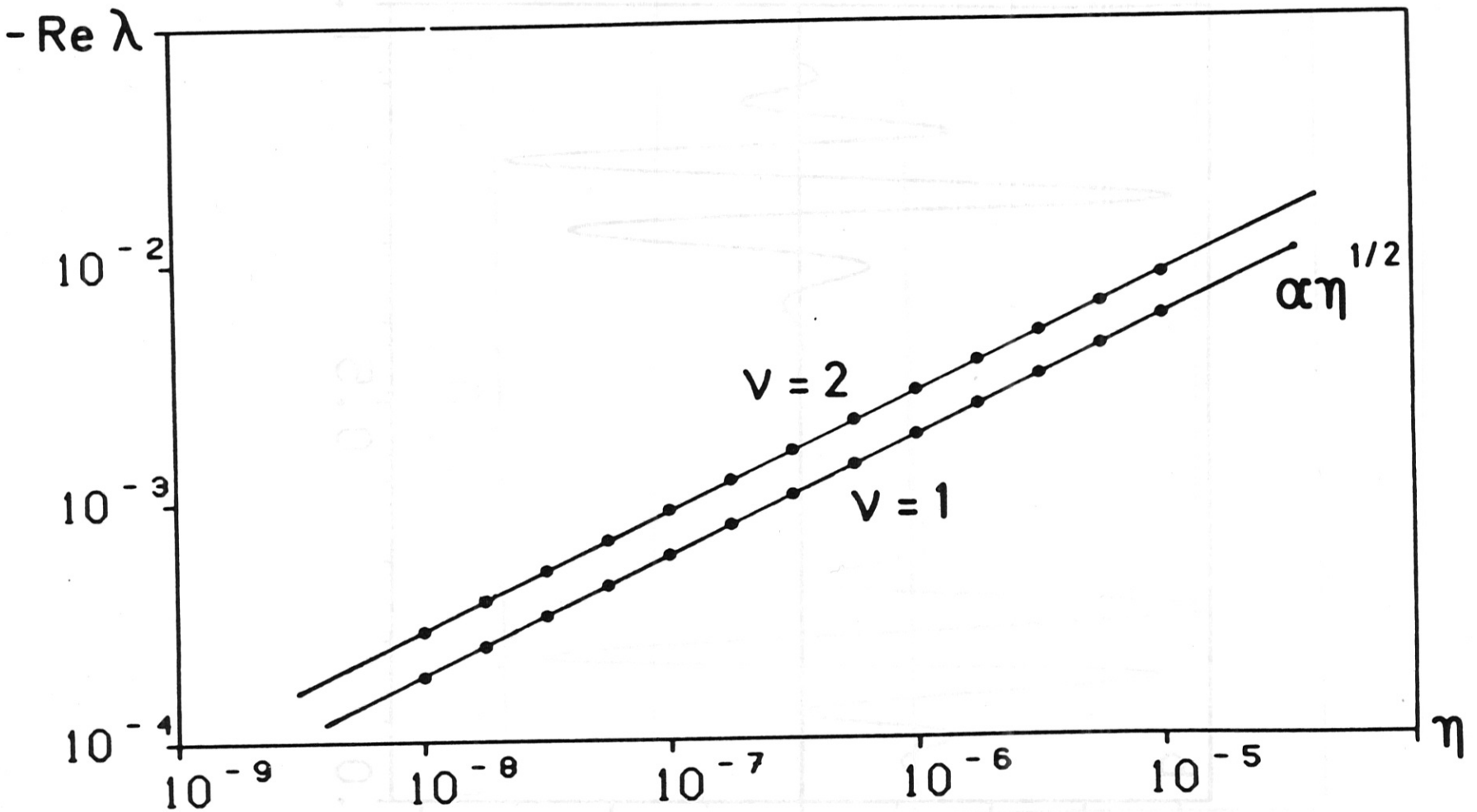

Fig 7

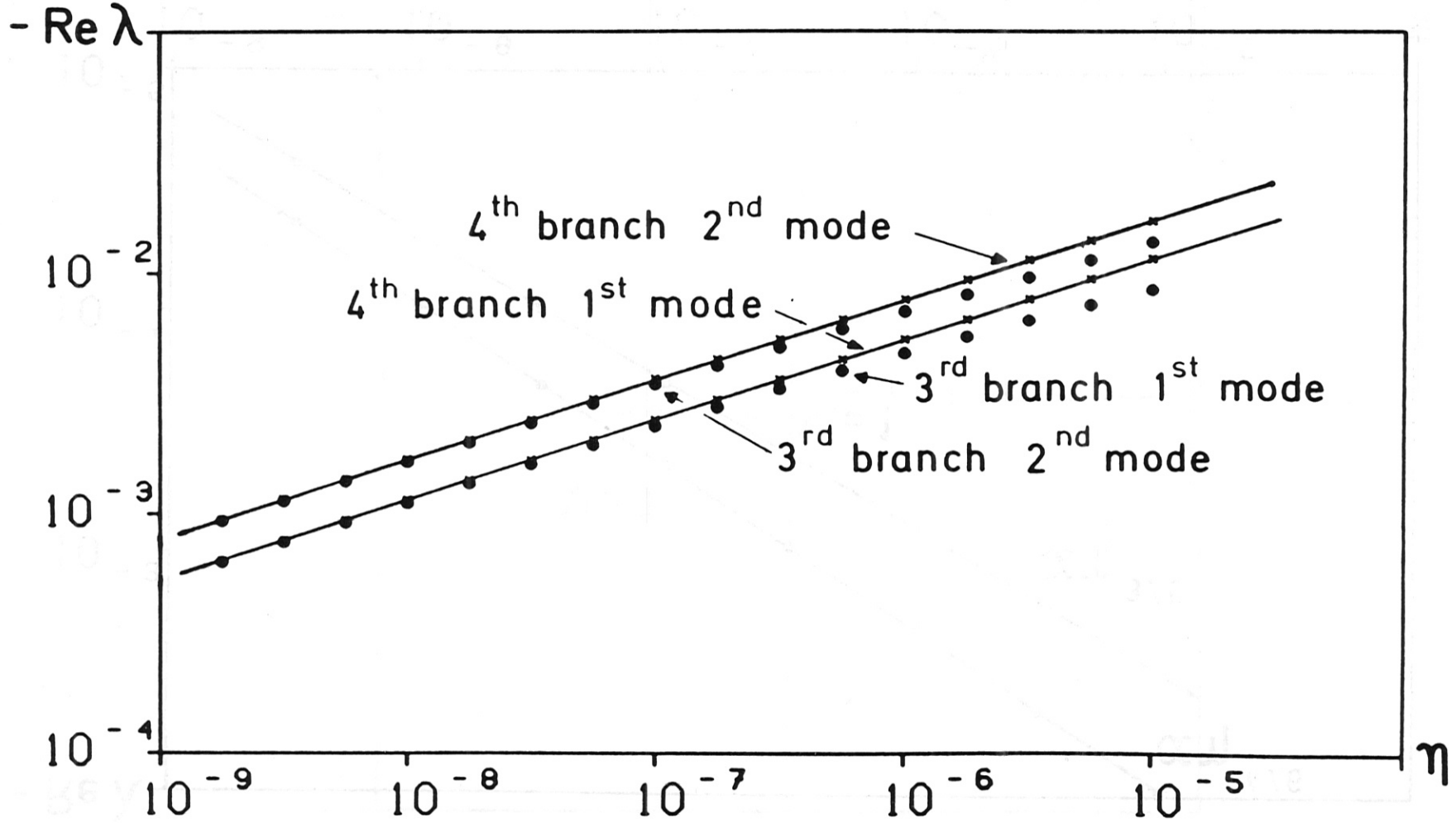
- Re λ
10 - 2
10 - 3
10 - 4
10 - 9
10 - 8
10 - 7
10 - 6
10 - 5
η
4th branch 2nd mode
4th branch 1st mode
3rd branch 1st mode
3rd branch 2nd mode

Fig 8

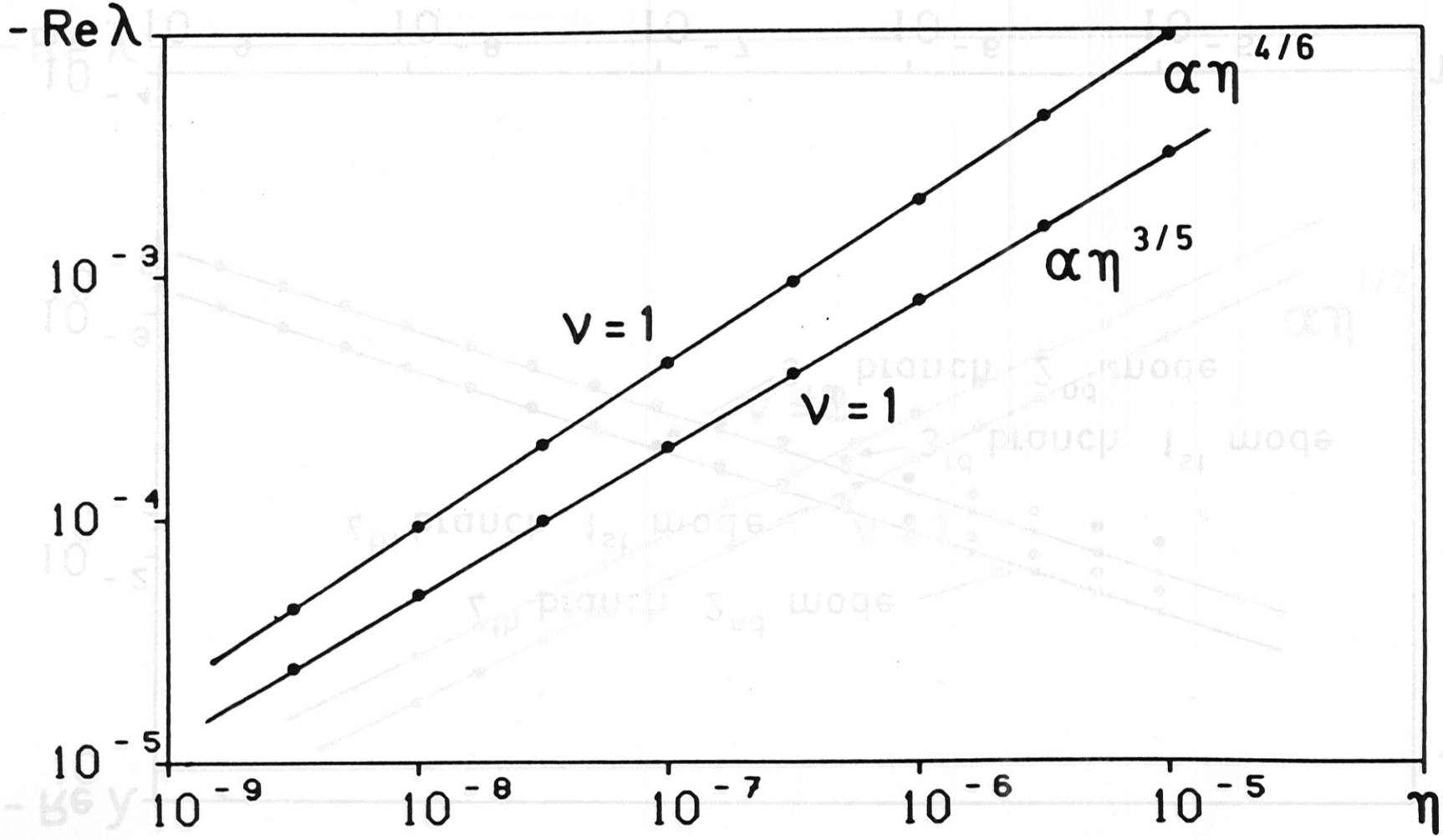

Fig 9

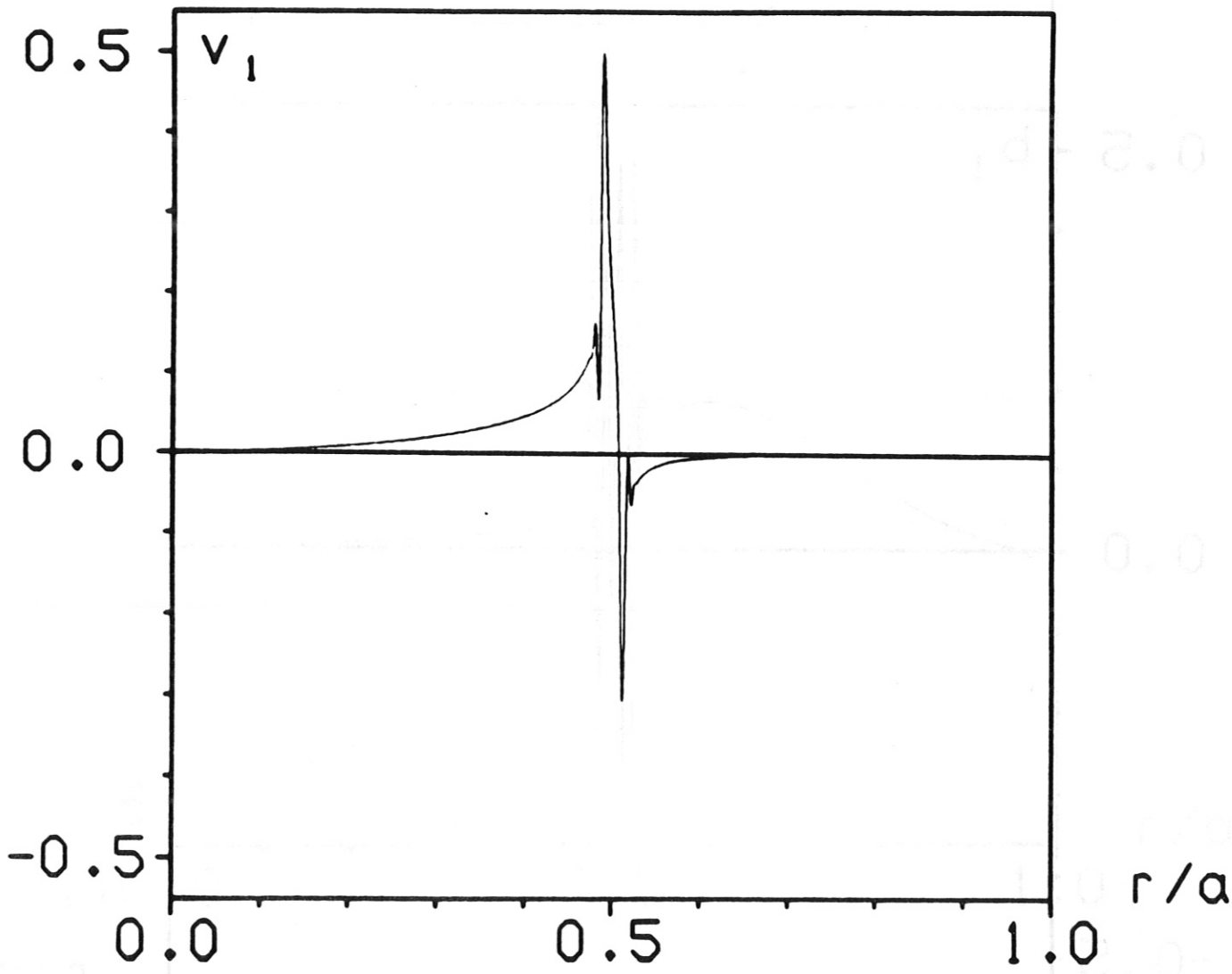

Fig 10a

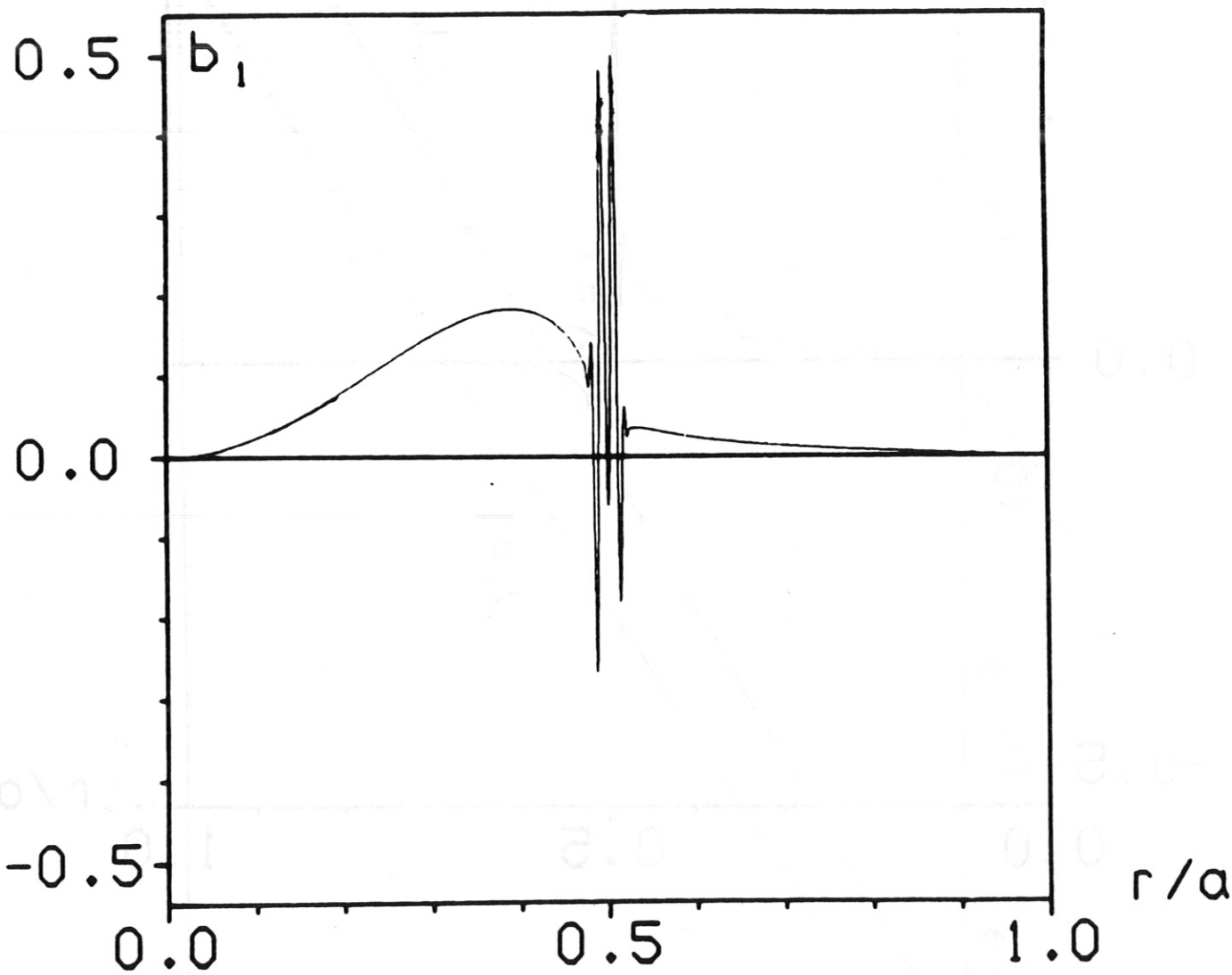

Fig 10a

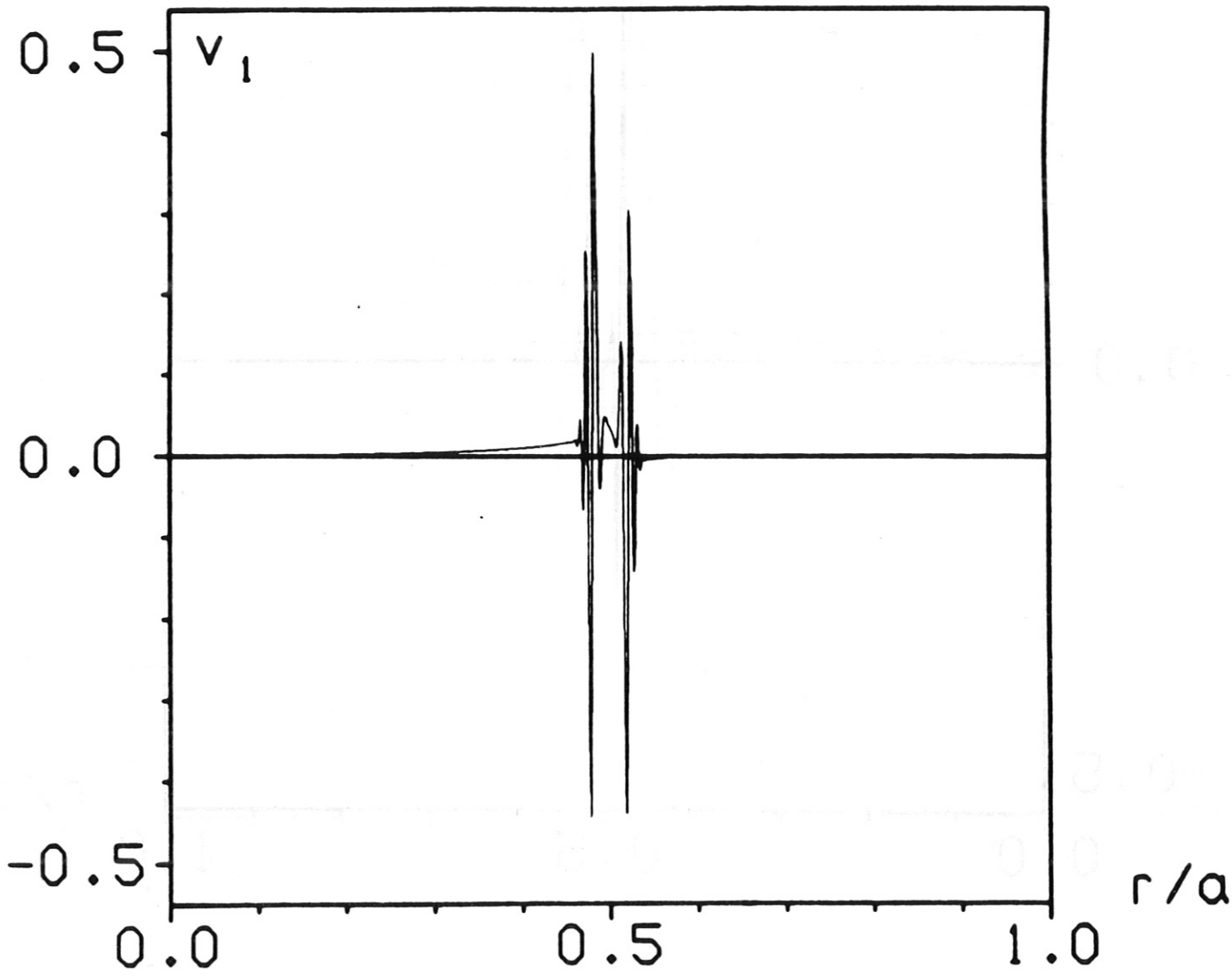

Fig 10b

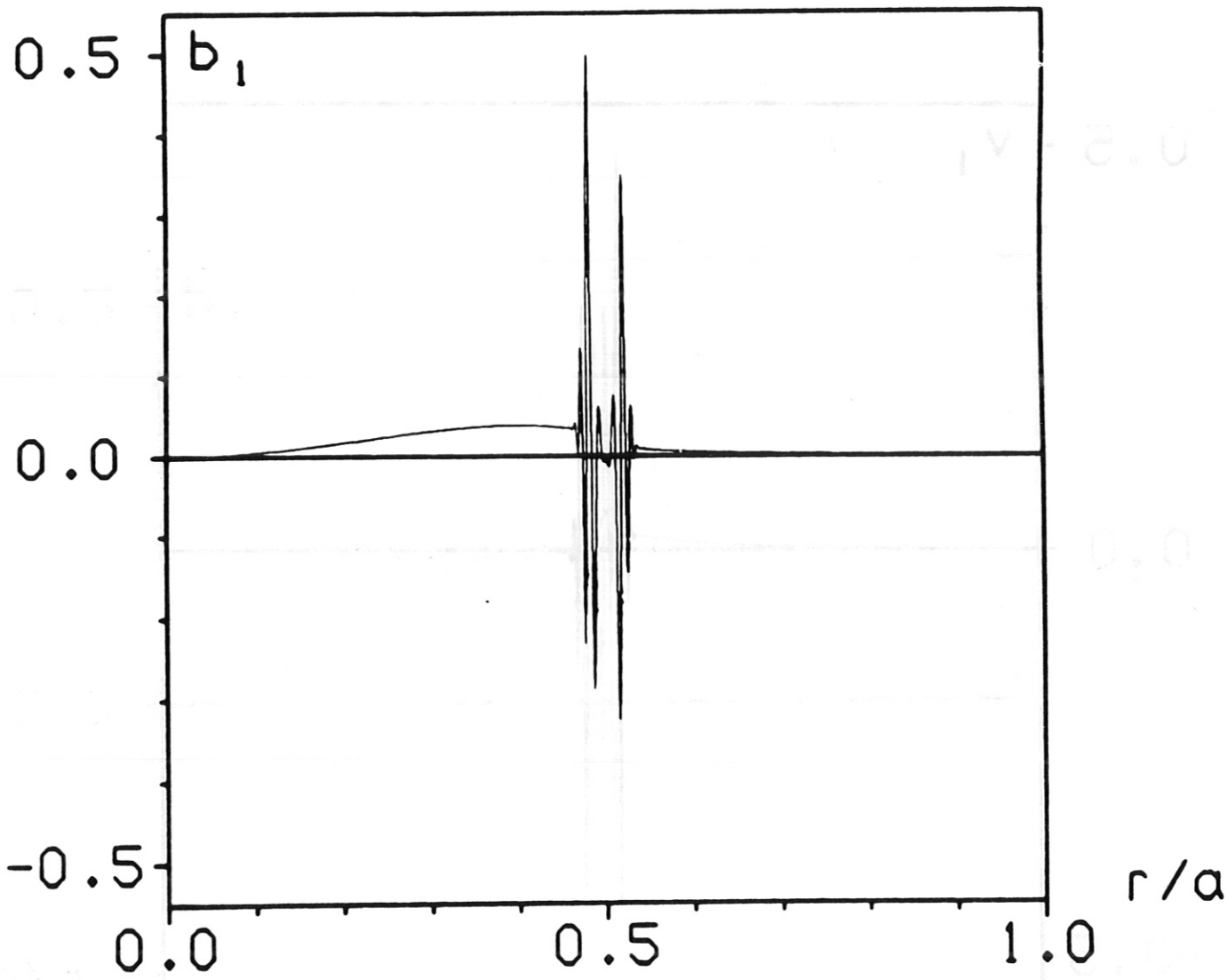

Fig 10b

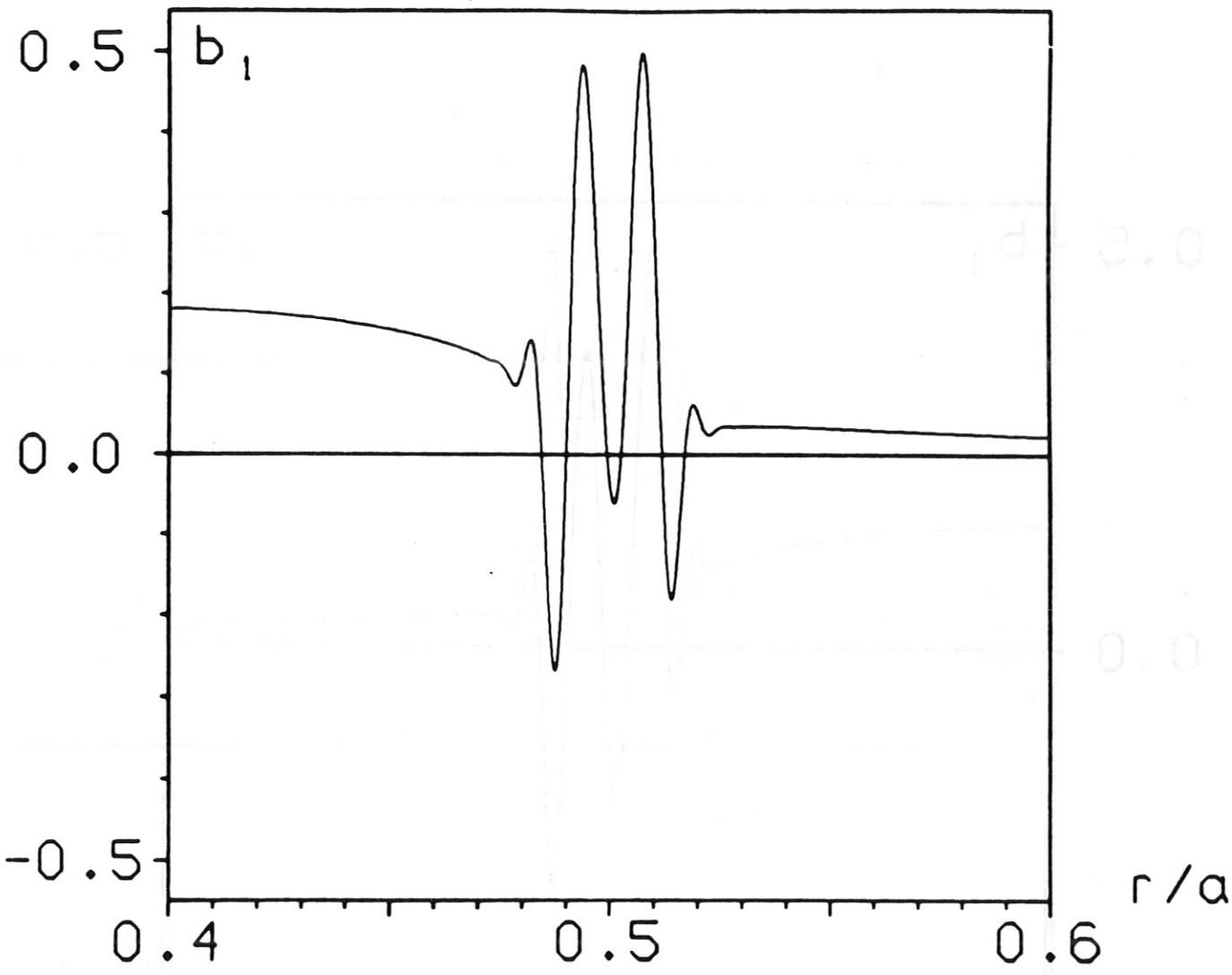

Fig 11a

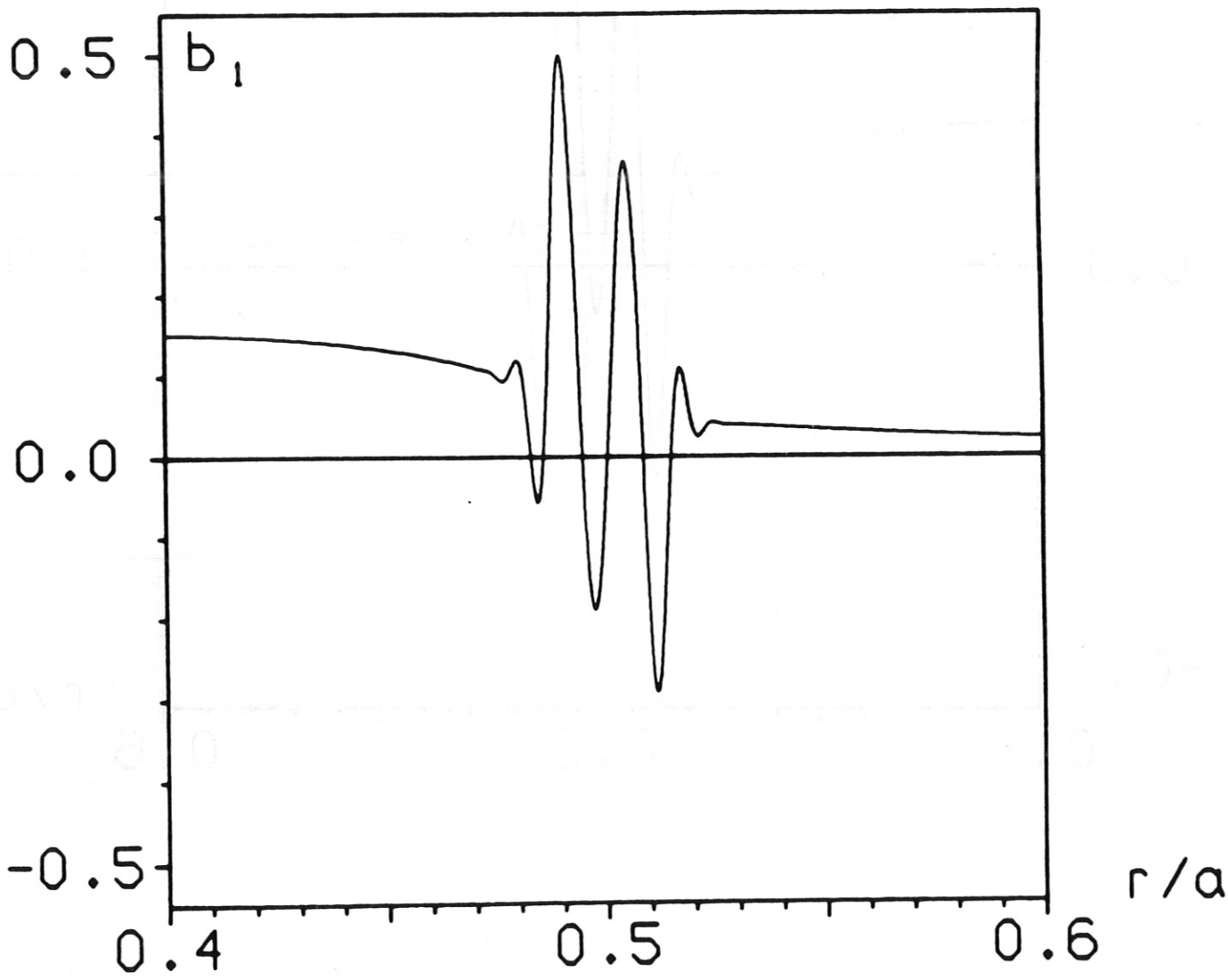

Fig 11b

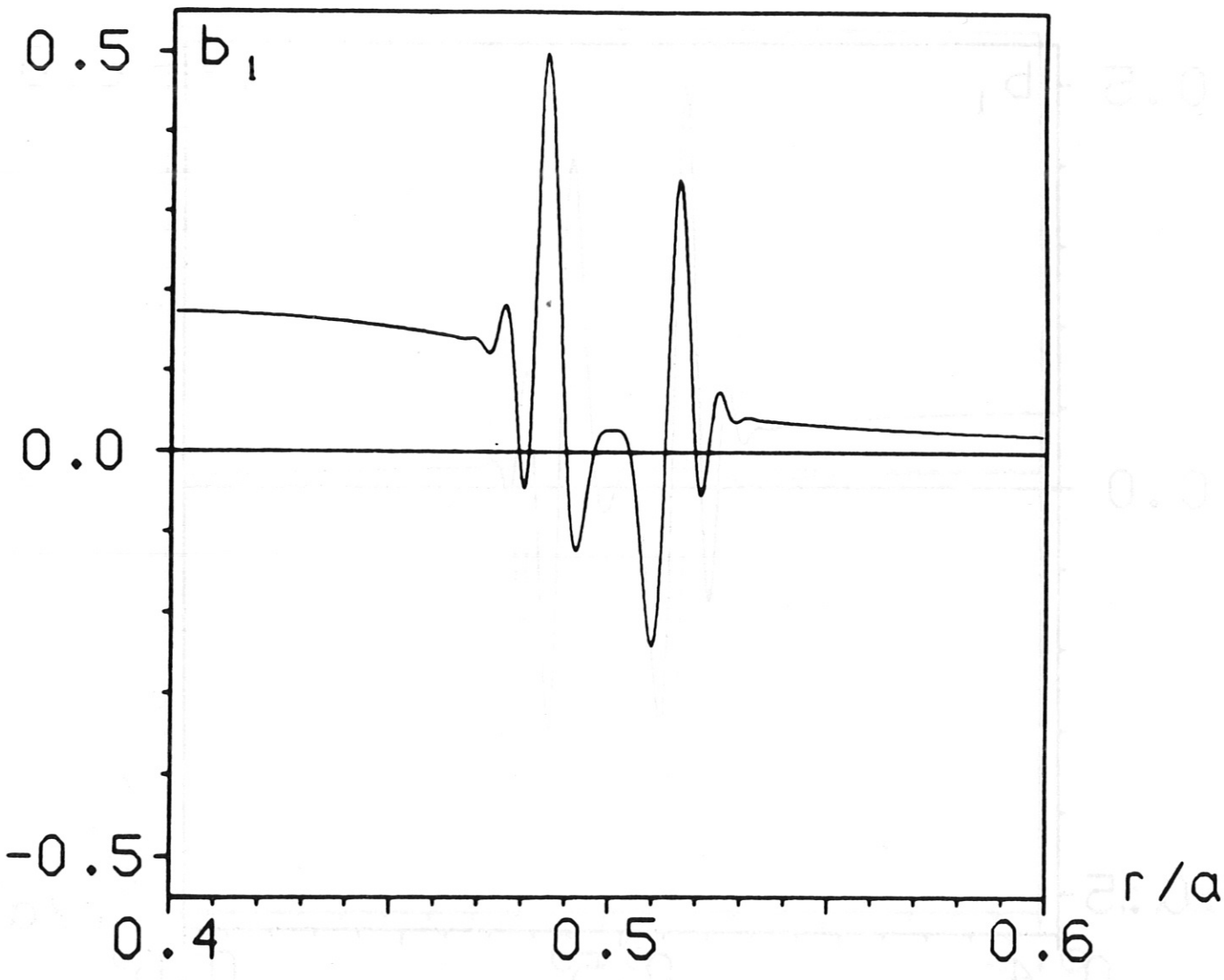

Fig 11c

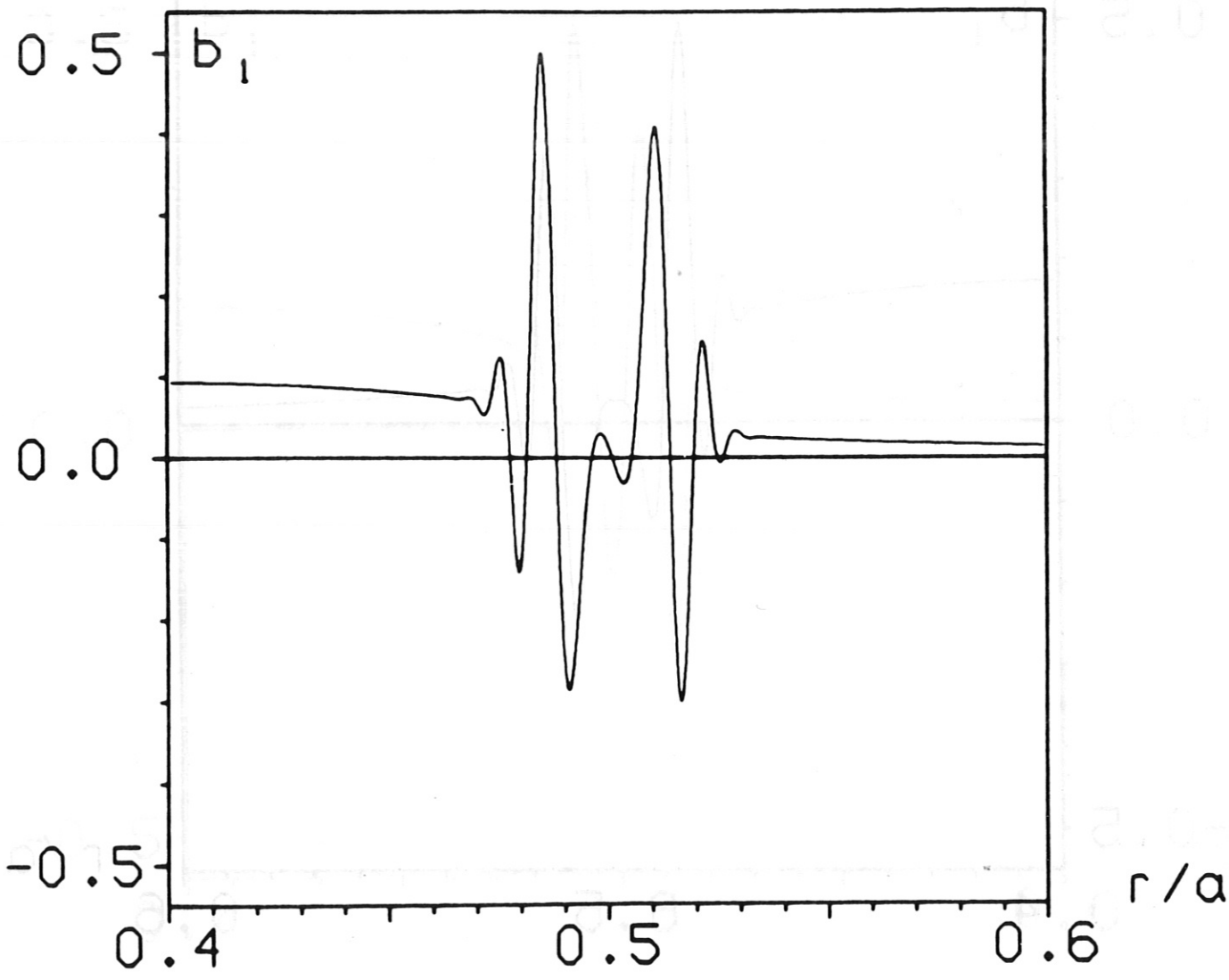

Fig 11d

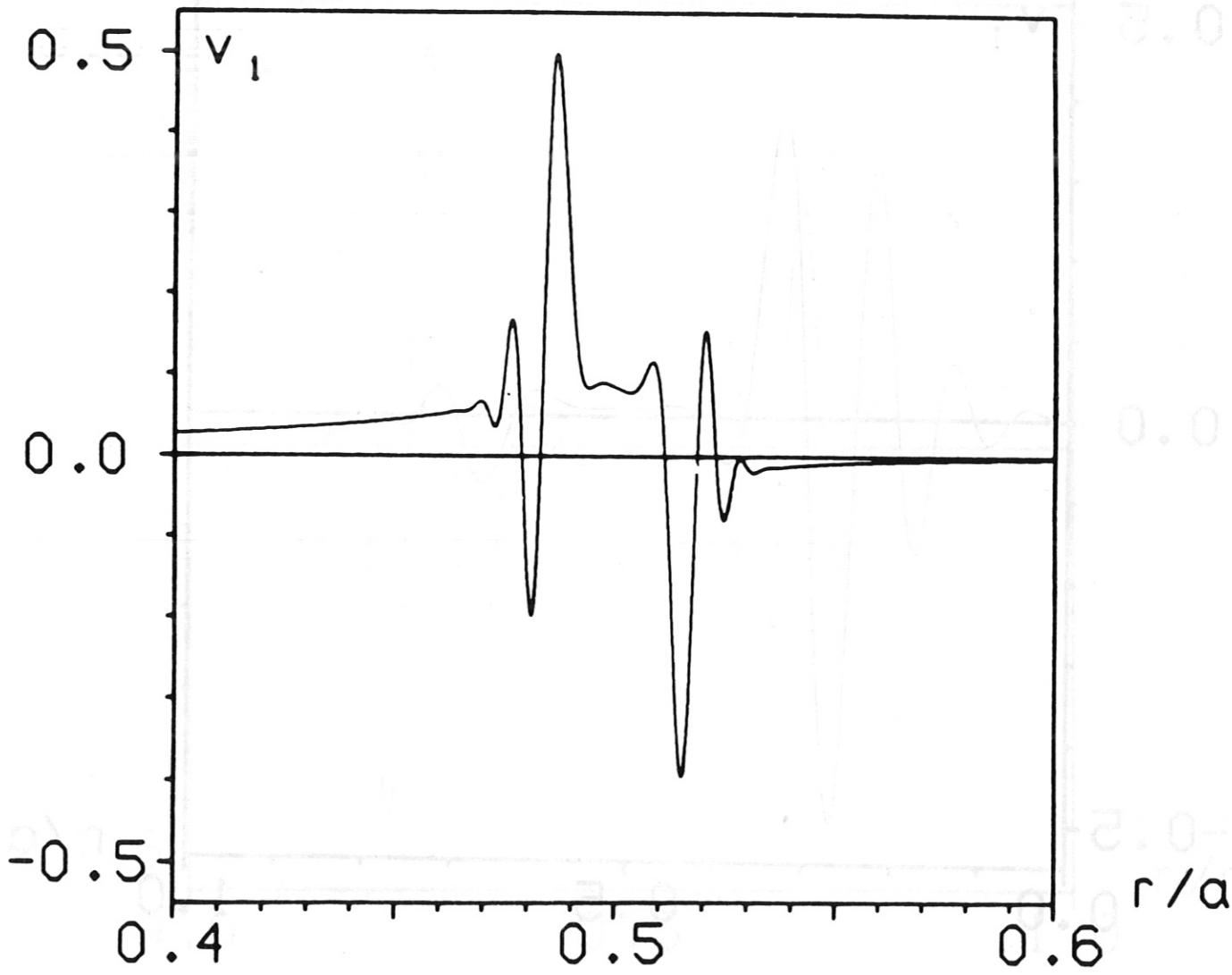

Fig 12

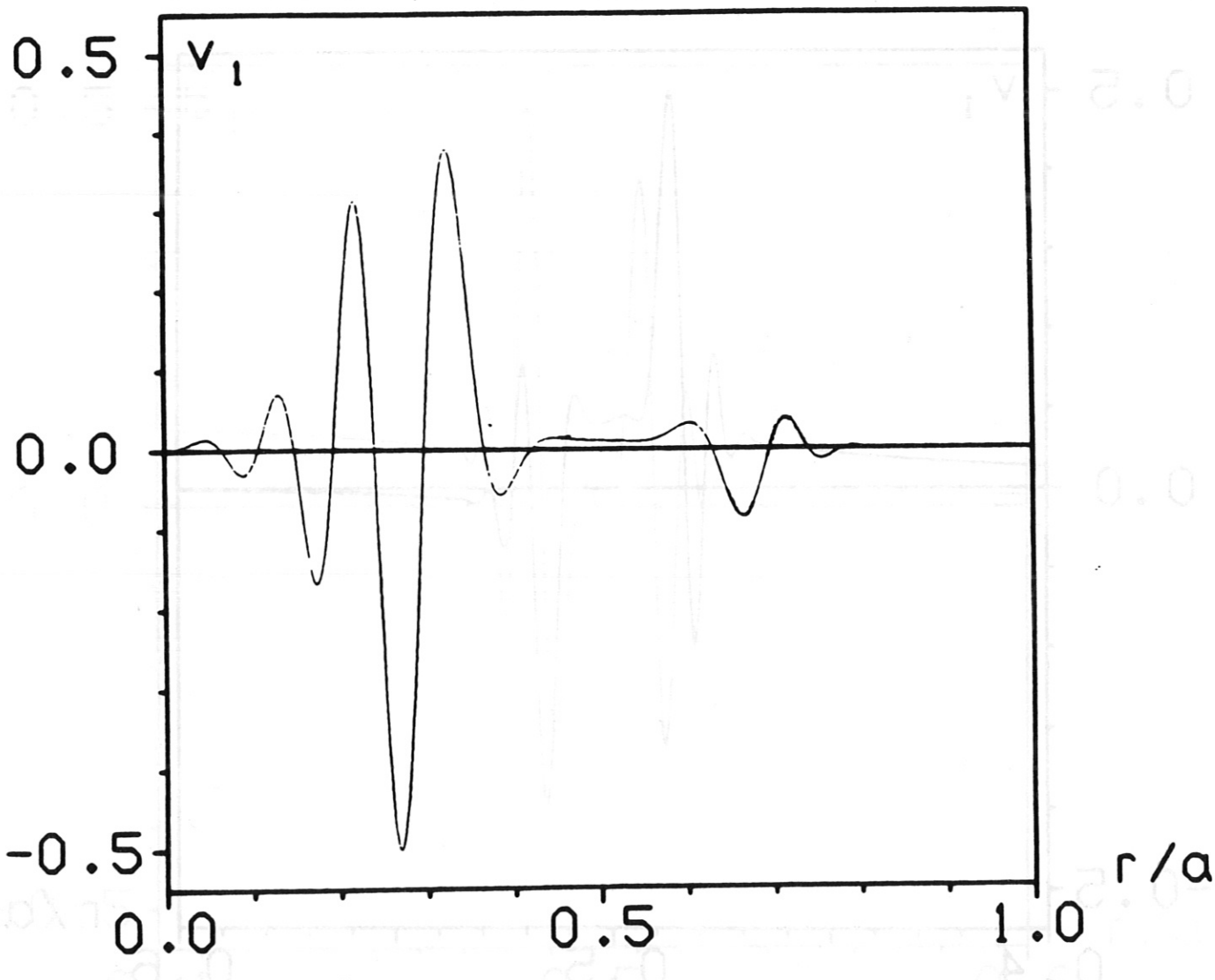

Fig 13a

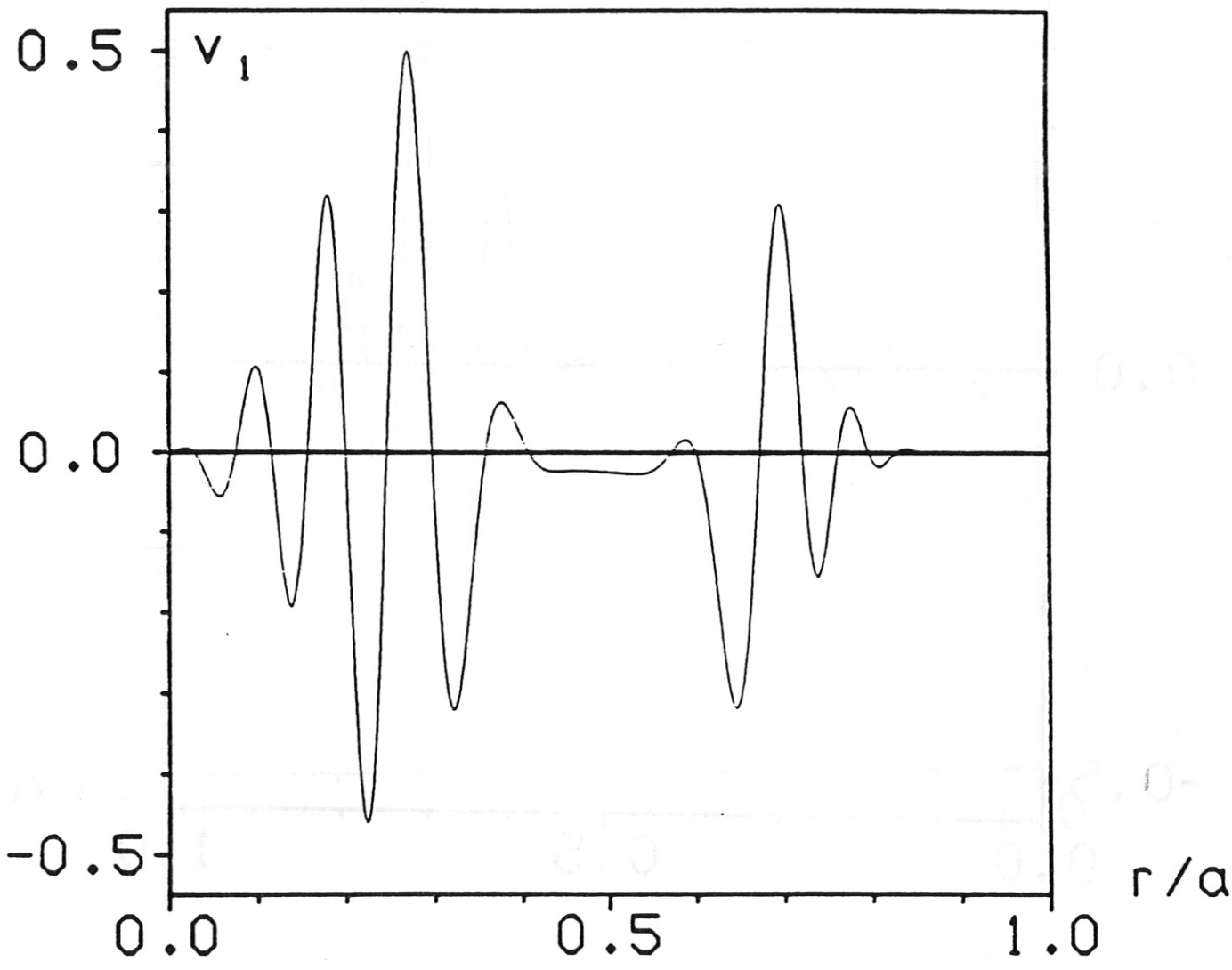

Fig 13b

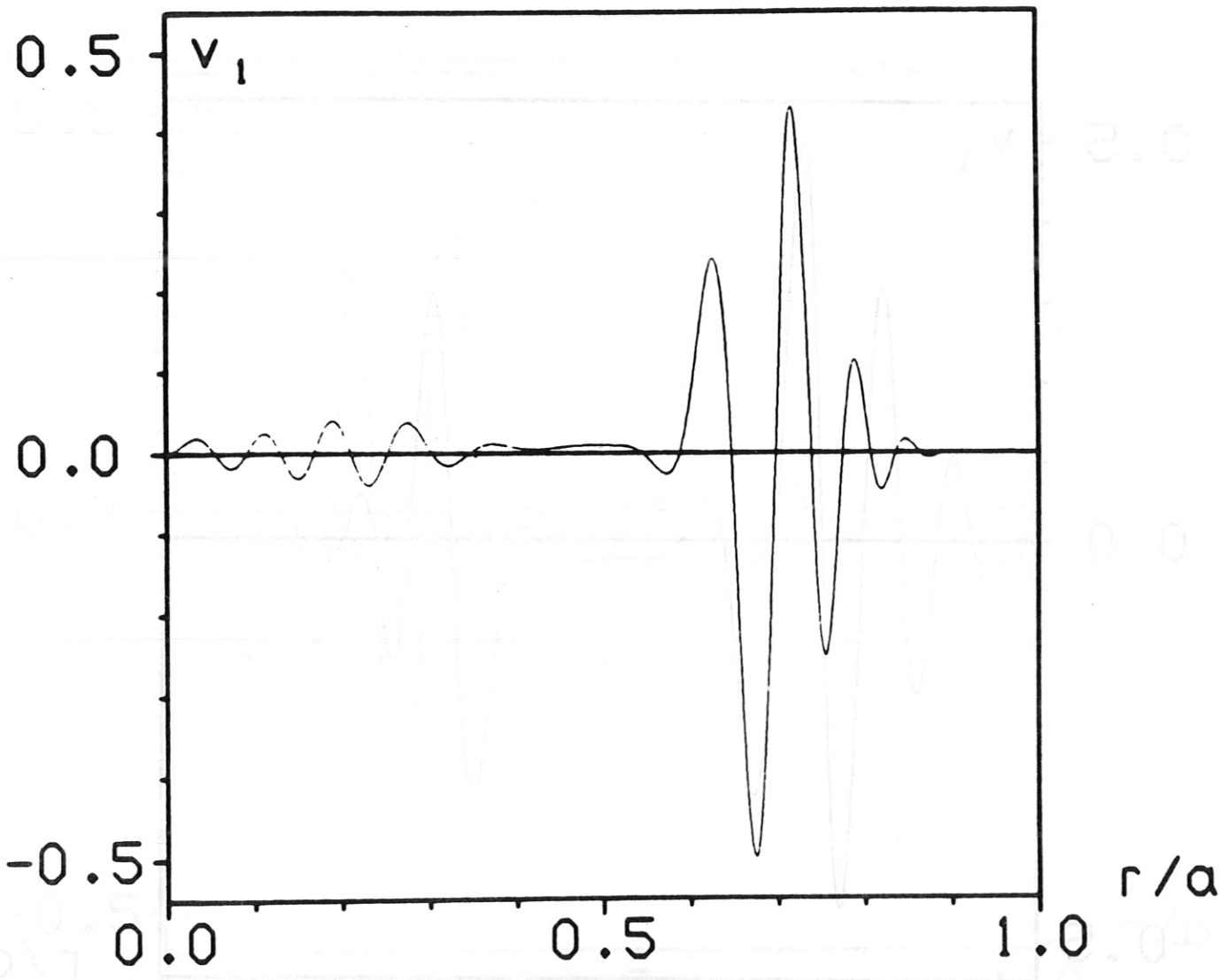

Fig 13c

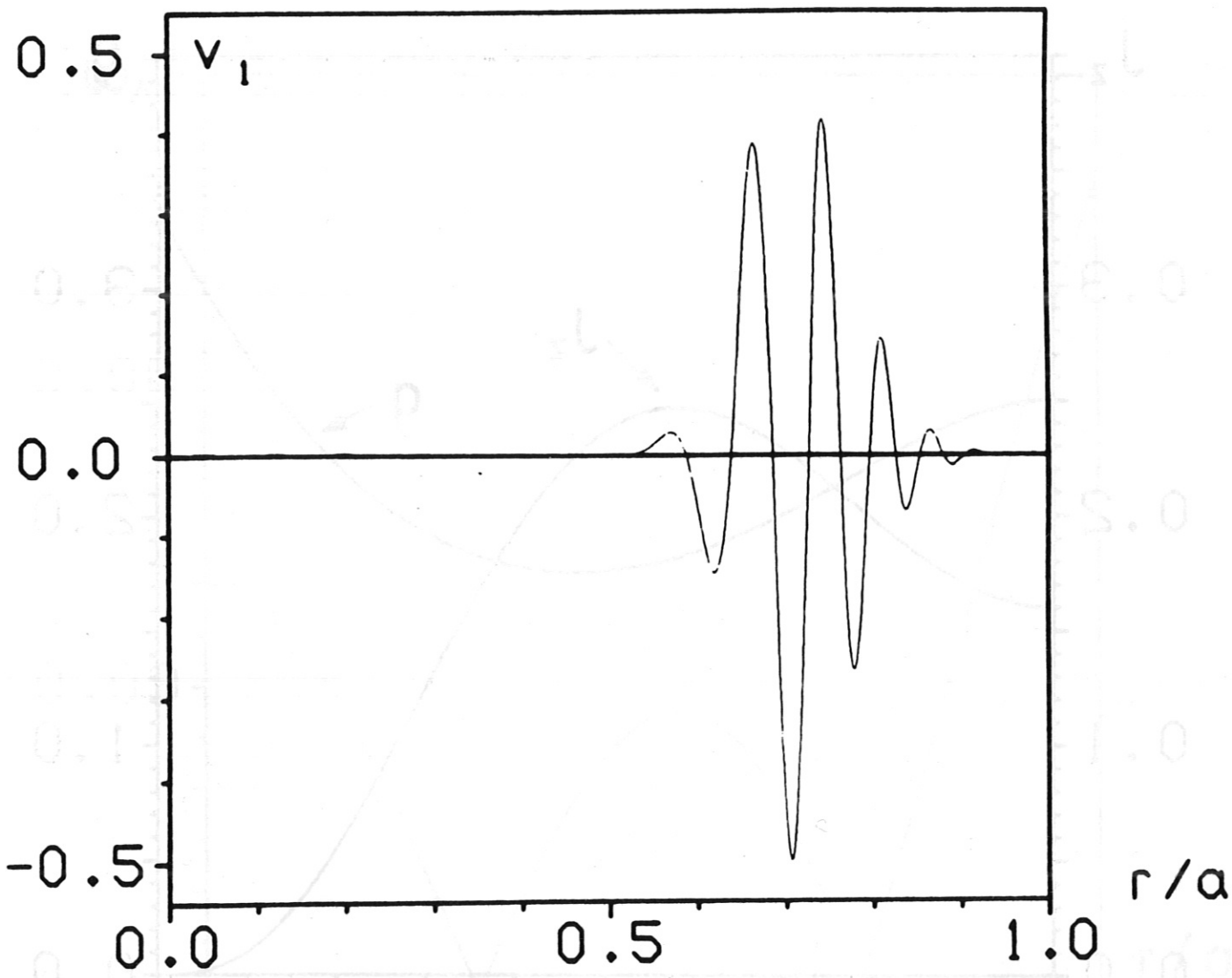

Fig 13d

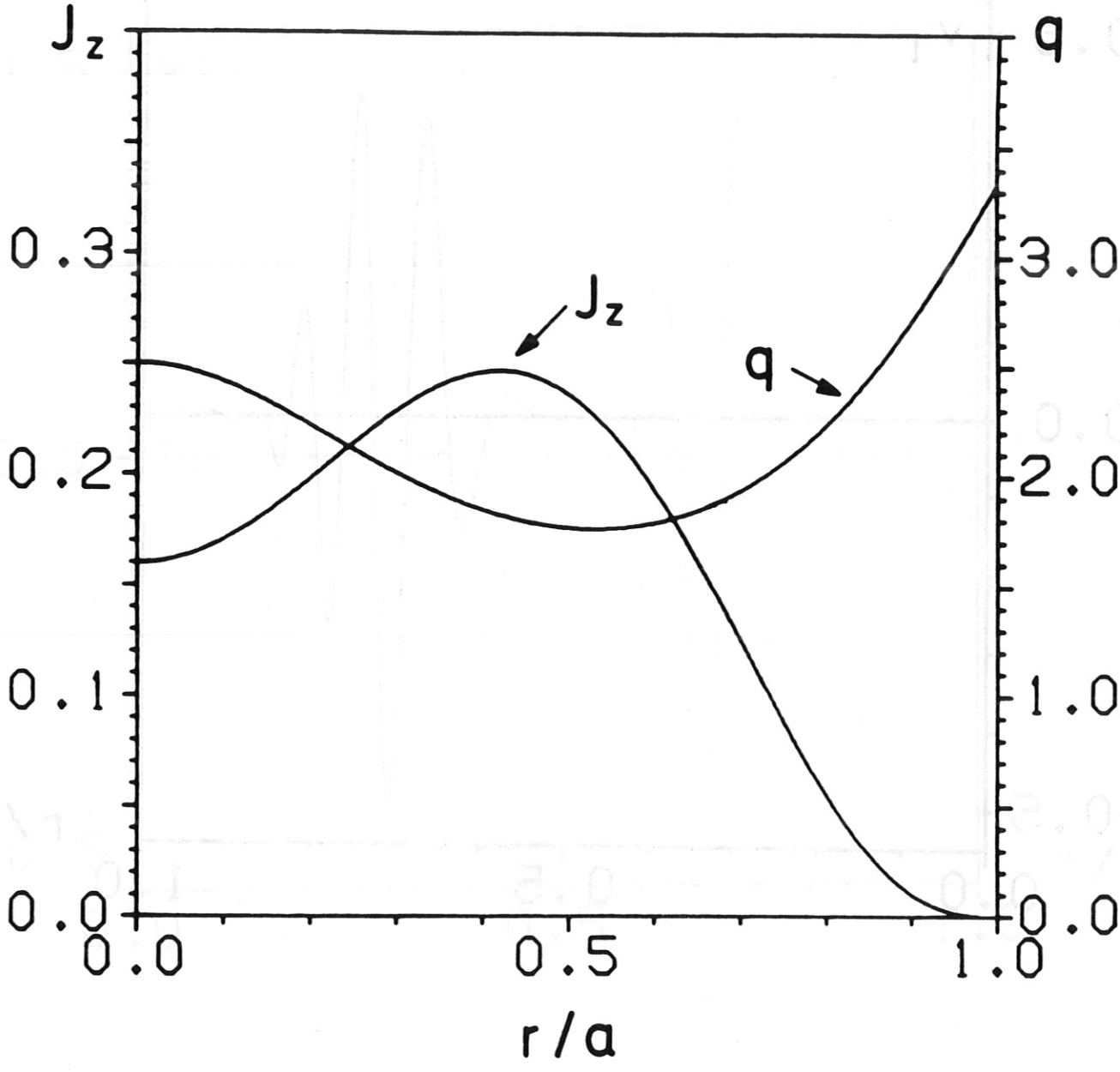

Fig 14

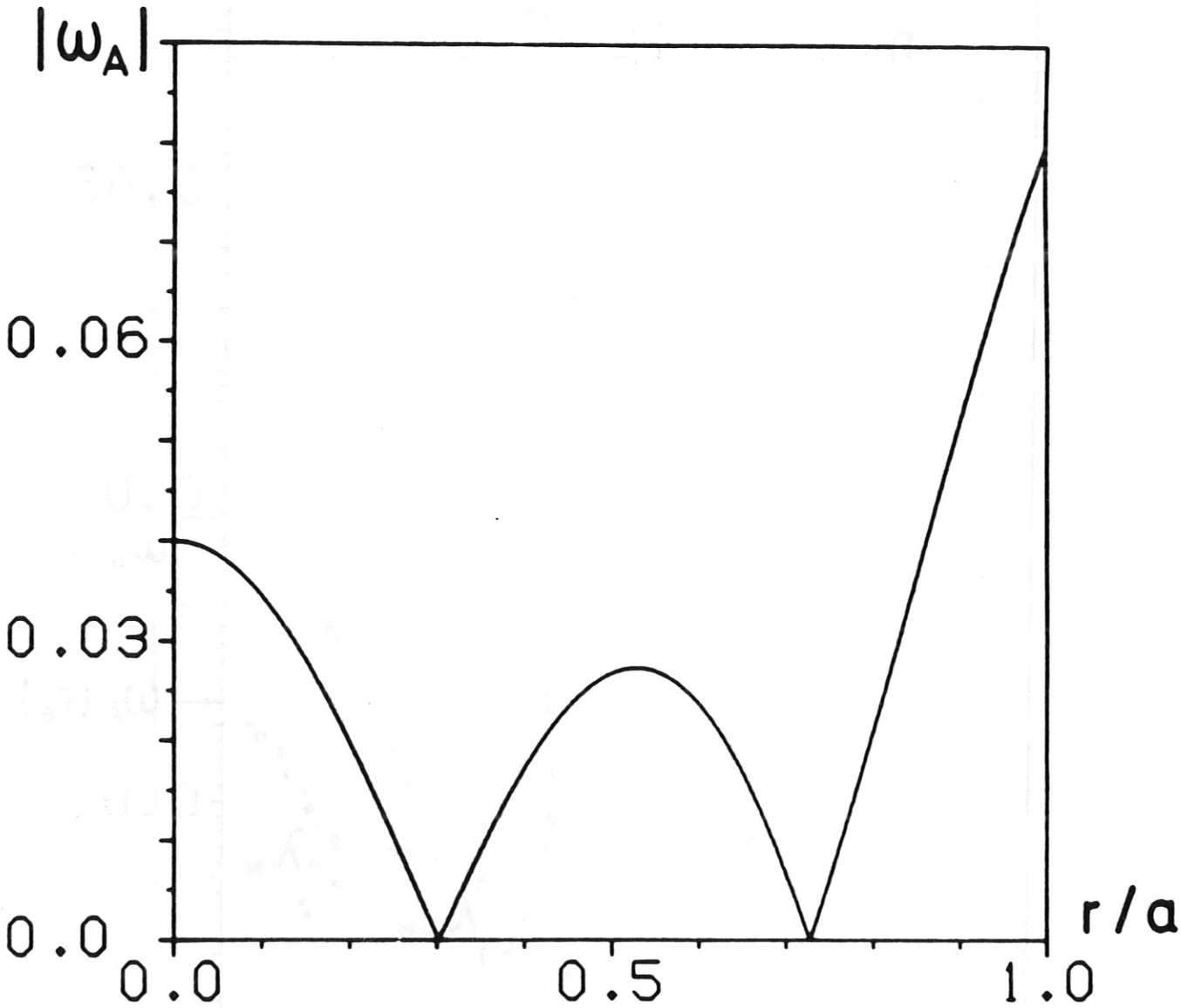

Fig 15

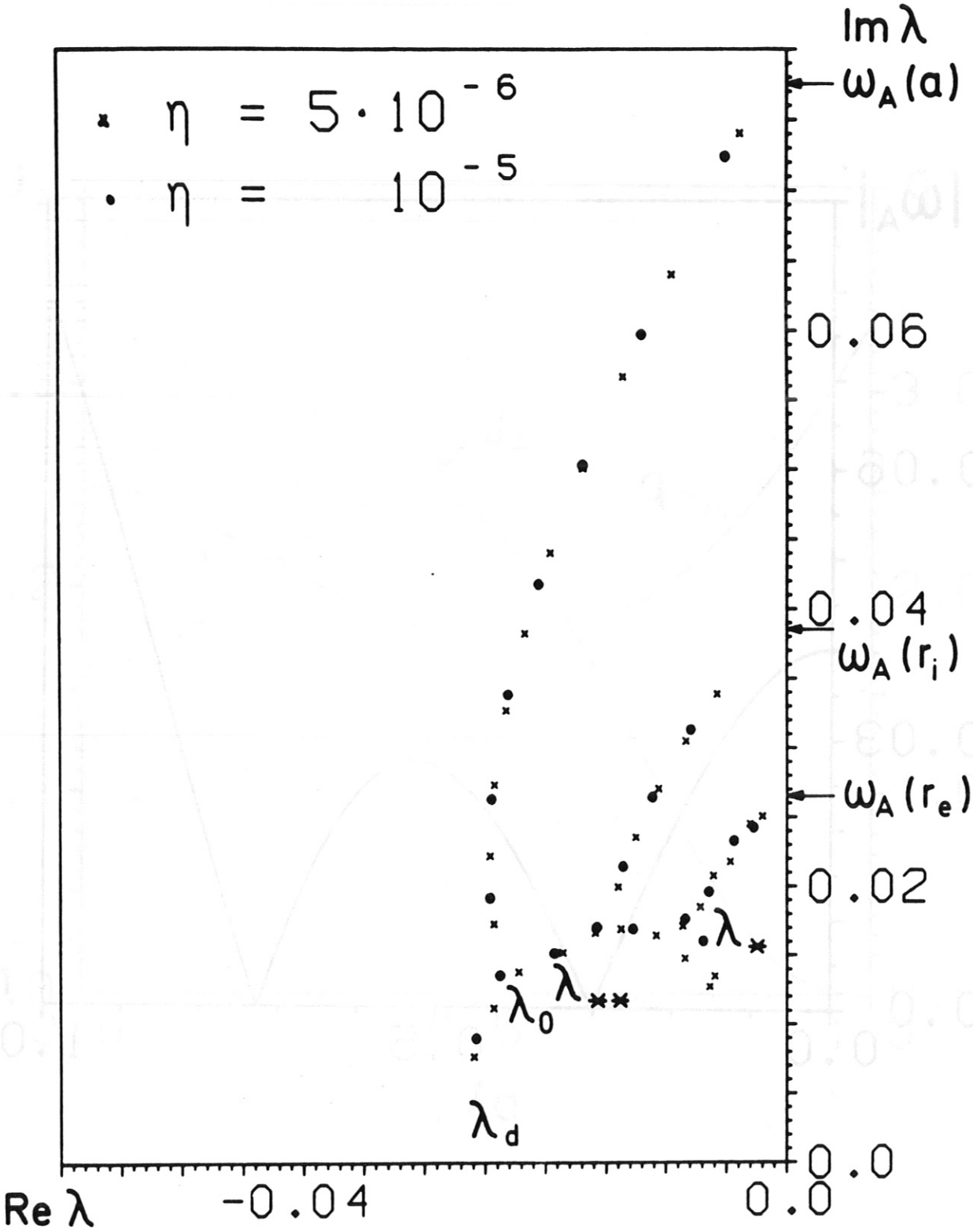

Fig 16

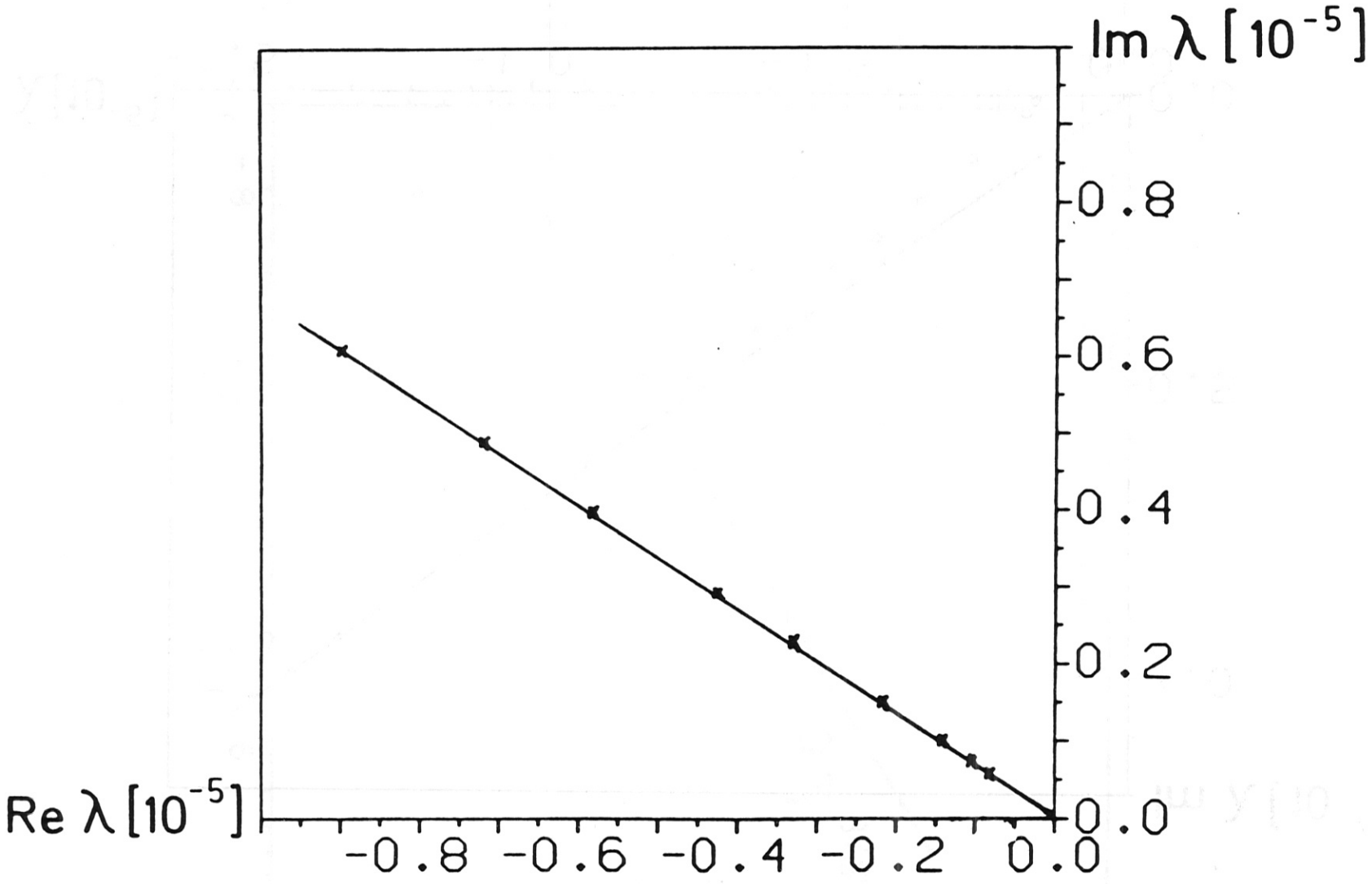

Fig 17

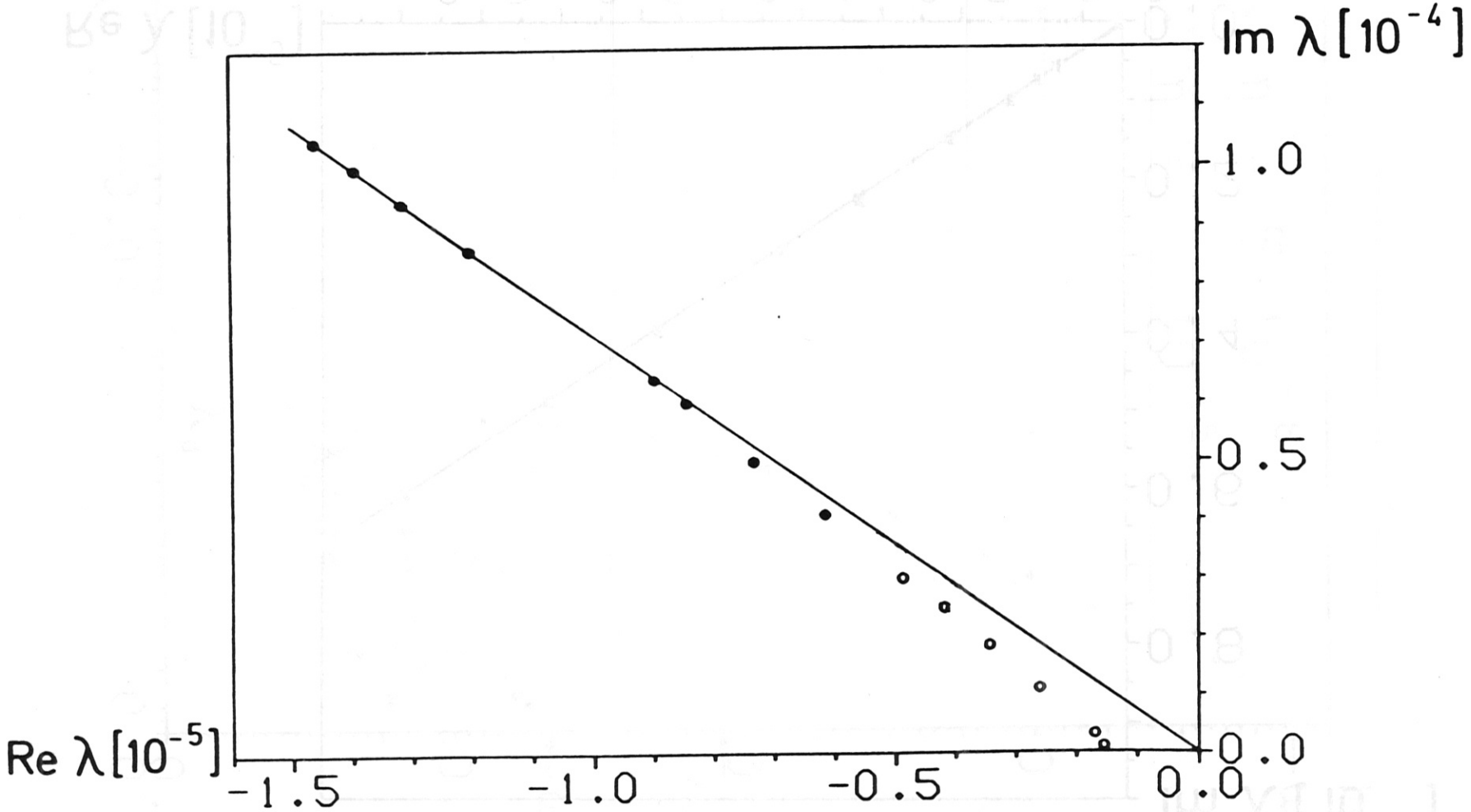

Fig 18a

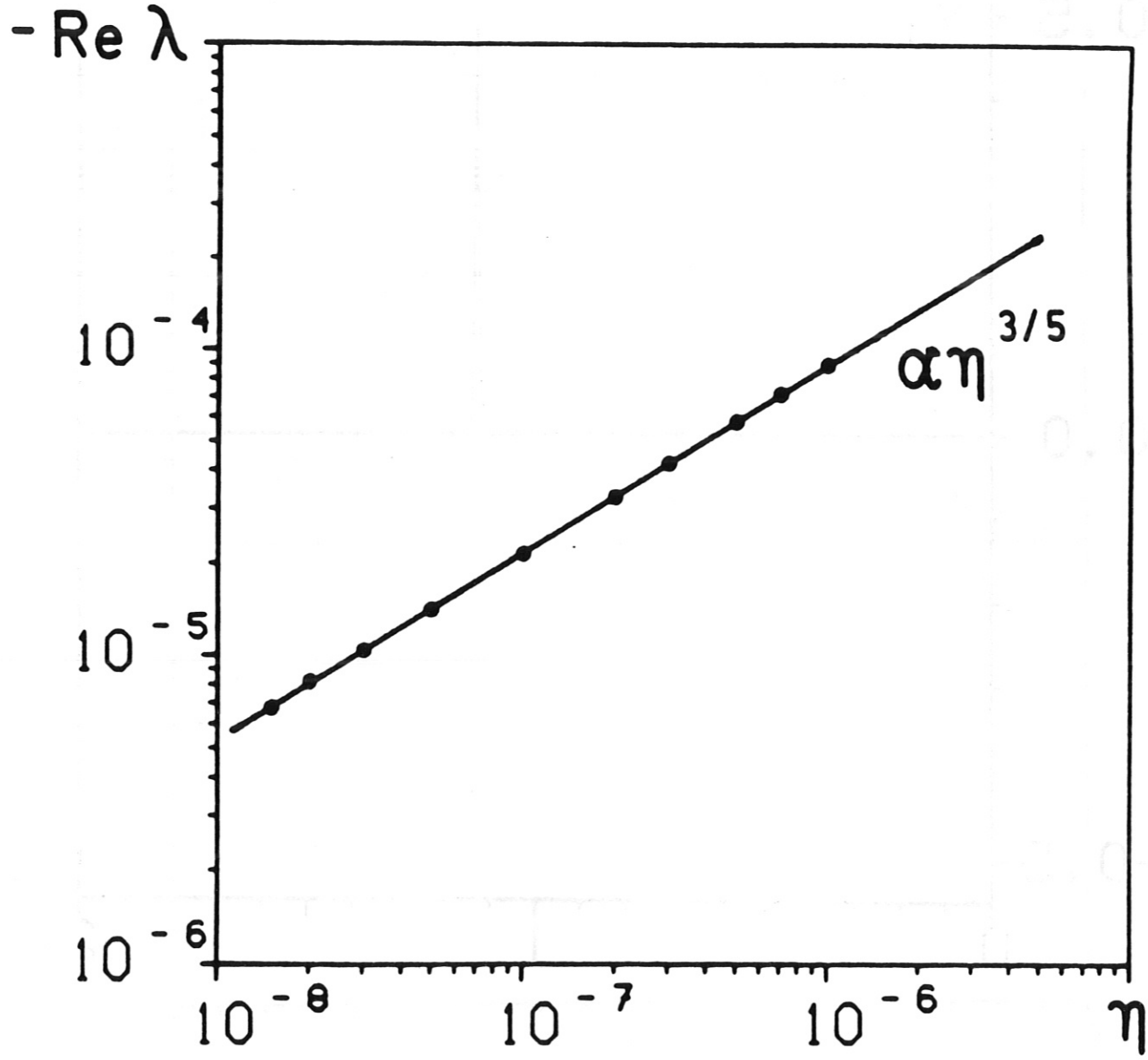

Fig 18b

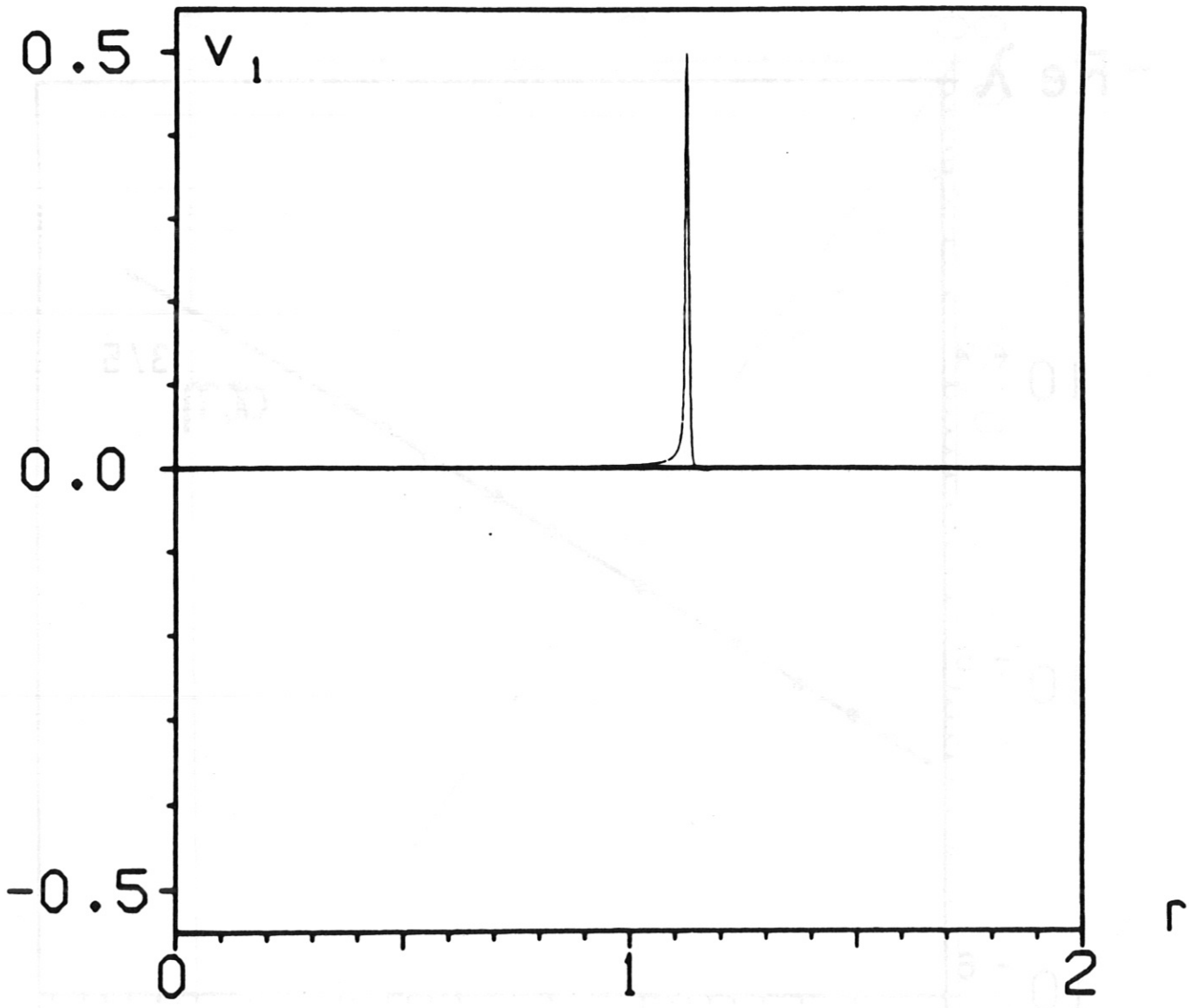

Fig 19a

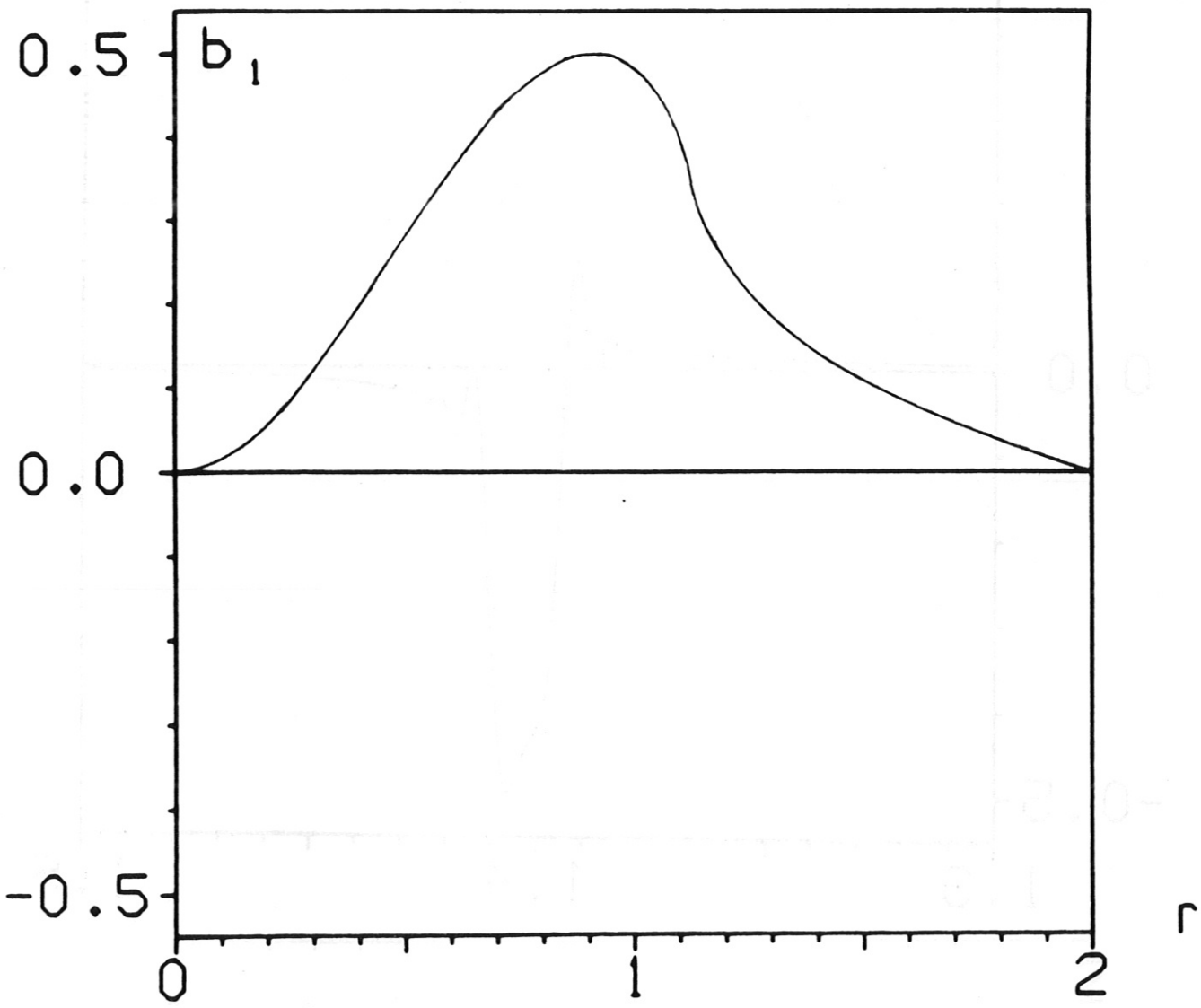

Fig 19a

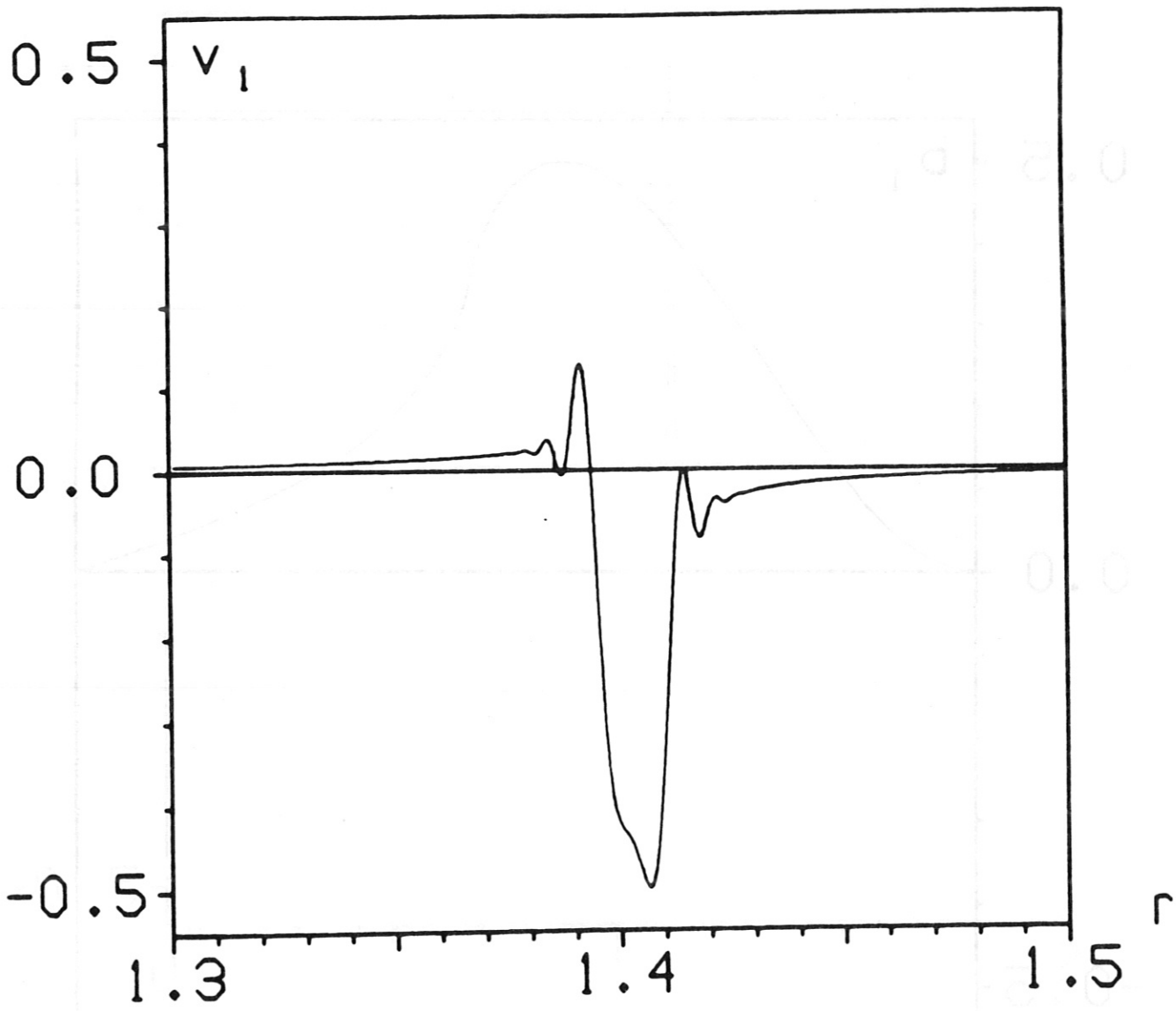

Fig 19b

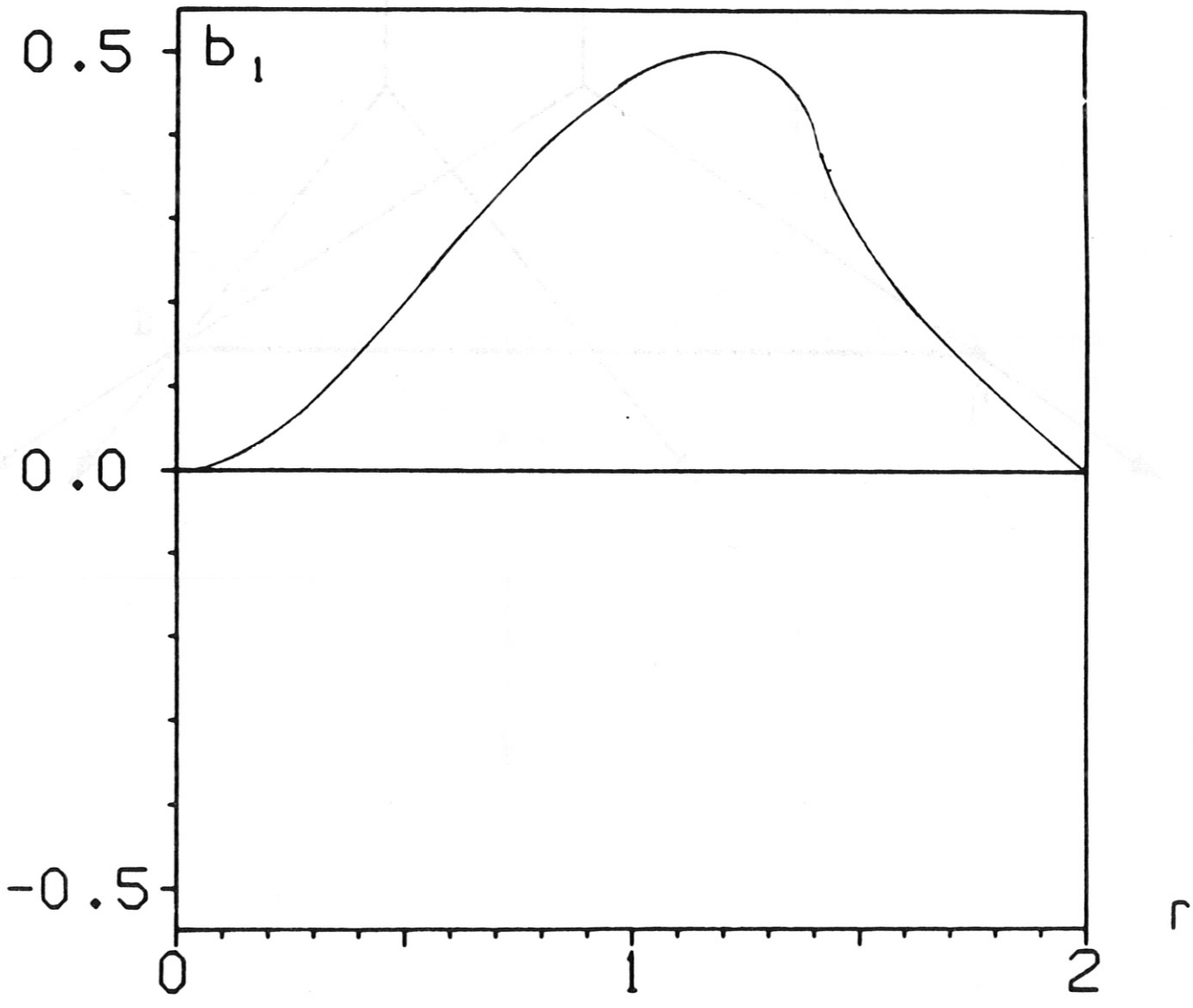

Fig 19b

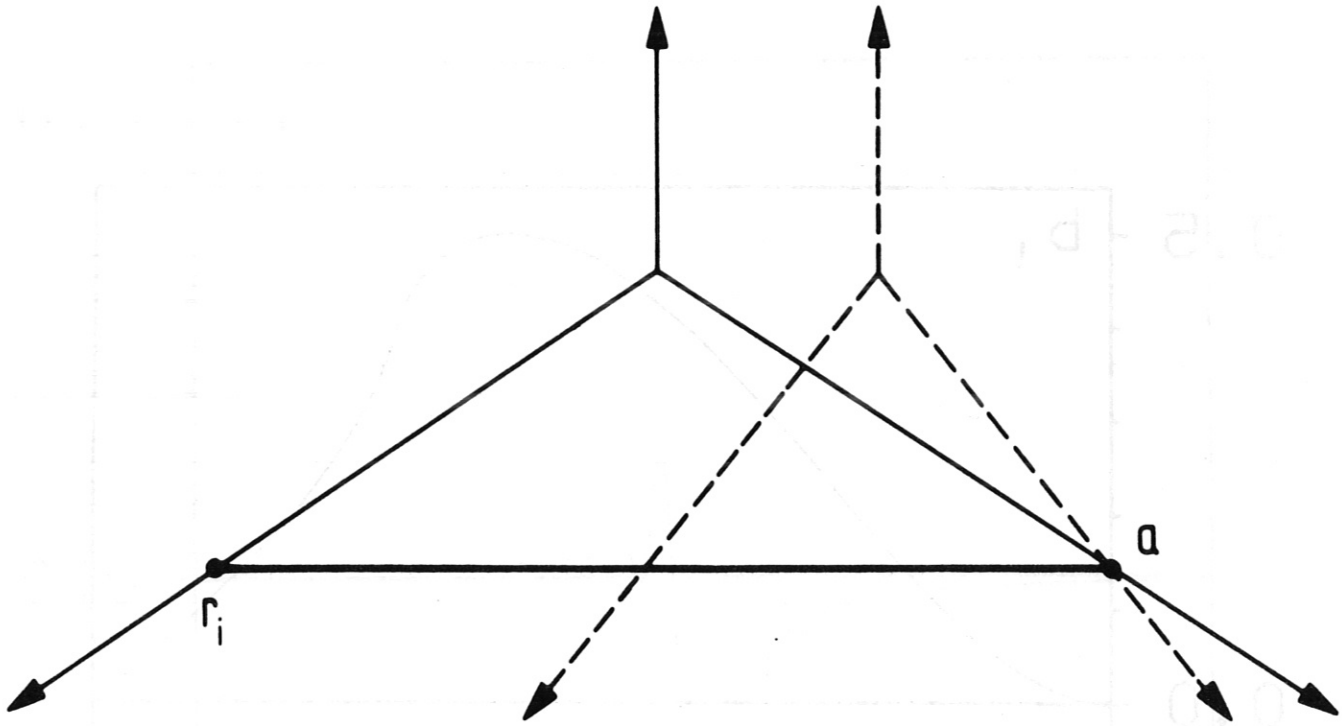

Fig 20

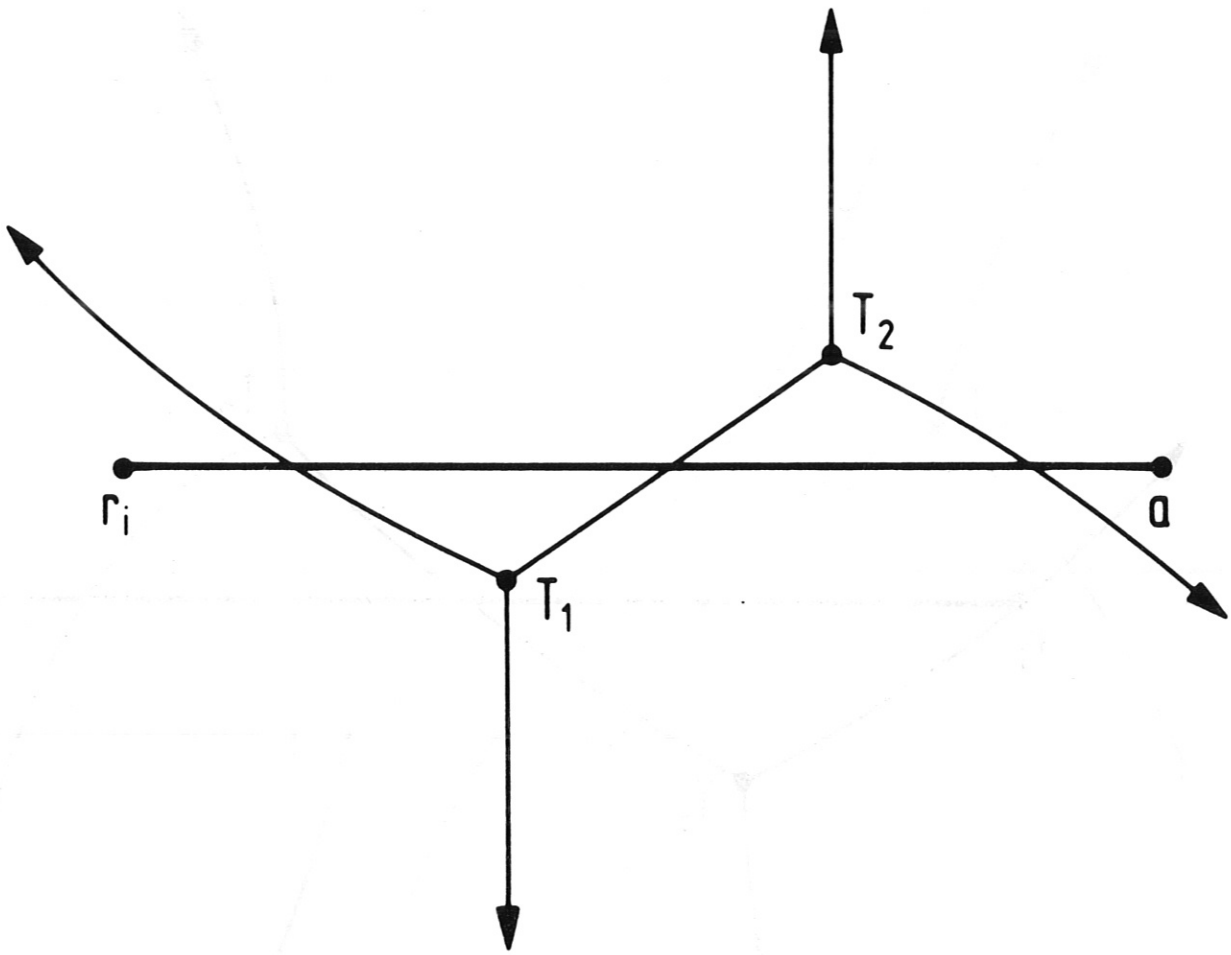

Fig 21a

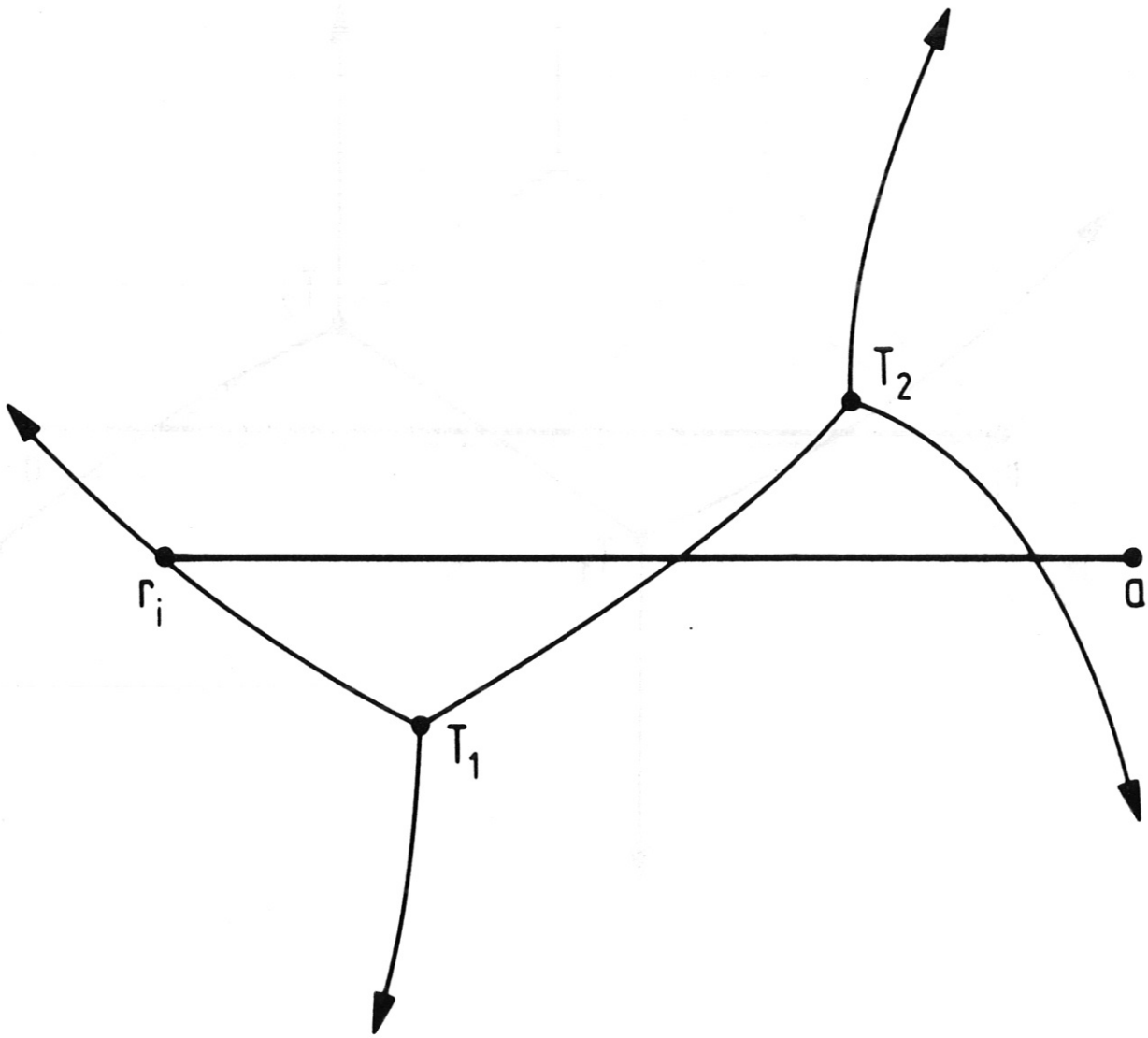

Fig 21b

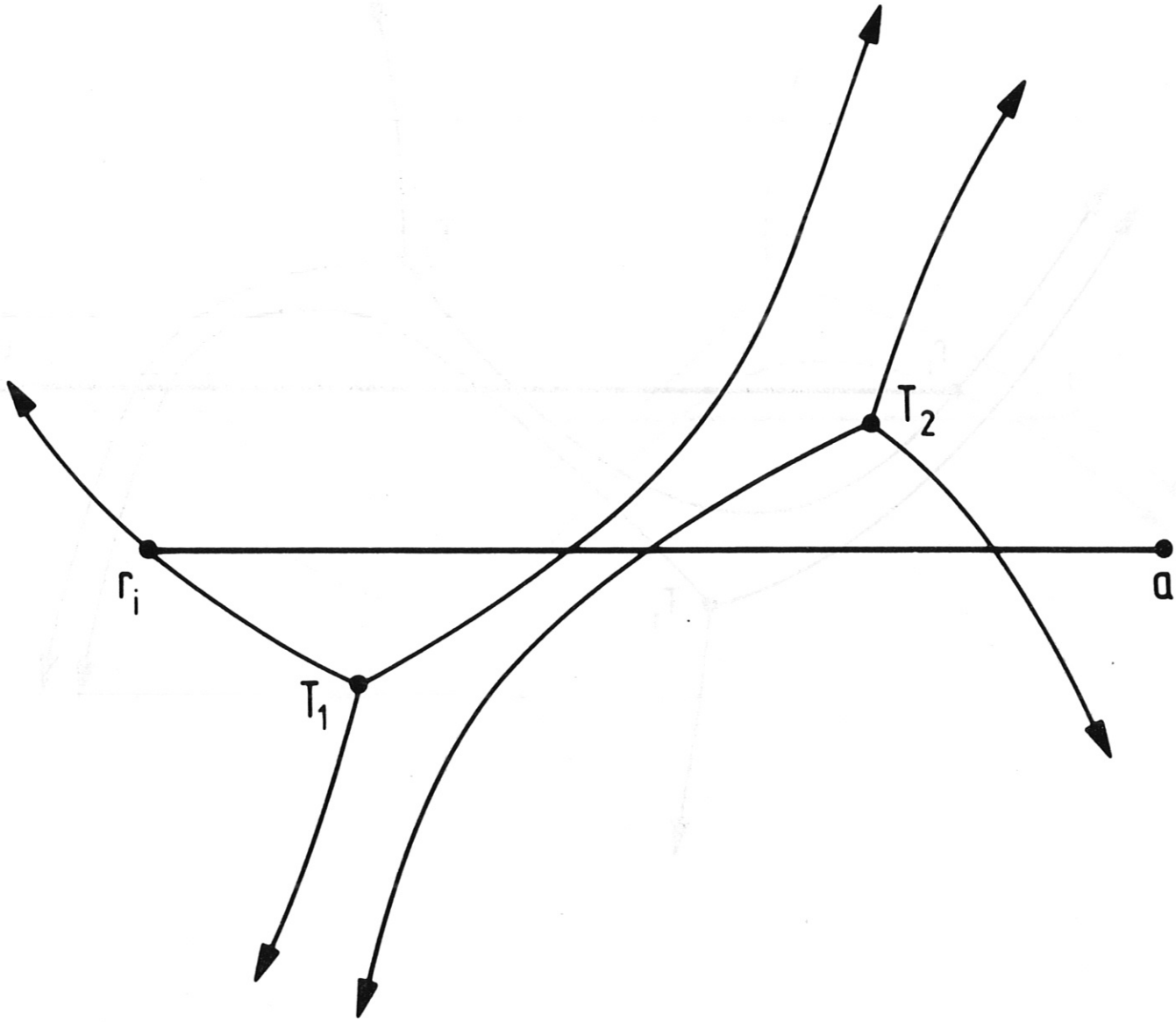

Fig 21c

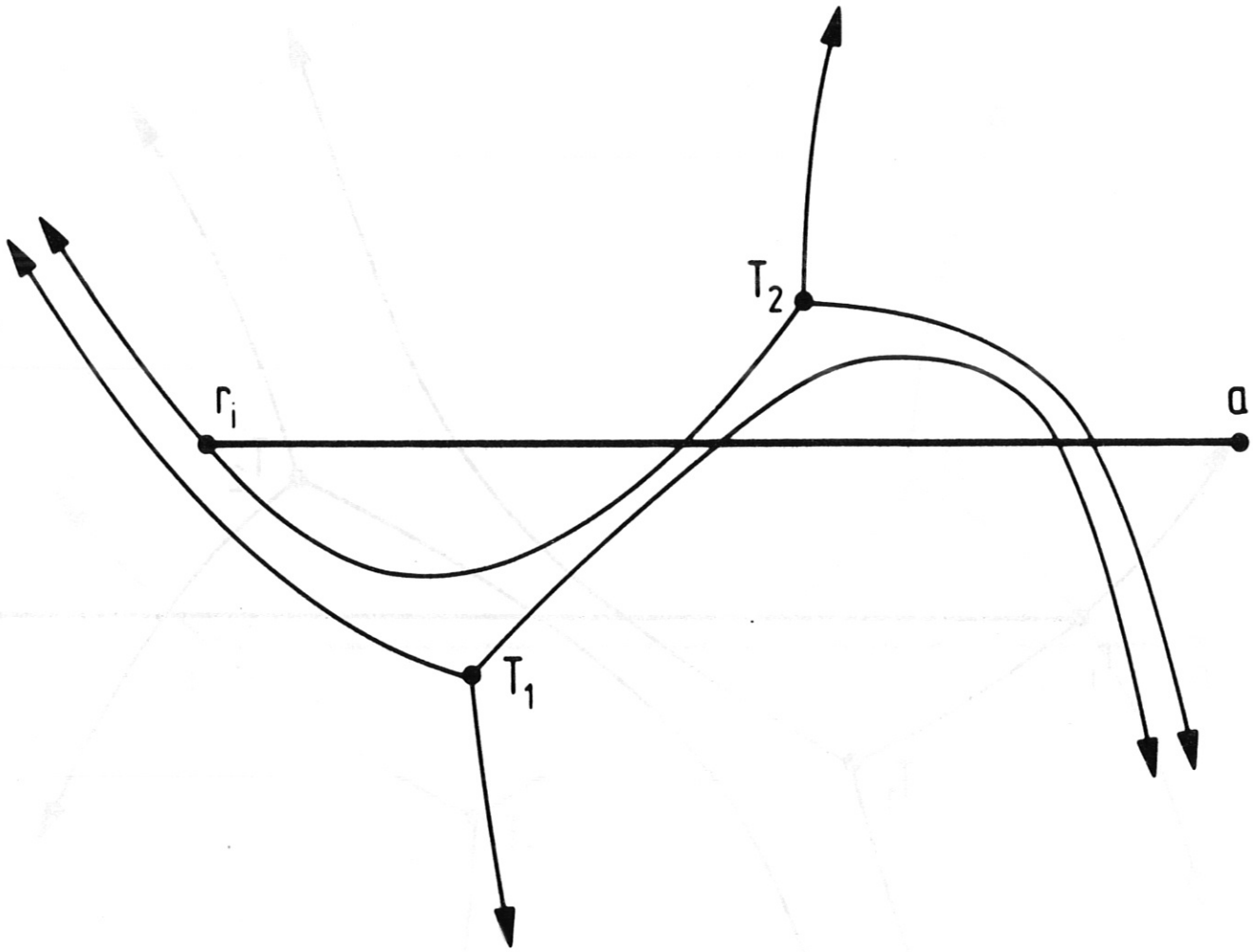

Fig 21d

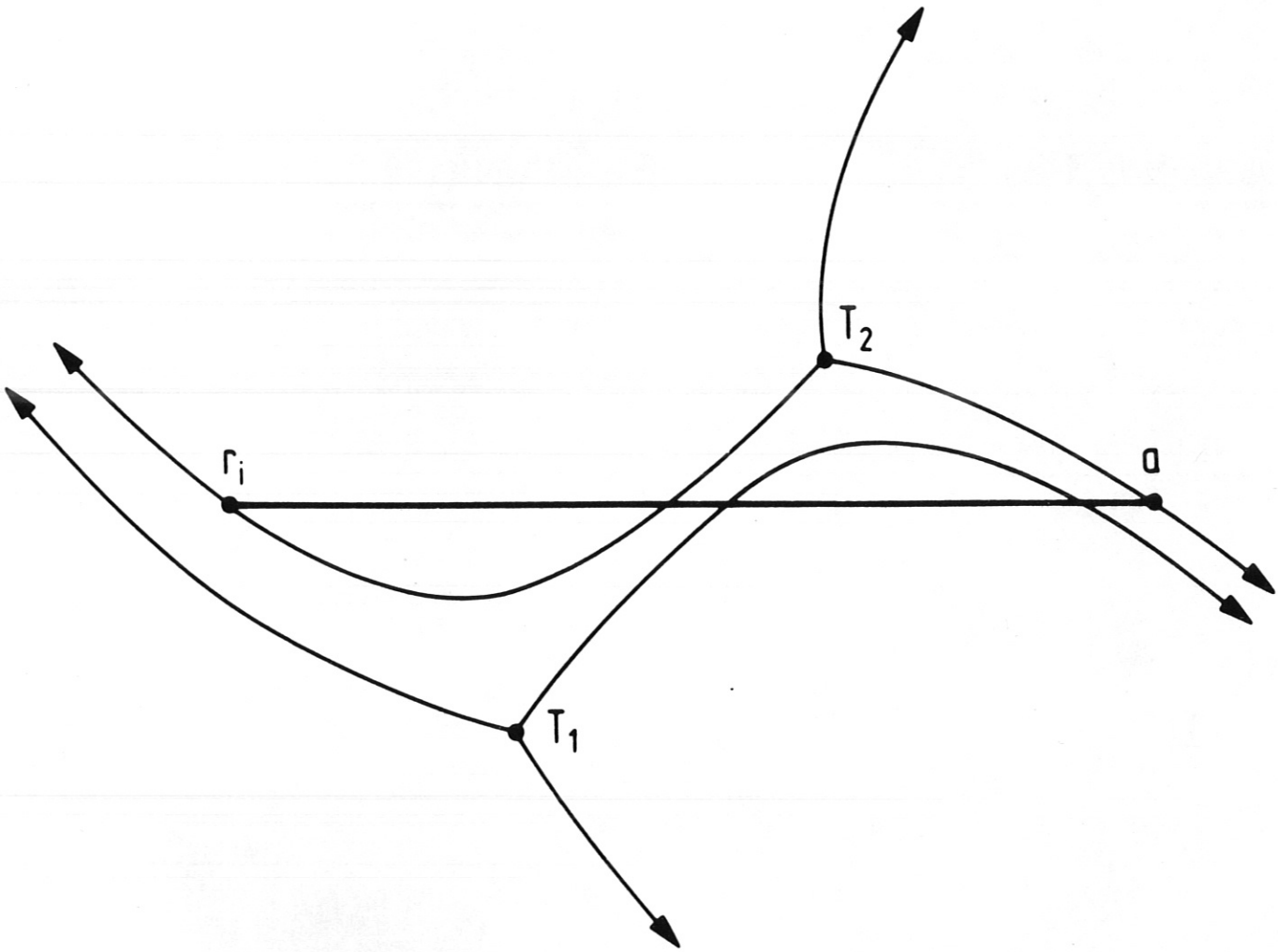

Fig 22